Spatially defined multicellular functional units in colorectal cancer revealed from single cell and spatial transcriptomics

Inbal Avraham-Davidi[1,20]*, Simon Mages[1,2,20], Johanna Klughammer[1,2,20], Noa Moriel[3], Shinya Imada[4], Matan Hofree[1,], Evan Murray[5], Jonathan Chen[5,6,7], Karin Pelka[5,6,8,9], Arnav Mehta[5,6,10], Genevieve M. Boland[5,11], Toni Delorey[1], Leah Caplan[1], Danielle Dionne[1], Robert Strasser[2], Jana Lalakova[12], Anezka Niesnerova[12], Hao Xu[12], Morgane Rouault[12], Itay Tirosh[13], Nir Hacohen[5,6], Fei Chen[5,14], Omer Yilmaz[4,15], Jatin Roper[4,16,*], Orit Rozenblatt-Rosen[1,17,*], Mor Nitzan[3,18,19*], Aviv Regev[1,4,17*]

[1]Klarman Cell Observatory, Broad Institute of MIT and Harvard, Cambridge, MA, USA

[2]Gene Center and Department of Biochemistry, Ludwig-Maximilians-Universität München, Munich, Germany

[3]School of Computer Science and Engineering, The Hebrew University of Jerusalem, Jerusalem, Israel

[4]Departmen of Biology at MIT, Koch Institute for Integrative Cancer Research at MIT, Cambridge, MA, USA

[5]Broad Institute of Massachusetts Institute of Technology and Harvard, Cambridge, MA, USA

[6]Massachusetts General Hospital (MGH) Cancer Center, Harvard Medical School (HMS), Boston, MA, USA

[7]Department of Pathology, MGH, Boston, MA, USA

[8]Current address: Gladstone-UCSF Institute of Genomic Immunology, Gladstone Institutes, CA, USA

[9]Current address: Department of Microbiology and Immunology, UCSF, CA, USA

[10]Dana Farber Cancer Institute, Boston, MA, USA

[11]Department of Surgery, MGH, Boston, MA, USA

[12]10xGenomics, Solnavägen 3H, Stockholm, Sweden

[13]Department of Molecular Cell Biology, Weizmann Institute of Science, Rehovot, Israel

[14]Harvard Stem Cell and Regenerative Biology, Cambridge MA, USA

[15]Department of Pathology, Massachusetts General Hospital, Boston, MA, USA

[16]Current address: Department of Pharmacology and Cancer Biology and Department of Medicine, Division of Gastroenterology, Duke University, Durham, NC, USA

[17]Current address: Genentech, 1 DNA Way, South San Francisco, CA, USA

[18]Racah Institute of Physics and Faculty of Medicine, The Hebrew University of Jerusalem, Jerusalem, Israel

[19]Faculty of Medicine, The Hebrew University of Jerusalem, Jerusalem, Israel

[20]These authors contributed equally

*Correspondence: inbalavr@gmail.com (I.A.-D.), jatin.roper@duke.edu (J.R.), orit.r.rosen@gmail.com (O.R.-R.), mor.nitzan@mail.huji.ac.il (M.N.), aviv.regev.sc@gmail.com (A.R.)

Abstract

While advances in single cell genomics have helped to chart the cellular components of tumor ecosystems, it has been more challenging to characterize their specific spatial organization and functional interactions. Here, we combine single cell RNA-seq, spatial transcriptomics by Slide-seq, and *in situ* multiplex RNA analysis, to create a detailed spatial map of healthy and dysplastic colon cellular ecosystems and their association with disease progression. We profiled inducible genetic CRC mouse models that recapitulate key features of human CRC, assigned cell types and epithelial expression programs to spatial tissue locations in tumors, and computationally used them to identify the regional features spanning different cells in the same spatial niche. We find that tumors were organized in cellular neighborhoods, each with a distinct composition of cell subtypes, expression programs, and local cellular interactions. Comparing to scRNA-seq and Slide-seq data from human CRC, we find that both cell composition and layout features were conserved between the species, with mouse neighborhoods correlating with malignancy and clinical outcome in human patient tumors, highlighting the relevance of our findings to human disease. Our work offers a comprehensive framework that is applicable across various tissues, tumors, and disease conditions, with tools for the extrapolation of findings from experimental mouse models to human diseases.

INTRODUCTION

The spatial organization of diverse cells in the tumor ecosystem impacts and drives interactions between malignant cells and neighboring immune and stromal cells, either promoting or suppressing tumor growth[1]. Recent studies have shown that systematic understanding of the spatial organization of tumors can shed light on disease progression and response to therapy, with specific features correlated with tumor subtypes[2–4], cancer prognosis[5–7], or response to treatment[8,9].

However, genome-scale, high-resolution dissection of the spatial organization of tumors and its functional implications remains challenging, largely due to technical limitations. Methods such as fluorescent *in situ* hybridization (FISH) and immunohistochemistry can only measure a handful of pre-selected transcripts or proteins, whereas single cell RNA-seq (scRNA-seq) does not directly capture spatial relations. Recent advances in spatial genomics and proteomics allow multiplexed or genome-scale measurements *in situ*[10–17], but with a trade-off between genomic scale and spatial resolution[18]. As a result, data from different experimental methods need to be integrated for a comprehensive view of the tissue biology. Many analytical tools have been developed to integrate some crucial aspects of the data[19–23], but it can be challenging to deploy them and distill answers to specific disease biology questions. This leaves open many fundamental questions about tissue organization and collective function, including whether there are canonical functional units in tumors, what may be their organization in the tumor landscape, and what role does each play in tumor progression.

A case in point is colorectal cancer (CRC), where initial lesions (adenomatous polyps) progress over time to carcinoma and eventually to metastatic disease. While the mutations that drive this process were extensively studied[24–27], and the cellular ecosystem of CRC has now been deeply charted[2,28,29], the spatial landscape is less well-characterized. In a recent study of human CRC[2], we statistically associated cell profiles across tumors and showed that they map to different cellular communities, reside in different locations in the tumor and reflect different tumor subtypes. However, absent genome wide *in situ* measurements, these statistical inferences do not yet reflect the full spatial organization of the tumor. Moreover, it is important to relate such patterns to those in animal models used in mechanistic studies and as pre-clinical models, to understand the relation between lab models and human tumors.

Here, we deciphered the spatial and cellular organization of colorectal cancer (CRC) by combining scRNA-seq, spatial transcriptomics by Slide-seq, and *in situ* RNA multiplex analysis, using a novel computational framework. We first profiled two inducible genetic mouse models of colorectal cancer that recapitulate key features of human CRC, before and after tumor initiation. We integrated the spatial and cell profiles to create a spatial cell map of the tumor landscape, revealing dysplasia-specific cellular layout and potential physical interactions. We found that the tumor landscape is organized in cell neighborhoods, each with distinct epithelial, immune, and stromal cell compositions, and governed by different gene programs. Three of the cell neighborhoods are associated with tumor progression, each activating different biological pathways but all active simultaneously albeit in different parts of the tumor. We devised a computational framework, based on the TACCO[21] method, extending it to compare single cell and spatial features of tumors between species and applied it to scRNA-seq data from human CRC. Multiple features were conserved between tumors in the mouse model and the human patients, and the mouse cellular neighborhoods correlated with malignancy and clinical outcome (progression-free intervals (PFI) and overall survival (OS)) in human patient tumors. Our work provides a general approach that can be applied to other tissues, tumors and disease conditions.

RESULTS

A cell atlas of genetic models of colorectal cancer

To chart the cell ecosystem of CRC and how it changes during tumor progression, we studied two genetic mouse models of CRC, one with inactivation of *Apc* and another in which *Apc* inactivation is accompanied by an oncogenic *Kras*$^{G12D/+}$ mutation and inactivation of *Trp53*[30–32] (**Figure 1A**). In the AV model, *Apc*$^{fl/fl}$*Villin*^{creERT2} mice are injected with 4-hydroxytamoxifen to the submucosal layer of the colon, inducing the deletion of *Apc* specifically in epithelial cells within the injection site[30]. In the AKPV model (*Apc*$^{fl/fl}$; *LSL-Kras*^{G12D}; *Trp53*$^{fl/fl}$;*Rosa*$^{26LSL\text{-}tdTomato/+}$; *Villin*^{CreERT2} mice, **Methods**), 4-hydroxytamoxifen injection also induces an oncogenic *Kras*$^{G12D/+}$ mutation and then inactivation of *Trp53*. In both cases, 4-hydroxytamoxifen injection leads to the formation of local lesions that resemble human dysplastic lesions[30].

We first generated a single-cell atlas of the models consisting of 48,115 high quality scRNA-seq profiles from normal colon, AV (3 weeks after 4-hydroxytamoxifen induction) and AKPV (3 and 9 weeks after induction) tissues. We captured a diverse cell census (**Figure 1B,C**, **Methods**), with 35 clusters annotated *post hoc* by the expression of known marker genes (**Figure 1B**, **Figure S1A,B**, **Methods**), across epithelial, immune and stromal cell compartments (**Figure S1C**). For validation purposes, we also generated multiplex *in situ* RNA profiles (with the Cartana[33] method) in 6 sections each from normal and AV conditions, using a panel of 66-180 marker genes chosen to best represent the cell types and programs found in the tissues (**Figure S1D, Methods**).

Tumorigenic genotypes cause shifts in the composition of epithelial cell populations and their microenvironment in AV and AKPV lesions

Dysplastic lesions exhibited shifts in proportions of immune and stromal cells, including changes in subsets pre-existing in normal tissue, as well as infiltration of new cell subsets (**Figure 1C,D** and **Figure S1D,E,F**). This resulted in both increase in cells of existing populations (*e.g.*, some T cell subsets (TNK05 (GdT/Il17+), TNK06 (Treg)) and emergence of new dysplasia-associated cells (*e.g.*, granulocytes (Gran01, Gran02) and monocytes (Mono02, Mono03)) mirroring observations in human CRC[2], breast cancer[34], and non-small cell lung cancer[35] (**Figure 1C,D** and **Figure S1D,E** and **Figure S2 A-C**). We validated these patterns using multiplex *in situ* RNA analysis (**Figure 1E**, **Figure S1F-H** and **Supplementary item 1 and 2**). Infiltration is likely to underlie many of these changes as many of the increasing cell subsets (granulocytes, monocytes, mast cells) expressed genes, such as Sell and Ccr2, indicating tissue recruitment, and as the cells dramatically increase in proportion despite negligible signals of proliferation programs.

Two of four monocyte subsets, Mono02 and Mono03, were unique dysplasia-associated cells (**Figure S2D-F**) and were respectively enriched for general inflammatory response genes (FDR=5.7 10^{-30}, two-sided Fisher's exact test in GO term enrichment) and interferon beta and gamma response genes (FDR=3.5 10^{-11}, 1.0 10^{-13}). T cell subsets showed the expected diversity across nine subsets (**Figure S2G-I**)[36], with a significant decrease (out of all T cells) in TNK01 (GdT/Cd8) in the dysplastic microenvironment and an increase in TNK05 (GdT/Il17+) (**Figure**

S2J). This is consistent with the T cell composition in tumors from mismatch repair proficient (MMRp) CRC patients (**Figure S2K**). RNA velocity analysis[37] of T cells from normal and AV tissue (**Figure S3A**) showed a change in inferred cellular relationships with TNK03 (naïve T) and TNK02 (Th1/Th17) preceding TNK06 (Treg), consistent with the promotion of an immunosuppressive microenvironment, and TNK08 (proliferating T) also preceding TNK02 (Th1/Th17), TNK04 (GdT/Cd8) and TNK05 (GdT/Il17+) populations.

Within the five subsets of stromal cells (including vascular endothelial and lymphatic endothelial cells and three fibroblast subsets, **Figure S2L-N** and **Methods**), Endo01 (vascular) were enriched in dysplastic lesions compared to normal colon (FDR=1.8 10^{-3}, two-sided Welch's t test on CLR transformed compositions; **Figure S2O**). Angiogenesis-related pathways, such as angiogenesis (FDR=1.0 10^{-11}) and positive regulation of angiogenesis (FDR=3.4 10^{-4}) as well glycolytic process (FDR=1.4 10^{-4}) were enriched in Endo01 (vascular) from lesions compared to normal colon (**Table S1**). This is in line with vascular adaptation to the tumor's growing needs for nutrients and oxygen[38] and with the increased expression of the vascular growth factor *Vegf-A* in both monocytes and macrophages (**Figure S2P**).

Cell-intrinsic expression shifts in different sub-lineages in the dysplastic epithelium

Epithelial cells showed dramatic cell-intrinsic changes between normal tissues and either AV or AKPV lesions, such that the cell profiles of dysplastic epithelial cells in both models were highly distinct from normal epithelial cells (and similar to each other) (**Figure 1C**, **Figure S4A** and **Methods**). Epithelial cell profiles from normal mice (41% of cells) separated from most of those from AV and AKPV models (59% of cells) (**Figure 2A** and **Figure S4A,B**), suggesting a common shift in all dysplastic cells from the normal state. Notably, 11% of epithelial cells from AV/AKPV mice were classified as non-dysplastic healthy cells, indicating that normal, non-dysplastic, cells may be present in or adjacent to the lesion microenvironment (**Figure 2B** and **Figure S4A**), although we cannot firmly rule out adjacent tissue contamination. We annotated two cell clusters – Epi01 (dysplastic stem-like) and Epi05 (dysplastic secretory-like) – as dysplastic, due to their virtually exclusive presence in AV and AKPV models and because they expressed high levels of *Apc* target genes (*e.g.*, *Axin2, Ascl2, Myc, Ccnd1, Lgr5*) and were enriched in tdTomato^{+} cells from AKPVT mice (**Figure 2C** and **Figure S4C,D**) while also spanning the enterocyte to secretory continuum with healthy cells (**Figure S4B**, PC2).

Interestingly, Epi05 (dysplastic secretory-like) had distinguishing markers (*e.g.*, *Ccl9, Mmp7, Ifitm3*) from their counterparts in normal tissue, Epi04 (secretory) (**Figure 2A-C** and **Figure S4A,C,E**). *Mmp7* and *Ifitm3* are known to promote metastasis in human CRC[39,40], and *Ccl9* expression by epithelial cells promotes tumor invasion through recruitment of Ccr1^{+} myeloid cells to the tumor's invasive front in a mouse model of CRC[41]. Notably, *Ccr1* is expressed by newly recruited monocytes, macrophages and granulocytes in our model, suggesting a potential mechanism for tumor infiltration and invasion (**Figure S4E**). Thus, dysplastic secretory epithelial cells may perform additional functions that differ from those of their healthy counterparts.

RNA velocity[37] analysis of the epithelial cell compartment predicted that in the dysplastic epithelium (**Figure S3B, right**) a proliferating stem-cell like dysplastic subset is a direct source to both a massively expanded and heterogeneous non-proliferating population of dysplastic stem-like cells (expressing WNT signaling and angiogenesis programs) and to dysplastic cells of different 'differentiation states' (MHCII expressing stem/progenitors leading to enterocytes and secretory-like cells) (**Figure S3B,C**). Conversely, in the normal epithelium (**Figure S3B**, left), the 'root' is placed in a much smaller population of proliferating intestinal stem cells, and the stem cell compartment is overall much more modest. The proliferation and differentiation path of previously identified normal epithelial cells remains intact (*i.e.*, reminiscent of the one in normal samples) even in the dysplastic lesions (**Figure S3B**). While our RNA velocity analysis provides insights into potential cellular trajectories, further experimental validation is required to confirm these findings.

Expression programs for stem-like functions, Wnt signaling, angiogenesis and inflammation are activated in dysplastic epithelial cells

Both normal and dysplastic epithelial cells varied along a continuum, as expected and previously observed in the ongoing differentiation in the colon epithelium[2,42–44] and our RNA Velocity analysis (**Figure S3**). Using non-negative matrix factorization (iNMF from LIGER[45], **Methods**), we recovered 20 expression programs spanning the different epithelial functions, and annotated them by Gene Ontology terms enriched in their top 100 weighted genes (**Figure 2D,E**, **Figure S3C, S4F-L, Methods**).

The programs enriched in different dysplastic cells highlighted key processes that play a role in tumor promotion, including stem cell programs, Wnt signaling, angiogenesis, and inflammation and innate immunity, including interferon alpha, beta and gamma pathways (**Figure 2D,E, Figure S3C**). In particular, the stem cell program (#16) detected in some cells across all conditions, was enriched in dysplastic samples (FDR=5.6 10^{-10}, two-sided Welch's t-test on CLR transformed compositions), reminiscent of a recently described population in human[28,29]. Comparing cells from dysplastic and normal samples that express the stem cell program, the dysplastic cells had distinct expression profiles with induction of negative regulators of Wnt signaling (FDR=4.5 10^{-5}, two-sided Fisher's exact test in GO term enrichment, *e.g.*, *Notum*, Wnt inhibitory factor 1 (*Wif1*) and *Nkd1*) and genes that are related to cellular response to interferon-gamma (FDR=1.7 10^{-6}, *e.g.*, *Ccl9, Ccl6*) and immune system process (FDR=6.4 10^{-4}, *e.g.*, Ifitm1 and Ifitm3) (**Figure 2E,F**). This is consistent with recent studies showing that *Apc*-mutant stem cells secrete negative regulators of Wnt signaling to induce the differentiation of the WT stem cells in their proximity, thereby outcompeting them and promoting tumor formation[46,47]. Thus, stem cells from dysplastic lesions may have non-canonical function and regulation. In addition, the programs for Wnt signaling (expressing both positive and negative regulators; #4, FDR=2.8 10^{-6}), angiogenesis (#14, FDR=1.2 10^{-9}), inflammatory response (#6, FDR=1.4 10^{-6}), and innate immune response and interferon response (#7, FDR=1.2 10^{-2}) were all predominantly expressed or enriched in AV/AKPV epithelium (all with two-sided Welch's t-test on CLR transformed compositions, **Figure 2E** and **Figure S4I-M**). These results are consistent with the known role of the Wnt signaling pathway in CRC, and of angiogenesis, response to hypoxia and inflammation in tumor progression[48–50].

Malignant-like tissue programs and composition are conserved between mouse and human tumors

To evaluate the relevance of our findings to human colorectal cancer, we compared them to a scRNA-seq atlas we recently generated from tumor and adjacent normal tissue from 62 patients with either MMRp or MMRd CRC[2]. We compared mouse and human tumors in terms of their epithelial expression programs, cellular composition, and cell associations in multicellular hubs[2].

While our mouse model should more closely resemble MMRp tumors, we compared to both classes separately and together to identify any shared features.

To assess the similarity between mouse and human programs we controlled for overall cross-species and batch differences by normalizing program-specific expression profiles with species-specific background profiles (**Methods**). The Pearson correlation coefficients of these normalized scores between the human and mouse programs indicate some overlap in the programs defined on mouse and human data (**Figure S5A**). Epithelial cells from human and mouse tumors expressed many programs highly correlated between the species (**Figure S5B**, **Methods**), including for cell cycle, inflammation, epithelial secretory, angiogenesis, Wnt signaling, and normal colon functions.

Co-variation in cell proportions across samples (by scRNA-seq) was also conserved between human and mouse tumors, suggesting broad conservation of tumor composition. For example, in both species the proportion of endothelial cells and fibroblasts correlated across samples, as did T and B cell proportions in human tumors and mouse dysplastic lesions (**Figure S5C**). Moreover, when we transferred epithelial program annotations from mouse to human scRNA-seq and calculated their co-variation across samples in each species, programs 11 (proliferation), 14 (angiogenesis) and 16 (stem cells), co-varied both across dysplastic mouse tumors and across human MMRp and MMRd tumors (**Figure S5D** and **Methods**), suggesting a conserved dysplastic tissue architecture.

Integrated spatial and single-cell atlas of mouse CRC tumors

To comprehensively decipher the distribution of cells and programs in the tumor spatial niche, we next used Slide-seqV2[15] for genome-wide spatial RNA-seq at 10 µm resolution. We sectioned and profiled frozen tissues from four normal colon and four AV lesions using 10 Slide-seqV2 pucks (**Methods**), recovering 221,936 high quality beads (**Figure S6A-C**, **Methods**). We then integrated the single cell census and spatial profiles using TACCO, which allowed us to annotate each bead with compositions of discrete cell types (from epithelial, immune and stromal compartments) and to further annotate the epithelial fraction of each bead with a composition of epithelial program activity (**Figure 1A** "annotation").

We first used TACCO to annotate every bead in the Slide-seq data with a composition of discrete cell subtypes for every puck separately, using its matching single-cell reference (normal or disease; **Figure 1A**, **Methods**). To this end, TACCO iteratively solved optimal transport problems to assign cell subtypes to fractions of reads of the beads. TACCO relies on unbalanced optimal transport to allow for shifts in the frequency of cell subtypes in the pucks *vs*. the single-cell dataset, while using the reference cellular frequencies as prior knowledge (**Figure S6E,G**). TACCO's cell type mapping recapitulated the muscularis layer in its expected tissue location based on the inferred cellular composition pattern (**Figure 3A, 4A and S6D**). This illustrates that TACCO's compositional annotations align well with biological patterns.

Next, we used TACCO to map the epithelial gene programs (defined above), focusing on transcript counts that are inferred as derived from epithelial cells. TACCO partitioned the read count matrices for each puck, assigning counts to epithelial cells based on the mapped per-bead cell subtype annotations (from the first step) and the expression profiles associated with each subtype

(**Methods**). It then summed all epithelial contributions into an epithelial-only spatial count matrix, followed by optimal transport to assign epithelial program contributions to individual beads, based on epithelial cell-only read signals. As for cell type mapping, the proportional contribution of the programs largely recapitulated their contributions in scRNA-seq (**Figure S6F,H**).

Altered and less ordered local cellular organization of dysplastic lesions

We assessed the local cellular architecture in terms of the preferential proximity of cells of certain type or expressing particular epithelial programs, within a fixed-sized neighborhood, by adapting an earlier method. We defined a z-score as significance of the observed neighborship relations compared to the null for neighborhoods of 20, 40 or 60 μm diameter (**Figure 3B,C** and **Figure S7A,B**). This z-score is defined with respect to a population of random cell type annotations generated by random permutations of the cell type annotations between the beads, where in our case we permute fractional cell type contributions.

Cell proximity preferences in the normal colon tissue are consistent with the expected morphology, validating our approach (**Figure 3A,B**). Epithelial cells were organized such that the differentiated Epi02 (Enterocytes) are excluded from the stem cell niche (**Figure 3B** and **Figure S7C**), and endothelial cells and fibroblasts were also spatially co-located in a focused region (**Figure 3B**), with T cells in their vicinity (**Figure 3B**). Our multiplex *in situ* RNA analysis validated the exclusion of enterocytes from the stem cell niche, as also seen in Slide-seq data (**Figure S7C,D**).

While some normal tissue features are preserved in dysplastic samples, including co-location of cells of the same lineage[5,10] (**Figure 3A-C**), there were notable changes, and more disorder. Cell types were more randomly distributed in AV lesion *vs*. normal tissue, reflected in lower z-scores

($p=1.6\ 10^{-37}$, one-sided Mann-Whitney U test; **Figure S7E**). At short distances, all epithelial cells (normal and dysplastic) were preferentially located close to cells from the same subtype (**Figure 3C**) and even to cells with similar functions: epithelial cells expressing programs associated with malignant-like function (*e.g.*, program 4 (Wnt signaling), 14 (angiogenesis) and 16 (stem cells)) resided close to each other and were spatially distant from cells expressing programs that are related to normal epithelial functions (*e.g.*, program 5 (basolateral plasma membrane), 8 (apical plasma membrane) and 10 (oxidation-reduction process)), supporting a model where tumor progression is structured and compartmentalized (**Figure S7F**). Immune and stromal cells were generally excluded from epithelial cell neighborhoods. Granulocytes aggregated together (self-proximal) (**Figure 3C**) and were relatively close to endothelial cells and dysplasia-associated monocytes (Mono02, Mono03), consistent with their recruitment from the blood through the vessels (**Figure 3C** and **Figure S7G**). Our multiplex *in situ* RNA analysis validated the spatial enrichment of monocytes and granulocytes near vessels (**Figure S7H**).

Epithelial regional analysis recovers canonical structures in normal colon

To detect distinctive tissue regions in tumors, which lack traditional tissue references, we identified cellular neighborhoods with both similar epithelial program activity and a particular composition of immune and stromal cells. Specifically, we first identified “epithelial program regions” as areas of distinct epithelial program activity, and then found immune or stromal cells associated with each region (**Figure 1A** “annotation”). Intuitively, we defined “regions” based on both the similarity in epithelial expression program activity and proximity in space. To do this, after assigning epithelial programs to epithelial beads, we clustered the beads based on a weighted sum of spatial proximity and expression program similarity. This results in spatially contiguous annotation of beads with distinct epithelial program activity, which, together with the immune and stromal cells in their proximity, compose the “region”. Specifically, using TACCO, we defined epithelial program regions by Leiden clustering of the weighted sum of neighborship graphs for spatial bead proximity and epithelial expression program similarity, such that transcriptionally similar epithelial beads on different pucks can be connected (despite “infinite” spatial distance, **Methods**). We then used this single framework for region annotation across all pucks (**Figure 4A**), to determine the distinctive composition of additional cell types in the same set of spatial regions (**Figure 4B-D** and **Figure S8A**).

In the normal colon, the regional analysis (**Figure 4A**, bottom) robustly recovered the expected spatial organization of the healthy colon across five regions and their cellular composition and sublayers (**Figure 1A**), from luminal/apical to basal. Four regions recovered by TACCO corresponded to different layers of the mucosa (**Figure 4A** and **4E,F**): a luminal layer with reads found beyond the cellular layer and likely representing cellular debris trapped in the mucus; three apical layers expressing programs related to normal epithelial function (transmembrane transport, oxidation-reduction process) with gradual transition from apical to basal features; and a basal-most layer, enriched for the deep crypt, proliferation (G1/S,G2/M), MHCII and basolateral plasma membrane programs, all common features of the deep crypt area. Finally, region 2, enriched with fibroblasts, myofibroblasts and endothelial cells, and located in the most basal side of the tissue, captured the submucosal and muscularis propria layers, which are predominantly comprised of fibroblasts and muscle, respectively, alongside blood and lymphatic vessels, nerves and immune cells. Overall, TACCO recovered the known organization of the colon, showing the power of our unsupervised mapping approach and shedding light on expression programs that are required for the maintenance of normal colon homeostasis.

Dysplastic lesions maintain some of the programs of the corresponding regions in healthy tissue

AV lesions did not maintain the robust organization of normal tissues, and reflected the expected histopathology of high grade dysplasia, when dysplastic cells are confined to the mucosal layer and do not invade the submucosa[51] (**Figure 1A** and **4A**, top). Specifically, the submucosal and muscularis propria layers from both normal and AV lesions were assigned to region 2 (**Figure 4A**).

Despite the altered morphology, some of the disrupted regions also expressed programs characteristic of their normal healthy function, suggesting that tumor progression is spatially structured and compartmentalized. For example, the region above the submucosa, captured as region 1 in AV lesions and region 5 in normal colon (**Figure 4A**), had similar features in both AV lesions and normal samples. Thus, although the overall spatial organization was disrupted in the lesion, region 1 in AV lesions expressed programs that are reminiscent of the normal deep crypt region 5, and was enriched for deep crypt cells and programs that are related to proliferation and MHC II[43] (**Figure 4A,C**). These included proliferation programs 3 and 11 and both normal stem cells (Epi03) and dysplastic secretory-like cells (Epi05), as well as dysplastic stem cells (Epi01, though to a lesser extent than some other regions), so it may reflect one of the proliferative stem cell (and dysplastic secretory-like) niches in AV models (**Figure 4B,C**). Other regions in the AV lesions also contained some epithelial cells with normal profiles, expressing programs that should allow them to maintain their capacity to perform normal tasks. For example, region 3 expressed apical plasma membrane functions and region 10 was enriched with oxidation-reduction functions (**Figure 4C**).

To learn about the spatial distribution of the dysplastic regions, we measured their distance from region 2 (muscularis), which is a stable landmark in the lesions. Remnants of the layered structure of the healthy tissue were still observed in the AV tissue, especially at relatively low distances from the muscularis. For example, healthy region 5 – characteristically located at distances of about 150-200µm from the muscularis – is replaced by dysplastic region 1, peaking at 200µm. All malignant-like regions (6/8/11) were spatially associated at ~300-700µm from the muscularis (**Figure S8C**), located ~100-400µm apart from each other (**Figure S8D**). We further validated this result at the protein level, by staining for b-catenin, showing an (inactive) cytoplasmic localization in the region adjacent to the muscularis, and mostly nuclear (active) localization in distal regions, near the lumen (**Figure S8B**).

Three spatially and functionally distinct tumor regions enriched in AV lesions

Three regions – 6, 8, and 11 – had epithelial composition and programs that suggested advanced malignant-like characteristics, each highlighting a potentially different mechanism for tumor progression (**Figure 4G,H**). These three 'malignant-like regions', were enriched (*vs*. all other regions) in stem cell, Wnt signaling and angiogenesis programs (16, #4 and #14; FDR=9.6 10^{-21}, 8.1 10^{-10}, 3.7 10^{-10}, two-sided Welch's t-test on CLR transformed compositions) and depleted of normal epithelial programs (#5, #8, and #10; FDR=5.5 10^{-12}, 1.6 10^{-12}, 4.2 10^{-10}, **Figure 4I**). Furthermore, the malignant-like regions were enriched in immune cells, including monocytes-macrophages (FDR<=1.5 10^{-5}; excluding Mac02 (Lyve1+)), T cell subsets TNK02 (Th1/Th17), TNK05 (GdT/Il17+), TNK06 (Treg), TNK08 (proliferating T) (FDR=2.4 10^{-3}, 2.2 10^{-4}, 1.7 10^{-3},

$9.6\ 10^{-4}$; two-sided Welch's t-test on CLR transformed compositions), infiltrating granulocytes (FDR<=$9.7\ 10^{-3}$), and mast cells (FDR=$1.4\ 10^{-2}$), suggesting an ongoing immune response (**Figure 4J**). However, each one of the three regions had a different epithelial program composition, suggesting that in each type of region there is a different dominant pathway/feature that may drive tumor progression (**Figure 4C, Table S2**).

Region 6 was characterized by an inflammatory and angiogenic multicellular community, with epithelial and immune cells expressing inflammatory programs, endothelial cells and monocytes connected in a pro-angiogenic circuit, and pro-invasive genes expressed by both endothelial and immune cells (**Figure 4B,C**). Specifically, region 6 was distinctly enriched for proliferation (programs 3 and 11; FDR=$2.2\ 10^{-14}$, $1.2\ 10^{-15}$, two-sided Welch's t-test on CLR transformed compositions) and inflammatory epithelial programs (programs 6 and 7; FDR=$9.0\ 10^{-7}$, $2.0\ 10^{-11}$), and its non-epithelial compartment was correspondingly enriched for genes from inflammatory pathways, including the response to TNF, IL-1 and IFN γ (FDR=$3.1\ 10^{-4}$, $2.8\ 10^{-3}$, $4.9\ 10^{-6}$, two-sided Fisher's exact test in GO term enrichment), and chemotaxis of monocytes, neutrophils, and lymphocytes (FDR=$1.5\ 10^{-3}$, $3.2\ 10^{-10}$, $1.0\ 10^{-2}$, **Table S2**), suggesting recruitment of inflammatory cells from the circulation or other parts of the tissue. Region 6 was also enriched for collagen binding genes and collagen-containing extracellular matrix (ECM) genes (FDR=$1.4\ 10^{-2}$, $7.6\ 10^{-5}$, two-sided Fisher's exact test in GO term enrichment, **Table S2**), which are important for migration and invasiveness[52]. These include *Sparc*, expressed mainly by endothelial cells and fibroblasts in our data, known to promote colorectal cancer invasion[53]; and *Ctss*, a peptidase expressed by T cells and monocytes-macrophages that promotes CRC neovascularization and tumor growth[54]. Finally, gene expression patterns in endothelial cells and monocytes in region 6 suggested active angiogenesis through a multi-cellular feedback loop, with enriched numbers of vascular and lymphatic endothelial cells expressing immune-attracting chemokines (*Cxcl9*) and adhesion molecules (*e.g. Chd5, Mcam*), monocytes expressing proangiogenic factors that induce proliferation of endothelial cells (*e.g.*, *Mmp12*), and monocytes and macrophages expressing *Ctsd*, which increases tumorigenesis in CRC models[55] (**Figure S8E**).

Region 8 was enriched for deep crypt cells (program 13; FDR=1.7 10^{-14}, two-sided Welch's t-test on CLR transformed compositions), reminiscent of the normal stem cell niche in normal colon, an epithelial innate immune program (program 1; FDR=3.4 10^{-100}) expressed by secretory cells in AV and AKPV lesions, and plasma and B cell activity. Unlike the canonical (normal) deep crypt region (region 5), which is enriched for MHCII expression (program 18; FDR=8.6 10^{-28}), this region was depleted for the program's expression (FDR=2.1 10^{-26}), which may indicate an earlier stem cell-like state[43], or a decoupling of the cell cycle and MHCII programs (which are coupled in normal ISC differentiation, and allow a cross talk with T cells to modulate T cell differentiation) (**Figure 4B,C**). The region's non-epithelial compartment was enriched for B cell activation and BCR signaling genes (FDR=4.0 10^{-4}, 1.9 10^{-3}, two-sided Fisher's exact test in GO term enrichment, **Table S2**). This may be related to B cell function in protection from lumen antigens[56] or to tertiary lymphoid structures (TLS), which is correlated with clinical benefits in cancer patients[57]. Notably, Epi05 (dysplastic secretory-like) enriched in Region 8 (**Figure 4B**) expressed higher levels of inflammatory genes and immune chemokines (*e.g.*, *Ccl9, Ifitm3*) compared to normal counterparts, Epi04 (secretory) (**Figure 2C** and **Figure S4C,E**), and may thus promote the formation of this region. We validated the presence of TLS-like structures in association with deep crypt secretory cells in AV lesions using multiplex RNA analysis (Cartana) (**Supplementary item 3**), showing that the dominant population of B cells is accompanied by monocyte-macrophages and T cells characteristic of TLSs, as well as the expression of *Reg4* and *Muc2*, deep crypt goblet/secretory cell markers.

Region 11 was populated by cells expressing the Wnt signaling pathway program (4, FDR=9.3 10^{-13}, two-sided Welch's t-test on CLR transformed compositions), with several lines of evidence supporting an active epithelial to mesenchymal transition (EMT) in this region. Epithelial cells in region 11 were enriched for the expression of mesenchymal genes, including Vimentin[58] (*Vim*, FDR=7.4 10^{-245}, one-sided Fisher's exact test), *Prox1*[59] (FDR=3.7 10^{-153}), and *Sox11*[60] (FDR=7.7 10^{-224}) (**Figure S8F**), as well as for EMT signatures from a mouse model of lung adenocarcinoma [61] (FDR=1.5 10^{-142}, two-sided Mann-Whitney U test) and from human head and neck squamous cell carcinoma tumors[62] (FDR=6.9 10^{-55}, two-sided Mann-Whitney U test). This is consistent with the role of Wnt signaling in promoting EMT and a mesenchymal phenotype in CRC, breast cancer and other epithelial tumors[63,64]. Region 11 non-epithelial cells also expressed genes encoding MHC-I binding proteins (FDR=4.6 10^{-2}, two-sided Fisher's exact test in GO term enrichment, **Table S2**) and actin cytoskeleton, filament and binding proteins (FDR=3.1 10^{-6}, 7.7 10^{-3}, 2.7 10^{-10}). Organization of the cytoskeleton affects migration, adherence, and interaction of lymphocytes with antigen presenting cells[65]. Notably, region 11 also concentrated at a more distal part of the tissue at ~900µm from the muscularis suggesting an outgrowth of the tissue towards the lumen (**Figure S8C**).

Non-epithelial cells formed two cellular hubs in the malignant-like regions (6,8,11) (**Figure S8G**): An endothelial-fibroblast hub, detected in all three regions, and an immune hub with B cells, TNK cells, monocytes, and macrophages, which was prominent in inflammatory region 6, weaker (less spatially correlated) in region 8 (but validated *in situ*), and not correlated in region 11. Thus, activation of an immune response is reflected by close proximity between immune cells. We further characterized the organization of the vascular niche using our multiplex *in situ* RNA data, finding that while neighbors of the Pdgfrb-expressing pericytes are mainly other Pdgfrb-expressing pericytes and endothelial cells, Pecam1-expressing endothelial cells appear self-enriched next to themselves at cellular scale distances and close to Pdgfrb-expressing pericytes for larger distances (**Figure S8H**).

Overall, three multicellular community regions were enriched in AV lesions: (**1**) inflammatory epithelial regions with endothelial cells and monocytes expressing angiogenesis, inflammation and invasion programs; (**2**) epithelial stem-like regions, associated with plasma and B cell activity; and (**3**) regions with epithelial to mesenchymal transition (EMT) and Wnt signaling dysplastic cells. Each region highlights different processes that modulate tumorigenesis or invasion, and the three regions co-exist in the same tumor at different spatial locations.

Cell-cell interactions are rewired in AV lesions

To identify cell-cell signaling mechanisms that may underly these regional associations, we used COMMOT[66], a computational framework that uses Optimal Transport to infer cell-cell communication from receptor-ligand expression patterns in spatially resolved data. We used COMMOT's bead-wise communication 'output' and devised a method to address p-value inflation in statistical enrichment testing, using spatially-informed data aggregation (**Methods**).

We observed stronger and distinct ligand-receptor interactions in AV *vs*. normal samples, reflecting the activated state in the dysplastic tissue (**Figure 4K, Supplementary item 4A**). In particular, while interactions enriched in AV lesions involved immune, epithelial and stromal signaling, those enriched in normal tissue involved neuropeptides, such as NPY and GCG (glucagon). Moreover, malignant-like regions 6 and 11 as well as region 2 (muscularis) were particularly enriched for active communication pathways (**Figure S8I** and **Supplementary item 4B**). This included the WNT signaling pathway, angiogenesis (VEGF, PDGF, FGF) and the OSM pathway.

Similar spatial patterns in human and mouse tumors

The overall spatial distribution of cell types and epithelial profiles was conserved between mouse and human tumors, when comparing to scRNA-seq[2,28,29,67–70]. We examined mouse-defined regions in human tumors, using TACCO to map the expression profiles associated with the epithelial, immune and stroma compartments in each of the TACCO-identified mouse regions to scRNA-seq profiles from human CRC, and probabilistically annotated region-specific expression profiles for each scRNA-seq profile from the human samples. This identified two main “meta compartments”, with epithelial, stromal and immune profiles from human MMRp and MMRd tumors associated with regions 6, 8 and 11 that were enriched in AV lesions (as well as 0 and 2), while those from normal human tissue were associated with normal regions (*e.g.*, 5, 10, 12) (**Figure 5A** and **Figure S9A**, **Methods**).

Malignant-like regions are associated with tumor progression in human colorectal tumors

We next assessed if the regional epithelial programs that we spatially identified in mouse are conserved in human. To this end, we constructed pseudo-bulk profiles from epithelial cells for our mouse samples and for recently published human samples profiled along different stages of malignant transformation, from normal tissue to polyp to CRC[2,28,29,67–70]. We scored each epithelial pseudo-bulk profile with the differentially expressed genes between the epithelial parts of the regions and computed the principal components of these scores across all human and mouse samples (**Methods**). The first principal component (PC1) captured features that are related to malignancy, with higher values for human tumors *vs*. polyps (**Figure 5B** and **Figure S9B**). In addition, malignant-like region (6/8/11) scores were higher in dysplastic *vs*. normal samples (**Figure 5C**). Thus, the spatial region profiles defined in mouse capture features that correlate with malignant transformation in human.

We further classified each full pseudo-bulk profile from the dysplastic human samples into one of the four groups in the CMS expression-based classification[71] (**Methods**) and compared the mouse region scores for each class of samples (**Figure S9C, Methods**). CMS2 classified samples were most closely related to our dysplastic mouse models: all of the dysplasia -associated regions were enriched in CMS2 tumors while most normal regions were depleted, relative to the other CMS classes.

Finally, we found that expression of the malignant like regions (6/8/11) in tumors was associated with clinical outcome. We scored each tumor based on genes that were differentially expressed between the full expression profile of malignant-like regions (6/8/11) and compared the progression-free interval (PFI) and overall survival (OS) for patients in TCGA whose RNA-seq profiles were in the top and bottom quartile of malignant-like region scores (**Methods**). High scores for malignant-like region 11 (EMT) were correlated with shorter PFI, while those for malignant-like region 6 (inflammation) correlate with longer PFI and longer OS, (**Figure 5D,E**).

These associations were driven primarily by MMRp tumors **(Figure S9D,E)**. This suggests that region 11 is associated with pro-tumorigenic properties in human patients, while region 6 might be associated with tumor controlling properties. This highlights the importance of multicellular functional tissue modules in the CRC tumor ecosystem.

DISCUSSION

Here, we systematically charted the spatial organization of cellular expression in dysplastic tissue of the colon, to help identify putative functional units in the tumor. We used TACCO[21] to integrate scRNA-seq and Slide-seq data, not only by mapping cell types to their positions, but also distinguishing different cell programs, the regions that they dominate, and their characteristic microenvironments. This allowed us to overcome technical limitations, such as lack of spatial context in scRNA-seq and sparse readout in Slide-seq, and to generate a high-resolution spatial map of the dysplastic landscape transcending beyond the mapping of individual cells to spatial positions. We used this map to show correlation with clinical outcome in human patient tumors.

Our scRNA-seq analysis revealed profound enrichment of a stem cell program in dysplastic tissues. The profiles of dysplastic cells expressing this program are distinct from normal stem cells and enriched with expression of negative regulators of the WNT signaling pathway and inflammation, suggesting a non-canonical function. The abundance of these cells with stemness potential across all our malignant-like regions, points to a dynamic population that can affect the cells in its proximity, by secretion of negative regulators of the WNT signaling and inflammatory function but may also adopt various functions depending on the environmental cues and dysplasia-associated cells in its proximity. A similar population, designated "high-plasticity cell state", was previously described in a mouse model of lung adenocarcinoma and in human patients, where it was correlated with resistance to chemotherapy[61]. Whether these cells can be manipulated to take on specific phenotypes or even to differentiate into normal-like enterocytes given the appropriate signal from the microenvironment, remain as open questions.

Within the dysplastic lesions, alongside malignant-like regions, we found regions with normal features (Regions 3,4,9,10), comparable to regions found in the normal colon, most likely representing compartments driven by clones that were not affected by the genetic perturbation. One of these regions, region 4, contained mainly goblet cells with normal expression profiles. Whether this neighborhood represents normal cells that reside alongside malignant cells or a cancer transition state, it may modify tumor progression, by recruiting immune cells or by secreting factors that affect epithelial proliferation in adjacent regions. For example, region 4 in dysplastic lesions is enriched with chemokine activity genes relative to region 4 in normal colon suggesting a possible role in recruitment of immune cells to the dysplastic landscape. Further work is required to understand the role of these regions (expressing normal features) in tumor progression.

While the malignant-like regions were identified as discrete spatial entities, each with coordinated features across epithelial, immune, and stromal cells, these regions are adjacent to each other. Thus, they may still influence one another through signaling or by utilizing branches of the same main vessels. For example, *Osm* is expressed by cells in region 6, whereas its receptor is expressed on fibroblasts and endothelial cells enriched in region 11. *OSMR* was previously shown to be expressed by inflammatory fibroblasts[44,72] and its activation in malignant cells promotes EMT in breast cancer and pancreatic cancer[73,74] and a mesenchymal state in glioblastoma[75]. Future studies can help determine if these regions are functionally inter-dependent and if they evolved from the same clones and can inter-convert, or whether they developed independently.

Because animal models complement cell and tissue atlases of human colorectal cancer[2,28], by allowing experimental manipulation for mechanistic studies[76,77], it is important to relate between models and patients. By studying genetically engineered mouse models using high resolution single cell spatial genomics we can help determine to what extent they recapitulate the cellular and spatial organization of human disease, in the context of two distinct genetic states that represent human CMS-2 lesions. To this end, we developed several approaches to allow cross species comparison of tumors at the single cell and spatial level, despite the high level of both intra- and inter-individual variation within each species. Comparing to human CRC, our analysis suggests that the CRC landscape is organized in similar multicellular functional tissue modules between human and mouse, and disease subtypes (*e.g.*, MMRp and MMRd). Future studies applying our approaches to patient cohorts could help understand whether the expression of different tissue modules may contribute to the partial response to immunotherapy reported for MMRd patients[78], and to define specific tissue modules predictive of response to therapy. Notably, while our study focused on the tumor landscape, its findings may be relevant for tissue response to other challenges (*e.g.*, inflammation, fibrosis, wound healing), which involve activation of similar functional tissue modules, a result of collective function of parenchymal, immune and stromal cells.

Taken together, our integrative approach facilitates spatial analysis with high resolution, constructing regional neighborhoods and their spatial layout at both high cellular resolution and genomic scale. Our work is an important step toward a systematic understanding of the organization of dysplastic tissue with the potential to contribute to improved patient stratification by the multicellular functional units in the tumor landscape.

Methods

Human subjects

The MGH Institutional Review Board approved protocols for tissue collection used for sequencing (Protocol 02-240). Informed consent was obtained from all subjects prior to collection. Only patients with primary treatment- naive colorectal cancer were included in this study.

Mice

Mice were housed in the animal facility at the Koch Institute for Integrative Cancer Research at MIT. All animal studies described in this study were approved by the MIT Institutional Animal Care and Use Committee (Protocol 1213-106-16). *Apc*$^{fl/fl}$ mice[79] were obtained from NCI mouse repository, *Kras*$^{LSL\text{-}G12D/+}$ Ref.[80], *Rosa26*$^{LSL\text{-}tdTomato}$ Ref.[81] and Trp53$^{fl/fl}$ Ref.[82] mice obtained from Jackson, *Villin*^{CreERT2} Ref.[83] mice were a gift from Dr. Sylvie Robine. All mice were maintained on C57BL/6J genetic background. Approximately equal numbers of male and female mice of 6–10 weeks of age were used for all experiments. Where indicated, mice were injected to the submucosal layer of the colon with 4-hydroxytamoxifen (EMD Millipore # 579002) dissolved in ethanol at a concentration of 100 µM (for the mice that were kept for 3 weeks after injection) or 30 µM (for the mice that were kept for 9 weeks after injection). Tumors were resected at either 3 or 9 weeks after 4-hydroxytamoxifen injection. Colonoscopy and colonoscopy-guided injection methods were previously described in detail[30,31].

Tissue processing for scRNA-seq

Single-cell suspensions from healthy colon or dysplastic lesions were processed using a modified version of a previously published protocol[44]. Tissue samples were rinsed in 30ml of ice-cold PBS

(ThermoFisher 10010-049), chopped to small pieces and washed twice in 25 ml PBS, 5mM EDTA (ThermoFisher AM9261), 1%FBS (ThermoFisher 10082-147). To prime tissue for enzymatic digestion, samples were incubated for 10 minutes at 37°C, placed on ice for 10 minutes before shaking vigorously 15 times followed by supernatant removal. Tissues were placed into a large volume of ice-cold PBS to rinse prior to transferring to 5ml of enzymatic digestion mix (Base: RPMI1640, 10 mM HEPES (ThermoFisher 15630-080), 2% FBS), freshly supplemented immediately before use with 100 mg/mL of Liberase TM (Roche 5401127001) and 50 mg/mL of DNase I (Roche 10104159001), and incubated at 37°C with 120 rpm rotation for 30 minutes. After 30 minutes, enzymatic dissociation was quenched by addition of 1ml of 100% FBS and 10mM EDTA. Samples were then filtered through a 40 mM cell strainer into a new 50 mL conical tube and rinsed with PBS to 30 mL total volume. Tubes were spun down at 400 g for 7 minutes, at 4°C. Resulting cell pellets were resuspended in 1ml PBS, placed on ice and counted.

Cell hashing

Cell hashing was performed based on the published protocol[84] as summarized below. Dissociated cells were resuspended in 1ml of Cell Hashing Staining Buffer (1× PBS with 2% BSA (New England Biolabs, B9000S) and 0.02% Tween (Tween®-20 Solution, 10%, Teknova, VWR-100216-360) and counted. 500,000 cells were resuspended in 100 µL of Cell Hashing Staining Buffer and incubated for 30 minutes on ice, with 2 µL of the appropriate BioLegend TotalSeq™ Hashing antibody (a 1:50 dilution, using a total of 1 µg of antibody per cell suspension). TotalSeq™-A anti-mouse Hashtag antibodies #1-8 (catalog numbers:155801, 155803, 155805, 155807, 155809, 155811, 155813, 155815) were used. Cells were washed three times with 0.5 mL of Cell Hashing Staining Buffer and filtered through low-volume 40-µm cell strainers. All cell suspensions were recounted to achieve a uniform concentration of 7,000 cells per microliter before pooling for capture by 10x Chromium controller following the manufacturer protocol for the v2 or v3 3' kit (10X Genomics, Pleasanton, CA).

Hashtag oligo (HTO) library preparation

Separation of hashtag oligo (HTO)-derived cDNAs (<180 bp) and mRNA-derived cDNAs (>300 bp) was done after whole-transcriptome amplification by performing 0.6× SPRI bead purification (Agencourt) on cDNA reactions as described in 10x Genomics protocol. Briefly, supernatant from 0.6× SPRI purification contains the HTO fraction, which was subsequently purified using 1.4 and 2× SPRI purifications per the manufacturer's protocol (Agencourt). HTOs were eluted by resuspending SPRI beads in 15 µL TE. Purified HTO sequencing libraries were then amplified by PCR (1µL clean HTO cDNA, 25µL 2X NEBNext Master Mix (NEB #M0541)), 10 µM SI-PCR and D701or D704 primers performed dial out PCR (98°C (10 sec), (98°C for 2 sec, 72°C for 15 sec) x 12/18 then 72°C for 1 min) for 12 and 18 cycles, and used the 18 cycles product for sequencing. PCR reactions were purified using another 2× SPRI clean up and eluted in 15 µL of 1× TE. HTO libraries were quantified by Qubit High sensitivity DNA assay (ThermoFisher) and loaded onto a BioAnalyzer high sensitivity DNA chip (Agilent).

SI-PCR: AATGATACGGCGACCACCGAGATCTACACTCTTTCCCTACACGACGC*T*C

D701:

CAAGCAGAAGACGGCATACGAGATCGAGTAATGTGACTGGAGTTCAGACGTGTGC

D704 :

CAAGCAGAAGACGGCATACGAGATGGAATCTCGTGACTGGAGTTCAGACGTGTGC

Sequencing

Samples were sequenced using HiSeq X (Illumina). Hashing libraries were sequenced with spike-ins of 2.5%.

Tissue processing for Slide-seq

Colons were flashed with cold PBS and a segment that includes the lesion and surrounding tissue (or a respective healthy segment from normal mice) was dissected. Samples were then mounted in cold OCT, flash frozen on dry ice covered with ETOH and long-term stored in -80°C.

Slide-seq

For mouse and human experiments, 10 μm sections were cut and the Slide-seq V2 protocol was used as previously described[15]. For mouse experiments, four and six arrays were collected from normal colons and AV lesions respectively. The muscularis was fit onto the array of both healthy and dysplastic lesions to allow appropriate orientation.

Multiplex *in situ* RNA Analysis

Multiplex *in situ* RNA analysis was performed with Cartana[33] technology (a newer version is now available as Xenium (10x Genomics)). In total we measured 3 samples with one section per sample in each state (normal/AV) and probe set (V1/V2), with an additional replicate section for one of the samples in normal V2.

Fresh Frozen OCT-embedded tissues from normal colon and AV lesions were cryosectioned as 10 μm sections and placed onto SuperFrost Plus glass slides (ThermoFisher) and further stored at -

80˚C before experiments. Samples were fixed (with 4% formaldehyde) for 5 minutes and permeabilized for 5 minutes (with 0,1 mg/mL pepsin in 0.1M HCl (P7012 Sigma-Aldrich)) prior to library preparation.

For library preparation, chimeric padlock probes (directly targeting RNA and containing an anchor sequence as well as a gene-specific barcode) for a custom panel of 66 (V1) or 180 (V2) genes (**Table S3**, see below) were hybridized overnight at 37°C, then ligated before the rolling circle amplification was performed overnight at 30°C using the HS Library Preparation kit for CARTANA technology and following manufacturer's instructions. All incubations were performed in SecureSeal^{TM} chambers (Grace Biolabs). Note that prior to final library preparation, optimal RNA integrity and assay conditions were assessed using Malat1 and Rplp0 housekeeping genes only using the same protocol.

To prevent tissue sections detachment, an additional baking step of 30 minutes at 37°C was performed before mounting. To quench autofluorescence background, TrueView (SP-8400 VectorLabs) was used for 1 minute at room temperature. For tissue sections mounting, Slow Fade Antifade Mountant (Thermo Fisher) was used for optimal handling and imaging.

Quality control of library preparation was performed by applying anchor probes to detect simultaneously all rolling circle amplification products from all genes in all panels. Anchor probes are labeled probes with Cy5 fluorophore (excitation at 650 nm and emission at 670 nm).
All samples passed quality control and went through *in situ* barcode sequencing, imaging and data processing. Briefly, adapter probes and sequencing pools (containing 4 different fluorescent labels:

Alexa Fluor® 488, Cy3, Cy5 and Alexa Fluor® 750) were hybridized to the padlock probes to detect the gene-specific barcodes, through a sequence specific signal for each gene specific rolling circle amplification product. This was followed by imaging and performed 6 times in a row to allow for the decoding of all genes in the panel. To reduce lipofuscin autofluorescence, 1X Lipofuscin Autofluorescence Quencher (Promocell) was applied for 30 seconds before fluorescence labeling.

Raw data consisting of 20x or 40x images from 5 fluorescent channels (DAPI, Alexa Fluor® 488, Cy3, Cy5 and Alexa Fluor® 750) were each taken as z-stack and flattened to 2D using maximum intensity projection. After image processing and decoding, the results were summarized in a csv file and gene plots were generated using MATLAB [85].

scRNA-seq pre-processing and quality control filtering

Count matrices for scRNA-seq were generated using the Cumulus feature barcoding workflow v0.2.0[86] with CellRanger v3.1.0 and the mm10_v3.0.0 mouse genome reference. Cell profiles were quality filtered by requiring between 1,000 and 50,000 counts, and between 500 and 7,000 genes, less than 20% mitochondrial counts, and less than 10% hemoglobin counts. Cell profiles that did not meet all these criteria were discarded. The top 5,000 highly variable genes were annotated on the remaining cells after normalization to 10,000 counts and log1p transform using Scanpy's “highly_variable_genes” function[87] and providing the chemistry (v2/v3) by hashing (True/False) combination as batch-annotation. Putative doublets were removed using Scrublet[88] with default parameters.

Selection of variable genes, dimensionality reduction and clustering

A preliminary clustering using the Leiden algorithm with resolution 1.0 was performed after normalization to 10,000 counts, log1p transform, correction for number of counts and percentage of mitochondrial genes, scaling with a max_value of 10, and generating a *k*-nearest neighbors (*k*-NN) graph with 15 neighbors on a PCA of the previously annotated 5000 highly variable genes with 50 components using Scanpy[87]. The single cell profiles were provisionally annotated with SingleR[89] cell-wise (i.e. without using clustering information) using the SingleR built-in MouseRNAseqData and an intestine specific dataset from Tabula Muris[90] (https://figshare.com/ndownloader/files/13092143). For further processing, the dataset was then split into the three compartments, epithelial, immune and stromal, using the provisional SingleR annotations.

For each compartment, the top 5,000 highly variable genes were annotated using Scanpy's "highly_variable_genes" function on cells normalized to 10,000 counts after log1p-transformation and providing the chemistry (v2/v3) by hashing (True/False) combination as batch-annotation.

Expression programs and batch correction

For the dataset of each compartment separately (generated as described above), an integrative NMF was performed (using a part of the LIGER[45] implementation) with k=20 and lambda=5 to identify 20 programs and their respective weights per cell. This iNMF factorization represents the single cell expression matrix as a weighted sum of profiles such that both the weights and programs contain only non-negative numbers, while allowing for and separating out batch-only contributions. The same approach was also used with a higher *k* (epithelial and immune: 200, stromal: 50) to yield a detailed and batch corrected decomposition of expression which was then combined to obtain a count-like corrected expression matrix for the top 5,000 highly variable genes. For each compartment separately, these batch-corrected data were normalized to 10,000 counts, log1p transformed, corrected for number of counts and percentage of mitochondrial genes by linear regression, scaled with a max_value of 10, followed by a PCA of the previously annotated 5,000 highly variable genes. A *k*-nearest neighbors (*k*-NN) graph was constructed from the top 50 PCs, with *k*=15 neighbors using Scanpy, and clustered using a compartment-specific Leiden resolution parameter (epithelial: 0.2, immune: 0.4, stromal: 0.1). This clustering was used as the cluster level annotation of the mouse scRNA-seq data for the epithelial and stromal compartment. Separately per compartment the data were annotated with SingleR using the cluster information. The same per-compartment batch-corrected and preprocessed data from the Leiden clustering was used to create UMAP embeddings with PAGA initialization using Scanpy.

To improve the clustering and annotation in the immune compartment and to filter out additional doublets not detected by Scrublet, the immune data were separately filtered and clustered using information from the compartment level clustering and annotation. To that end, myeloid and T/NK cells were partitioned separately and further processed, and additional likely doublet cells were labeled and removed by the following procedure:

1. Cells were labeled as doublets based on higher number of UMIs of marker genes for other compartments than the 95th percentile observed in this immune partition (*i.e.*, Epcam and Cdh1 to remove immune-epithelial doublets and Cav1 and Kdr to remove immune-stromal doublets) and other immune partitions (i.e., Cd3d, Cd3e, and Cd3g to remove myeloid-lymphoid doublets from the myeloid cells). This type of filter criterion for lowly expressed genes ("larger

than some percentile" on integer counts) also allows to keep more than 95% of the cells if, for example, all cells of this partition happened to have 0 UMIs of a particular marker gene.

2. Cells were labeled as doublets if they had inconsistent cell-wise and cluster-wise SingleR annotations.
3. Cells were labeled as doublets if they had significantly (Benjamini-Hochberg FDR=0.05, one-sided Fisher's exact test) more neighbors in the k-NN graph from the immune compartment that were already marked as doublets.
4. All cells labeled as doublets were removed.

After filtering, the count matrices were batch corrected as above using the integrative NMF from LIGER with k=20 and lambda=5, and clustered like above with group specific Leiden resolution (myeloid: 0.2, TNK: 0.4). For myeloid and TNK cells, this clustering superseded the original clustering. The integrative NMF result here was only used for updating the clustering and not for generating an extra set of expression programs.

Note that cluster Epi06 shows a broad expression spectrum; while such pattern can best be explained by remaining doublets, they were not called by Scrublet and could also not be consistently removed by extra QC as was applied to the immune compartment. The interpretation of Epi06 as containing doublets is supported by its overrepresentation in the annotation of the Slide-seq data (Figure S6E), as both doublets and slide-seq beads represent compositions of different cells. Still, non-doublet explanations (e.g. undifferentiated cells) cannot be ruled out. Therefore, Epi06 cells are retained in the data but not interpreted biologically.

Marker selection for *in situ* RNA analysis (CARTANA)

CARTANA V1 markers were selected from genes differentially expressed between compartments, cell types and clusters (for the immune and stromal compartments), and highly ranked genes for programs (for the epithelial compartment) were first filtered by biological relevance and the literature, obtaining 87 genes. To further reduce the set to the available panel size (66 genes), genes were annotated into categories of potential redundancy. To choose between redundant genes, a global objective function was optimized over the gene selection, looping over all potentially redundant gene sets until convergence, exhaustively testing all choices within a gene set, and accepting the best choice for this gene set in terms of the global objective function. The global objective function was constructed as the mean 4-fold cross-validation scores (using “GroupKFold” and “cross_val_score“ from sklearn[91]) of multi-class logistic regression classification (using “LogisticRegression” from sklearn) for discriminating cell classes and of ridge regression of epithelial program weights (using “RidgeRegression” from sklearn) on the scRNA-seq data subsampled to the expected sparsity of CARTANA data. The cell classifications used were between the stromal, immune, and epithelial compartment, within the stromal compartment between Endo01, Endo02, and fibroblasts, within the immune compartment between myeloid and lymphoid lineage, within the lymphoid lineage between T cells and B cells, within the myeloid lineage between granulocytes, mast cells, and all monocytes and macrophages together, between monocytes and macrophages, and within monocytes between Mono01, Mono02, Mono03, and Mono04. The programs used in ridge regression were programs 3, 4, 6, 7, 13, 14, 15, and 16. As the probes for Ly6c1 and Ly6c2 could not discriminate sufficiently between Ly6c1 and Ly6c2, we chose combined probes that measure both.

The CARTANA V2 panel, included 59 of the 66 genes in the V1 panel (the others had to be removed for technical reasons), another 113 genes from the standard fixed gene panel for CARTANA, and 8 selected genes from literature.

Analysis of CARTANA data

Each measured molecule was annotated with an originating cell type cluster label (using TACCO's "tc.tl.annotate_single_molecules", with RCTD[19] as the core annotation method and parameters bin_size=20, n_shifts=3, assume_valid_counts=True) separately for each sample. For this, genes in the reference that would likely cross hybridize in the probe panel design were summed over (Ly6c1 and Ly6c2). TLS-like regions were annotated by visual inspection of the cell type cluster composition and morphology.

To assess cell type compositions of the full dataset, molecules with cell type cluster annotations were binned into 10µm bins (using TACCO's "tc.utils.bin" and "tc.utils.hash" functions) and cluster-level annotations were merged to cell-type level.

To assess the compositions of TLS-like regions, CARTANA v2 data were aggregated, conserving the categorical TLS annotation (using TACCO's "tc.utils.bin" and "tc.tl.dataframe2anndata" functions).

Comparison between experimental methods

To compare cell type composition between methods, CLR-transformed compositions of samples (or of spatially split samples for the spatial methods, see subsection "Ligand-Receptor Analysis and Spatially Informed Enrichment") were computed. Then, using a 100 bootstrapped means of the compositions, mean and standard error of the mean were calculated once for the AV and once for the normal samples. To compare gene expression, the mean difference of gene counts between normal and AV samples and its standard error were calculated using all pairwise differences between the bootstrapped normal and AV samples. For gene comparisons, the CLR-transformed composition over all genes that were measured in all of scRNA-seq, Slide-seq, CARTANA V1, and CARTANA V2 was used. Pearson correlation between mean compositions was calculated for each pair of methods.

RNA-velocity analysis

Splicing aware count matrices for scRNA-seq were generated using CellRanger v6.1.2 and velocyto v0.17.17[37] with the ensembl v108 mouse genome reference. Scvelo v0.2.5 was used to infer velocity separately for the epithelial and TNK subsets (using the functions “scv.pp.filter_and_normalize”, “scv.pp.moments”, “scv.tl.velocity” (with mode='stochastic'), and “scv.tl.velocity_graph”). Scanpy and bbknn v1.5.1[92] were used to generate batch-corrected UMAP embeddings for the two subsets for visualization with scvelo’s “scv.pl.velocity_embedding_stream” function.

Selection of human single cell data for the comparison of cell type and epithelial program composition

ScRNA-seq data from Ref[2] was used as reference for human CRC. To avoid biases in cell type compositions, only the subset of the data where "PROCESSING_TYPE = unsorted" were used.

Comparison of human and mouse samples by cell type composition

To compare human and mouse samples by composition of T/NK cell subsets, T/NK annotations from mouse and human data[2] were matched by TACCO, using optimal transport (OT). First, human expression data were mapped to mouse genes using MGI homology information [subsection "Mapping of mouse and human orthologs"]. Then, human cell cluster annotations ('cl295v11SubFull') were mapped from the subset of human cells annotated as T/NK/ILC to the subset of mouse cells annotated as T/NK using TACCOs "annotate" function with OT as core method, basic platform normalization, entropy regularization parameter epsilon 0.005, marginal relaxation parameter lambda of 0.1, and 4 iterations of bisectioning with a divisor of 3. Annotation with maximum probability per cell was used as the unique cluster level annotation for mouse T/NK cells. Annotations were aggregated per sample to yield a compositional annotation over the identical cluster annotation categories (from the human dataset) for the T/NK subsets of human and mouse samples. Annotation vectors were then processed using the sc.pp.neighbors and sc.tl.umap functions from Scanpy[87] to yield a 2D sample embedding with respect to T/NK cell composition. Using the coordinates in the UMAP in place of spatial coordinates, neighborship enrichment z-scores were computed with TACCO's co_occurrence_matrix function with max_distance=2 and n_permutation=100.

Slide-seq compositional annotation

Slide-seq data were annotated with scRNA-seq reference annotations. First, Slide-seq and scRNA-seq data were filtered to retain only 15759 genes that were detected in both datasets and only beads and cells that had at least 10 counts across all these common genes.

Next, TACCO[21] was used to perform compositional annotation of each bead, allowing the bead counts to be explained by fractional contributions. In its basic application, TACCO finds an "optimal" mapping between scRNA-seq annotation categories (*e.g.*, cell types) and beads by solving a variant of an entropically regularized Optimal Transport (OT) problem in expression space. In its iterative application, TACCO uses a bi-sectioning functionality iteratively, annotating only fractions of the counts in each round, and reserving the remainder for the next round to improve the sensitivity to sub-leading annotation contributions (that is, first capture a portion of the counts for the "top" cell types, but preserving others for other, more minor, cell types).

For the compositional annotation of Slide-seq beads with the categorical cell clusters from the single cell data, the "annotate" function of TACCO with OT was used as core annotation method per Slide-seq puck with the subset of the single cell data with matching disease state, with basic platform normalization, entropy regularization parameter epsilon 0.005, marginal relaxation parameter lambda of 0.001, and 4 iterations of bisectioning with a divisor of 3.

For the compositional annotation of Slide-seq beads with the compositional epithelial programs, the annotated beads were split using the "split_observations" function of TACCO on the cluster-level annotation and then aggregated to compartment level using the "merge_observations" function keeping only beads for a compartment with at least 50 counts assigned to that compartment. The genes from the epithelial part were filtered to retain only those that were used to define the epithelial programs in scRNA-seq, and then annotated using again the "annotate" function with OT as core annotation method, basic platform normalization, entropy regularization parameter epsilon 0.01, and a marginal relaxation parameter lambda of 0.001.

Slide-seq region annotation

Region annotation was done for all pucks (normal and AV pucks) in one step to get comparable region annotations across pucks, such that beads that have similar epithelial program activity and are spatially close are called as one region. Because cell type composition can change drastically from one bead to its neighbor at the length scales of Slide-seq data, there is a need to compromise between optimizing the two similarities. This is done with the "find_regions" function of TACCO, which performs a Leiden clustering on the weighted sum of connectivity matrices derived from epithelial program similarity and spatial proximity, using a position weight of 0.7, a Leiden resolution of 1.3, and 15 nearest neighbors per bead in position space and epithelial program space. To determine the neighbors in epithelial program space, the square-roots of the program weights were used for neighbor finding which effectively uses Bhattacharyya coefficients as overlap in epithelial program space instead of the Euclidean scalar products used for position space. These regions are defined by construction only on beads with a large enough epithelial contribution (see above) and are then extended to all beads by assigning unannotated beads the region from the nearest bead with region annotation.

Submucosal and muscularis propria layers are predominantly comprised of fibroblasts and muscle cells, respectively, alongside blood and lymphatic vessels, nerves and immune cells. Our algorithm depends on the epithelial expression component in beads. Since these layers do not contain epithelial cells[93], mapping likely relied either on "noisy" signal from non-epithelial cells or from the basal-most epithelial layer.

To determine region composition at a certain distance of a reference region, TACCO's "annotation_coordinate" function is used with max_distance=1000 and delta_distance=10.

Slide-seq quality filtering

For all downstream analyses, all beads with less than 100 reads were discarded.

Region- and cell type- characterizing genes in Slide-seq data

Genes to characterize regions on Slide-seq pucks irrespective of compartment composition were found using Scanpy's rank_genes_groups function on the full bead expression profiles. To find them separately for each compartment, the compartment-level split beads [sub-section "Slide-seq annotation"] were used instead of the full beads. To compare gene expression between cell types on Slide-seq pucks, cluster-level split beads [sub-section "Slide-seq annotation"] were aggregated to cell type level.

EMT scoring

Malignant regions were scored for EMT signatures, using only counts attributed to the epithelial compartments within these regions and only genes expressed on at least 3 beads. Bead profiles were normalized to 10,000 counts, log1p transformed and scaled, and Scanpy's "sc.tl.score_genes" function was used to score the top 50 genes in two EMT gene signatures[61,94].

Cell-type neighborships in Slide-seq data

To evaluate the local cell-type neighborship relations in the different disease states on the cluster level, the clusters were filtered per disease state to contain only clusters which account for at least 1% of the UMIs in that state. Then neigbourhood-enrichment z-scores were calculated using TACCO's "co_occurrence_matrix" function with max_distance=20 and n_permutation=10. To evaluate the stability of the result, this is also repeated for (max_distance, n_permutation)=(40,10),(60,10),(20,5), and (20,50). To get the significance of the overall change in z-scores between the states, a one-sided Mann-Whitney-U test was performed on the values of the upper triangular half of the matrix between the two disease states for (max_distance, n_permutation)=(20,10).

A similar neighborship analysis was performed on the coarser cell-type level separately for the three malignant regions 6, 8, and 11, using TACCO's "co_occurrence_matrix" function with max_distance=20 and n_permutation=10.

Cell-type co-occurrence in Slide-seq data

Cell-type compositions relative to a spatial landmark, Region 2=muscularis, were evaluated using TACCO's "annotation_coordinate" function with max_distance=1000 and delta_distance=10. To reduce tissue structure bias from the muscularis, the distance dependency of cell-type frequency relations was evaluated only for beads deep in the "epithelial domain", defined as follows. The effective distance from stromal annotation was computed using TACCO's "annotation_coordinate" function (with max_distance=100, delta_distance=10, critical_neighbourhood_size=4.0) and only beads with a distance of at least 75µm were used. On these remaining beads, TACCO's "co_occurrence" function was used (with delta_distance=20, max_distance=1000) to compute cell types co-occurrence as a function of their distance.

Epithelial program neighborships in Slide-seq data

As for cell types above, neighborship relations were evaluated for epithelial programs in the AV Slide-seq samples using TACCO's "co_occurrence_matrix" function with max_distance=20 and n_permutation=10, after selecting only the programs which make up at least 1% of the UMIs in the AV Slide-seq samples.

Ligand-Receptor analysis and spatially informed enrichment

For the ligand-receptor analysis on slide-seq data we used COMMOT v0.03[66]. COMMOT employs optimal transport to construct sender and receiver side receptor-ligand interactions for every bead in one run of COMMOT. After filtering to beads with at least 100 counts, we applied basic preprocessing (normalization, log1p-transformation) and load the CellChat database as done in the COMMOT tutorial (https://commot.readthedocs.io/en/latest/notebooks/Basic_usage.html). We then follow the Slide-Seq v2 analysis from the COMMOT paper ("slideseqv2-mouse-hippocampus/1-lr_signaling.ipynb" from https://doi.org/10.5281/zenodo.7272562) to filter the database and to reconstruct the spatial communication network on ligand-receptor pair and pathway level separately for every puck. In particular, we use the distance cutoff of 200µm for inference of ligand-receptor interactions. The resulting bead-wise sender- and receiver communication values were then used for enrichment analysis between disease states and between spatial regions.

Unlike the downstream Slide-Seq v2 analysis from the COMMOT paper ("slideseqv2-mouse-hippocampus/2-downstream_analysis.ipynb" from https://doi.org/10.5281/zenodo.7272562), we do not treat each bead on the puck as statistically independent observation in statistical tests, which leads to unreliably small p-values. Instead, we split all pucks along their axis of greatest extent (defined by the first principal component axis of the distribution of the spatial measurements) into spatial patches discarding 400µm of boundary layer (twice the COMMOT distance cutoff, also co-occurrences have decayed strongly at this distance) in between the patches to reduce the correlation between the patches. This is done iteratively with the patches to get a set of weakly correlated patches. On these patches we calculate the mean of the communication values and treat them as statistically independent observations for statistical tests. We argue that multiple sufficiently separated spatial patches of single spatial samples can be seen as multiple spatial samples using a spatial method with a smaller measurement area, and therefore can be treated as replicates. Unlike splitting into patches without removing a boundary layer, this procedure does not converge to the case of treating each bead as an independent observation as the number of iterations rises as it accounts for the spatial correlations between adjacent measurements. This gives a natural lower limit of p-values reachable with p-values rising again if too many splits are performed as too much data is lost to remove the correlations (**Supplementary item 4C,D**). We chose a number of iterations of 2 as a compromise between having more patches and not discarding much data. For the enrichment of the pathway communication values we used a two-sided Mann-Whitney U test across the patches and cite Benjamini-Hochberg FDR values. For the enrichment testing in a given group (e.g. an annotated spatial region) only those patches are used which have at least 100 beads on the patch.

Unless otherwise noted, for consistency, an analogous enrichment procedure was also used for COMMOT-unrelated quantities, like cell types, even though their spatial footprint is not as large as COMMOT’s (distance cutoff of 200µm). For cluster-level cell type enrichment analyses on Slide-seq data, only the top 3 contributing subtypes were considered, to better reflect the expected properties of Slide-seq data and better compare with categorically annotated scRNA-seq data.

Mapping of mouse and human orthologs

We applied TACCO's functions "setup_orthology_converter" and "run_orthology_converter" with option "use_synonyms=True" to map human to mouse genes using the ortholog mapping from Mouse Genome Informatics (http://www.informatics.jax.org/homology.shtml). Specifically we used http://www.informatics.jax.org/downloads/reports/HOM_MouseHumanSequence.rpt (downloaded April 26th, 2021) for the analyses comparing T/NK compositions of human and mouse scRNAseq data, analyses comparing epithelial program similarity in human and mouse scRNAseq data, analyses involving the annotation of human scRNA-seq data with mouse regions, and analyses comparing the cell type and epithelial program correlations cross samples between human and mouse scRNA-seq data, and http://www.informatics.jax.org/downloads/reports/HOM_AllOrganism.rpt (downloaded on August 8th, 2022) for the analyses involving the scoring of mouse regions in mouse and human scRNA-seq data and leading to the CMS classification.

GO term enrichment analysis

We used TACCO's functions "setup_goa_analysis" and "run_goa_analysis" to perform GO terms enrichment. As "gene_info_file" we used https://ftp.ncbi.nih.gov/gene/DATA/GENE_INFO/Mammalia/Mus_musculus.gene_info.gz, as "GO_obo_file" http://purl.obolibrary.org/obo/go/go-basic.obo, and as "gene2GO_file" https://ftp.ncbi.nih.gov/gene/DATA/gene2go.gz (all downloaded on August 10th, 2022).

Comparison between mouse and human programs

To compare mouse and human epithelial expression programs[2], genes were mapped to mouse homologs using MGI homology information [subsection "Mapping of mouse and human orthologs"]. Mouse and human programs were then characterized by a single vector of mean expression per program in mouse gene space. Specifically, both mouse and human programs were defined such that their weighted sum approximates the expression profiles of the cells without any transformations. Programs and weights were normalized to sum to 1. To reduce batch-effects (including species-specific ones), a background expression profile was defined for each species dataset as the pseudo-bulk epithelial expression profile in the respective scRNAs-seq data. Program and background profiles were normalized to 10,000 counts and the log ratio of the normalized program and background expression vectors was used to define a vector for each species. Pearson correlation coefficients were calculated for each pair of program vectors (mouse vs. human).

Human expression program associations across mouse scRNA-seq

All sets of programs that were previously used to define human CRC tissue hubs[2] (epithelial, T/NK cells and myeloid cells) were mapped to mouse genes with MGI homology information [subsection "Mapping of mouse and human orthologs"] and then to mouse single cell data with TACCO, using TACCOs platform normalization to account for batch effects. The "annotate" function in TACCO was used with OT as the core annotation method, on the comparable subsets of cells from mouse and human single-cell datasets (*e.g.*, myeloid cells from mouse and human), with basic platform normalization, entropy regularization parameter epsilon 0.005, marginal relaxation parameter lambda of 0.1, and 4 iterations of bisectioning with a divisor of 3, and flat annotation prior distribution. The resulting probabilistic per-cell program annotations were aggregated to get probabilistic per-sample program annotations for all dysplastic mouse samples and CLR-transformed. For each pair of programs, the Pearson correlation coefficient was calculated on these transformed values.

Annotating human scRNA-seq data with mouse-derived region information

Human scRNA-seq profiles[2] were mapped to mouse gene space using MGI homology information [subsection "Mapping of mouse and human orthologs"]. Working in the same expression space, the "annotate" function in TACCO with OT as core annotation method was used on the full human scRNA-seq and mouse Slide-seq dataset with basic platform normalization, entropy regularization parameter epsilon 0.005, marginal relaxation parameter lambda of 0.1, and 7 iterations of bisectioning with a divisor of 3, and 10-fold sub-clustering of the region annotations. The region transfer is done separately per compartment, with the Slide-seq compartment split as described above and the human scRNA-seq data split using the cell type annotation of the data. For validation, mapping was also performed with mouse scRNA-seq data, as well as mapping the region information from the mouse pucks back to themselves.

To test for enrichments of region annotations across disease state, region composition was aggregated to sample-level (for Slide-seq to 4-way split pucks), CLR-transformed, and enrichment was calculated using a two-sided Welch's t-test. This was done for region annotation on human and mouse scRNA-seq data, and on the original and mapped region annotation on the mouse Slide-seq data.

Cell-type associations across samples

To compare associations of cell types across samples in human and mouse scRNA-seq the "clMidwayPr” cell type annotation in the human data[2] was aggregated to the same level as mouse cell type annotation, and then aggregated per sample and CLR-transformed. Pearson correlation coefficients were calculated for every cell type pair for different subsets of samples: all samples, normal samples, dysplastic, and for human MMRd/MMRp samples.

Epithelial program associations across human samples

To determine epithelial program associations across human samples, TACCO’s “annotate” function was used to annotate human epithelial scRNA-seq (after mapping to mouse orthologs using MGI homology information [subsection “Mapping of mouse and human orthologs”]) with mouse epithelial programs from mouse scRNA-seq data using OT as core method, basic platform normalization, entropy regularization parameter epsilon 0.005, marginal relaxation parameter lambda of 0.1, and 4 iterations of bisectioning with a divisor of 3. The remaining steps were performed as for cell-type association (subsection “Cell-type associations across samples”).

Scoring epithelial mouse regions in mouse and human epithelial pseudo-bulk data

The published processed and filtered count matrices were used (where available) or instead raw count matrices for single cell/nucleus RNA seq data from Pelka[2] (GEO accession number GSE178341; downloaded on August 8th, 2022), Chen[28] (Synapse IDs syn27056096, syn27056097, syn27056098, syn27056099; downloaded on August 5th, 2022), Khaliq[69] (GEO accession number GSE200997; downloaded on August 5th, 2022), Becker[29] (GEO accession number GSE201348; downloaded on August 5th, 2022), Zheng[68] (GEO accession number GSE161277; downloaded on August 5th, 2022; excluding 'blood' samples), Che[67] (GEO accession number GSE178318; downloaded on August 5th, 2022; only 'CRC' and 'LM' samples) and Joanito[70] (Synapse IDs syn26844072, syn26844073, syn26844078, syn26844087, syn26844111; downloaded on August 22nd, 2022; excluding the ‘LymphNode’ sample).

To subset the human single cell data to epithelial cells, the epithelial annotation was used where readily available[2,28]. For the remaining datasets[29,67–70], TACCOs tc.tl.annotate function was used with default parameters to transfer the 'cl295v11SubShort' annotation from Pelka[2], from which a compositional compartment annotation was constructed, and then a cell was assigned to the epithelial compartment if it had more than 95% epithelial fraction.

To correct for batch effects between the different data sources, first batches were defined by species times protokoll: 'mouse-10x3p', 'mouse-SlideSeq', 'human-10x3p'[2,67,68,70], 'human-10x5p'[69,70], 'human-inDrop'[28], and 'human-snRNA'[29]. Then TACCO's "tc.pp.normalize_platform" function was used to determine per gene batch normalization factors using only the normal samples of one data source per batch (choosing the normal samples from Zheng for 'human-10x3p' and the normal 5’ samples from Joanito for 'human-10x5p'). The resulting factors are then used to rescale the sample-by-gene count matrices for the full dataset per batch, i.e. including non-normal samples. The normalization factors are calculated with respect to an (arbitrarily chosen) normal reference dataset[68].

The epithelial mouse region score was defined as the mean of the CLR-transformed expression values in the pseudo-bulk expression profile of the epithelial part of a dataset using the top 200 differentially expressed genes between all regions by a one-sided Fisher’s exact test.

To account for species-specific biases (in-set *vs*. out-of-set prediction: the DEGs are calculated in mouse), the scores per region across samples were zero-centered and scaled to unit variance across all samples (including normal and non-normal samples and all batches) per species. A Principal Components Analysis (PCA) of the region scores across all species, batches and samples was conducted and the values for the first PC were compared between different conditions using a two-sided Mann-Whitney U test with Benjamini-Hochberg FDR.

Assessing the relationship between mouse regions and CMS tumor classification

We used the package 'CMSclassifier' (https://github.com/Sage-Bionetworks/CMSclassifier) referred to in Ref.[71] to classify human pseudo-bulk CRC profiles from all samples which were not normal or unaffected from the human studies above into CMS classes. We determine the enrichment (Benjamini-Hochberg FDR, two-sided Welch's t test) of the same mouse region scores in the CMS classes.

Assessing the relation between mouse regions and clinical endpoints in human bulk RNA-seq

Published RNA-seq data from the COAD and READ cohorts of TCGA PanCancerAtlas[95] were used. Mouse region scores were defined as the mean of the log1p-transformed, zero-centered and scaled expression values in the bulk expression profile using the top 200 differentially expressed genes between the malignant mouse regions (6, 8, 11) by a one-sided Fisher’s Exact test (comparing each of the three regions to the other two). Scores were stratified into quartiles. PFI and OS was compared between patients with tumors whose scores were in the lowest and highest quartiles using the Logrank test as implemented in the lifelines package[96], followed by Benjamini-Hochberg FDR.

Compositional enrichment analyses

Enrichments on compositional data (cell type compositions, etc.) were evaluated with a two-sided Welch's t test on sample level using CLR-transformed compositions followed by Benjamini-Hochberg FDR. For the enrichment of tdTomato, counts and ALR-transformation were used instead with all non-tdTomato counts used as reference compartment. Enrichment analyses were performed using TACCO's "enrichments" function.

Code availability

The analysis code is available on GitHub (https://github.com/simonwm/mouseCRC).

Data availability

All data generated in this project is deposited on the Single Cell Portal and is available under the accession SCP1891 (https://singlecell.broadinstitute.org/single_cell/study/SCP1891). The raw scRNA-seq and Slide-seq data is also deposited on GEO under the GSE260801 (https://www.ncbi.nlm.nih.gov/geo/query/acc.cgi?acc=GSE260801). The public human scRNA-seq datasets can be found on GEO under accession numbers GSE178341, GSE200997, GSE201348, GSE161277, GSE178318 and on Synapse under the IDs syn27056096, syn27056097, syn27056098, syn27056099, syn26844072, syn26844073, syn26844078, syn26844087, syn26844111.

ACKNOWLEDGEMENTS

We thank N. Friedman, I. Benhar, N. Habib, M. Biton, K. Geiger-Schuller, J.C. Hütter, B. Dumitrascu, E. Baker and A. Greenwald for helpful discussions. We thank C. McCabe, O. Kuksenko and I. Barrera for technical assistance. We thank P. Yadollahpour, E. Dhaval, G. Smith-Rosario, S. Vickovic, D. Schapiro, S. Farhi, D. Abbondanza, A. Segerstolpe and T. Biancalani for their important contribution to this project. We thank L. Gaffney and A. Hupalowska for help with figure preparation. S.M. was supported by a DFG research fellowship (MA 9108/1-1), J.K. was supported by a HFSP long term fellowship (LT000452/2019-L), A.R. was a Howard Hughes Medical Institute (HHMI) Investigator when conducting this work. Work was supported by the Klarman Cell Observatory, a CEGS grant (5RM1HG006193-09) from the NHGRI, the NIH/NIAID (grants 1U24 CA180922, 1U19 MH114821, 1RC2 DK114784), the MIT Ludwig Center, the Manton Family Foundation, and HHMI (A.R.); Azrieli Foundation Early Career Faculty Fellowship, and an ISF Research Grant (1079/21) (M.N.), the Center for Interdisciplinary Data Science Research at the Hebrew University of Jerusalem (N.M. and M.N.), the Israeli Council for Higher Education Ph.D. fellowship (N.M.), SU2C Peggy Prescott Early Career Scientist Award PA-6146, SU2C Phillip A. Sharp Award SU2C-AACR-PS-32 and NIH/NCI R00CA259511 (K.P.), NIH/NCI R01 CA208756; Arthur, Sandra, and Sarah Irving Fund for Gastrointestinal Immuno-Oncology (N.H.), NIH/NCI R01CA257523, MIT Stem Cell Initiative (Foundation MIT) (O.Y.), and NIH R37CA259363, R21CA256414, R21DK125911, R41EB032693, R01CA254108, R01CA256530, and R01CA244359; DOD W81XWH-20-1-0203; and a Duke-NC State Translational Research Grant (J.R.). The authors gratefully acknowledge LMU Klinikum for providing computing resources on their Clinical Open Research Engine (CORE) and the

Bioinformatic Core Facility of the Biomedical Center Munich for providing computing resources on their HPC system.

AUTHOR CONTRIBUTIONS

I.A-D. and A.R. conceived the study and designed experiments. I.A-D. J.R., S.Y., E.M., T.D., L.C. and D.D. performed experiments, with guidance from O.Y. and A.R.. S.M., J.K., and N.M. developed computational approaches and analyzed data with I.A-D., M.H., E.M. and R.S, and with guidance from M.N. and A.R.. M.H., E.M., J.C., K.P., A.M. and G.M.B. generated and analyzed human data, with guidance from N.H., I.T., N.H., F.C., O.Y., O.R-R, and A.R.. A.N. and H.X. generated and processed the multiplex *in-situ* RNA data, with guidance from J.L. and M.R.. M.N and A.R provided supervision and acquired funding. I.A-D., S.M., M.N. and A.R. wrote the manuscript with input from all authors.

DECLARATION OF INTERESTS

A.M. has served a consultant/advisory role for Third Rock Ventures, Asher Biotherapeutics, Abata Therapeutics, ManaT Bio, Flare Therapeutics, venBio Partners, BioNTech, Rheos Medicines and Checkmate Pharmaceuticals, is currently a part-time Entrepreneur in Residence at Third Rock Ventures, is an equity holder in ManaT Bio, Asher Biotherapeutics and Abata Therapeutics, and has received research funding support from Bristol-Myers Squibb. G.M.B. has sponsored research agreements with InterVenn Biosciences, Palleon Pharmaceuticals, Olink Proteomics, and Teiko Bio. G.M.B. is a consultant for Ankyra Therapeutics and InterVenn Bio. G.M.B. has been on scientific advisory boards for Merck, Iovance, Nektar Therapeutics, Instil Bio, and Ankyra Therapeutics. G.M.B. holds equity in Ankyra Therapeutics. J.L. and M.R. hold equity in 10xGenomics. N.H. holds equity in BioNTech and is a founder of Related Sciences/DangerBio.

F.C. is a founder and holds equity in Curio Biosciences. O.Y. holds equity and is a SAB member of AVA Lifesciences. A.R. and O.R.-R. are co-inventors on patent applications filed by the Broad Institute for inventions related to single cell genomics. O.R.-R. has given numerous lectures on the subject of single cell genomics to a wide variety of audiences and in some cases, has received remuneration to cover time and costs. O.R.-R. is an employee of Genentech since October 19, 2020 and has equity in Roche. A.R. is a co-founder and equity holder of Celsius Therapeutics, an equity holder in Immunitas, and was an SAB member of ThermoFisher Scientific, Syros Pharmaceuticals, Neogene Therapeutics and Asimov until July 31, 2020. From August 1, 2020, A.R. is an employee of Genentech and has equity in Roche.

References

1. McAllister, S.S., and Weinberg, R.A. (2014). The tumour-induced systemic environment as a critical regulator of cancer progression and metastasis. Nat. Cell Biol. *16*, 717–727.

2. Pelka, K., Hofree, M., Chen, J.H., Sarkizova, S., Pirl, J.D., Jorgji, V., Bejnood, A., Dionne, D., Ge, W.H., Xu, K.H., et al. (2021). Spatially organized multicellular immune hubs in human colorectal cancer. Cell *184*, 4734-4752.e20.

3. Wagner, J., Rapsomaniki, M.A., Chevrier, S., Anzeneder, T., Langwieder, C., Dykgers, A., Rees, M., Ramaswamy, A., Muenst, S., Soysal, S.D., et al. (2019). A Single-Cell Atlas of the Tumor and Immune Ecosystem of Human Breast Cancer. Cell *177*, 1330-1345.e18.

4. Hunter, M.V., Moncada, R., Weiss, J.M., Yanai, I., and White, R.M. (2021). Spatially resolved transcriptomics reveals the architecture of the tumor-microenvironment interface. Nat. Commun. *12*, 1–16.

5. Keren, L., Bosse, M., Marquez, D., Angoshtari, R., Jain, S., Varma, S., Yang, S.-R., Kurian, A., Van Valen, D., West, R., et al. (2018). A Structured Tumor-Immune Microenvironment in Triple Negative Breast Cancer Revealed by Multiplexed Ion Beam Imaging. Cell *174*, 1373-1387.e19.

6. Schürch, C.M., Bhate, S.S., Barlow, G.L., Phillips, D.J., Noti, L., Zlobec, I., Chu, P., Black, S., Demeter, J., McIlwain, D.R., et al. (2020). Coordinated cellular neighborhoods orchestrate antitumoral immunity at the colorectal cancer invasive front. Cell *182*, 1341-1359.e19.

7. Jackson, H.W., Fischer, J.R., Zanotelli, V.R.T., Ali, H.R., Mechera, R., Soysal, S.D., Moch, H., Muenst, S., Varga, Z., Weber, W.P., et al. (2020). The single-cell pathology landscape of breast cancer. Nature *578*, 615–620.

8. Jerby-Arnon, L., Shah, P., Cuoco, M.S., Rodman, C., Su, M.-J., Melms, J.C., Leeson, R., Kanodia, A., Mei, S., Lin, J.-R., et al. (2018). A Cancer Cell Program Promotes T Cell Exclusion and Resistance to Checkpoint Blockade. Cell *175*, 984-997.e24.

9. Grünwald, B.T., Devisme, A., Andrieux, G., Vyas, F., Aliar, K., McCloskey, C.W., Macklin, A., Jang, G.H., Denroche, R., Romero, J.M., et al. (2021). Spatially confined sub-tumor microenvironments in pancreatic cancer. Cell *184*, 5577-5592.e18.

10. Goltsev, Y., Samusik, N., Kennedy-Darling, J., Bhate, S., Hale, M., Vazquez, G., Black, S., and Nolan, G.P. (2018). Deep Profiling of Mouse Splenic Architecture with CODEX Multiplexed Imaging. Cell *174*, 968-981.e15.

11. Angelo, M., Bendall, S.C., Finck, R., Hale, M.B., Hitzman, C., Borowsky, A.D., Levenson, R.M., Lowe, J.B., Liu, S.D., Zhao, S., et al. (2014). Multiplexed ion beam imaging of human breast tumors. Nat. Med. *20*, 436–442.

12. Giesen, C., Wang, H.A.O., Schapiro, D., Zivanovic, N., Jacobs, A., Hattendorf, B., Schüffler, P.J., Grolimund, D., Buhmann, J.M., Brandt, S., et al. (2014). Highly multiplexed imaging of tumor tissues with subcellular resolution by mass cytometry. Nat. Methods *11*, 417–422.

13. Ståhl, P.L., Salmén, F., Vickovic, S., Lundmark, A., Navarro, J.F., Magnusson, J., Giacomello, S., Asp, M., Westholm, J.O., Huss, M., et al. (2016). Visualization and analysis of gene expression in tissue sections by spatial transcriptomics. Science *353*, 78–82.

14. Rodriques, S.G., Stickels, R.R., Goeva, A., Martin, C.A., Murray, E., Vanderburg, C.R., Welch, J., Chen, L.M., Chen, F., and Macosko, E.Z. (2019). Slide-seq: A scalable technology for measuring genome-wide expression at high spatial resolution. Science *363*, 1463–1467.

15. Stickels, R.R., Murray, E., Kumar, P., Li, J., Marshall, J.L., Di Bella, D.J., Arlotta, P., Macosko, E.Z., and Chen, F. (2021). Highly sensitive spatial transcriptomics at near-cellular resolution with Slide-seqV2. Nat. Biotechnol. *39*, 313–319.

16. Marx, V. (2021). Publisher Correction: Method of the Year: spatially resolved transcriptomics. Nat. Methods *18*, 219.

17. Waylen, L.N., Nim, H.T., Martelotto, L.G., and Ramialison, M. (2020). From whole-mount to single-cell spatial assessment of gene expression in 3D. Commun Biol *3*, 602.

18. Palla, G., Fischer, D.S., Regev, A., and Theis, F.J. (2022). Spatial components of molecular tissue biology. Nat. Biotechnol. https://doi.org/10.1038/s41587-021-01182-1.

19. Cable, D.M., Murray, E., Zou, L.S., Goeva, A., Macosko, E.Z., Chen, F., and Irizarry, R.A. (2021). Robust decomposition of cell type mixtures in spatial transcriptomics. Nat. Biotechnol., 1–10.

20. Kleshchevnikov, V., Shmatko, A., Dann, E., Aivazidis, A., King, H.W., Li, T., Elmentaite, R., Lomakin, A., Kedlian, V., Gayoso, A., et al. (2022). Cell2location maps fine-grained cell types in spatial transcriptomics. Nat. Biotechnol. *40*, 661–671.

21. Mages, S., Moriel, N., Avraham-Davidi, I., Murray, E., Watter, J., Chen, F., Rozenblatt-Rosen, O., Klughammer, J., Regev, A., and Nitzan, M. (2023). TACCO unifies annotation transfer and decomposition of cell identities for single-cell and spatial omics. Nat. Biotechnol., 1–9.

22. Lopez, R., Li, B., Keren-Shaul, H., Boyeau, P., Kedmi, M., Pilzer, D., Jelinski, A., Yofe, I., David, E., Wagner, A., et al. (2022). DestVI identifies continuums of cell types in spatial transcriptomics data. Nat. Biotechnol. *40*, 1360–1369.

23. Biancalani, T., Scalia, G., Buffoni, L., Avasthi, R., Lu, Z., Sanger, A., Tokcan, N., Vanderburg, C.R., Segerstolpe, Å., Zhang, M., et al. (2021). Deep learning and alignment of spatially resolved single-cell transcriptomes with Tangram. Nat. Methods *18*, 1352–1362.

24. Cancer Genome Atlas Network (2012). Comprehensive molecular characterization of human colon and rectal cancer. Nature *487*, 330–337.

25. Kwong, L.N., and Dove, W.F. (2009). APC and its modifiers in colon cancer. Adv. Exp. Med. Biol. *656*, 85–106.

26. Fearon, E.R. (2011). Molecular genetics of colorectal cancer. Annu. Rev. Pathol. *6*, 479–507.

27. Fearon, E.R., and Vogelstein, B. (1990). A genetic model for colorectal tumorigenesis. Cell *61*, 759–767.

28. Chen, B., Scurrah, C.R., McKinley, E.T., Simmons, A.J., Ramirez-Solano, M.A., Zhu, X., Markham, N.O., Heiser, C.N., Vega, P.N., Rolong, A., et al. (2021). Differential pre-malignant programs and microenvironment chart distinct paths to malignancy in human colorectal polyps. Cell *184*, 6262-6280.e26.

29. Becker, W.R., Nevins, S.A., Chen, D.C., Chiu, R., Horning, A.M., Guha, T.K., Laquindanum, R., Mills, M., Chaib, H., Ladabaum, U., et al. (2022). Single-cell analyses define a continuum of cell state and composition changes in the malignant transformation of polyps to colorectal cancer. Nat. Genet., 1–11.

30. Roper, J., Tammela, T., Cetinbas, N.M., Akkad, A., Roghanian, A., Rickelt, S., Almeqdadi, M., Wu, K., Oberli, M.A., Sánchez-Rivera, F.J., et al. (2017). In vivo genome editing and organoid transplantation models of colorectal cancer and metastasis. Nat. Biotechnol. *35*, 569–576.

31. Roper, J., Tammela, T., Akkad, A., Almeqdadi, M., Santos, S.B., Jacks, T., and Yilmaz, Ö.H. (2018). Colonoscopy-based colorectal cancer modeling in mice with CRISPR–Cas9 genome editing and organoid transplantation. Nat. Protoc. *13*, 217–234.

32. Golovko, D., Kedrin, D., Yilmaz, Ö.H., and Roper, J. (2015). Colorectal cancer models for novel drug discovery. Expert Opin. Drug Discov. *10*, 1217–1229.

33. Gyllborg, D., Langseth, C.M., Qian, X., Choi, E., Salas, S.M., Hilscher, M.M., Lein, E.S., and Nilsson, M. (2020). Hybridization-based in situ sequencing (HybISS) for spatially resolved transcriptomics in human and mouse brain tissue. Nucleic Acids Res. *48*, e112.

34. Hagerling, C., Gonzalez, H., Salari, K., Wang, C.-Y., Lin, C., Robles, I., van Gogh, M., Dejmek, A., Jirström, K., and Werb, Z. (2019). Immune effector monocyte–neutrophil cooperation induced by the primary tumor prevents metastatic progression of breast cancer. Proc. Natl. Acad. Sci. U. S. A. *116*, 21704–21714.

35. Arenberg, D.A., Keane, M.P., DiGiovine, B., Kunkel, S.L., Strom, S.R., Burdick, M.D., Iannettoni, M.D., and Strieter, R.M. (2000). Macrophage infiltration in human non-small-cell lung cancer: the role of CC chemokines. Cancer Immunol. Immunother. *49*, 63–70.

36. Smith, P.M., and Garrett, W.S. (2011). The gut microbiota and mucosal T cells. Front. Microbiol. *2*, 111.

37. La Manno, G., Soldatov, R., Zeisel, A., Braun, E., Hochgerner, H., Petukhov, V., Lidschreiber, K., Kastriti, M.E., Lönnerberg, P., Furlan, A., et al. (2018). RNA velocity of single cells. Nature *560*, 494–498.

38. Ziyad, S., and Iruela-Arispe, M.L. (2011). Molecular mechanisms of tumor angiogenesis. Genes Cancer *2*, 1085–1096.

39. Zeng, Z.-S., Shu, W.-P., Cohen, A.M., and Guillem, J.G. (2002). Matrix metalloproteinase-7 expression in colorectal cancer liver metastases: evidence for involvement of MMP-7 activation in human cancer metastases. Clin. Cancer Res. *8*, 144–148.

40. Li, D., Peng, Z., Tang, H., Wei, P., Kong, X., Yan, D., Huang, F., Li, Q., Le, X., Li, Q., et al. (2011). KLF4-mediated negative regulation of IFITM3 expression plays a critical role in colon cancer pathogenesis. Clin. Cancer Res. *17*, 3558–3568.

41. Kitamura, T., Kometani, K., Hashida, H., Matsunaga, A., Miyoshi, H., Hosogi, H., Aoki, M., Oshima, M., Hattori, M., Takabayashi, A., et al. (2007). SMAD4-deficient intestinal tumors recruit CCR1+ myeloid cells that promote invasion. Nat. Genet. *39*, 467–475.

42. Haber, A.L., Biton, M., Rogel, N., Herbst, R.H., Shekhar, K., Smillie, C., Burgin, G., Delorey, T.M., Howitt, M.R., Katz, Y., et al. (2017). A single-cell survey of the small intestinal epithelium. Nature *551*, 333–339.

43. Biton, M., Haber, A.L., Rogel, N., Burgin, G., Beyaz, S., Schnell, A., Ashenberg, O., Su, C.-W., Smillie, C., Shekhar, K., et al. (2018). T Helper Cell Cytokines Modulate Intestinal Stem Cell Renewal and Differentiation. Cell *175*, 1307-1320.e22.

44. Smillie, C.S., Biton, M., Ordovas-Montanes, J., Sullivan, K.M., Burgin, G., Graham, D.B., Herbst, R.H., Rogel, N., Slyper, M., Waldman, J., et al. (2019). Intra- and Inter-cellular Rewiring of the Human Colon during Ulcerative Colitis. Cell *178*, 714-730.e22.

45. Welch, J.D., Kozareva, V., Ferreira, A., Vanderburg, C., Martin, C., and Macosko, E.Z. (2019). Single-Cell Multi-omic Integration Compares and Contrasts Features of Brain Cell Identity. Cell *177*, 1873-1887.e17.

46. van Neerven, S.M., de Groot, N.E., Nijman, L.E., Scicluna, B.P., van Driel, M.S., Lecca, M.C., Warmerdam, D.O., Kakkar, V., Moreno, L.F., Vieira Braga, F.A., et al. (2021). Apc-mutant cells act as supercompetitors in intestinal tumour initiation. Nature *594*, 436–441.

47. Flanagan, D.J., Pentinmikko, N., Luopajärvi, K., Willis, N.J., Gilroy, K., Raven, A.P., Mcgarry, L., Englund, J.I., Webb, A.T., Scharaw, S., et al. (2021). NOTUM from Apc-mutant cells biases clonal competition to initiate cancer. Nature *594*, 430–435.

48. Clevers, H. (2006). Wnt/beta-catenin signaling in development and disease. Cell *127*, 469–480.

49. Folkman, J. (2002). Role of angiogenesis in tumor growth and metastasis. Semin. Oncol. *29*, 15–18.

50. Lasry, A., Zinger, A., and Ben-Neriah, Y. (2016). Inflammatory networks underlying colorectal cancer. Nat. Immunol. *17*, 230–240.

51. Fleming, M., Ravula, S., Tatishchev, S.F., and Wang, H.L. (2012). Colorectal carcinoma: Pathologic aspects. J. Gastrointest. Oncol. *3*, 153–173.

52. Winkler, J., Abisoye-Ogunniyan, A., Metcalf, K.J., and Werb, Z. (2020). Concepts of extracellular matrix remodelling in tumour progression and metastasis. Nat. Commun. *11*, 1–19.

53. Drev, D., Harpain, F., Beer, A., Stift, A., Gruber, E.S., Klimpfinger, M., Thalhammer, S., Reti, A., Kenner, L., Bergmann, M., et al. (2019). Impact of Fibroblast-Derived SPARC on Invasiveness of Colorectal Cancer Cells. Cancers *11*. https://doi.org/10.3390/cancers11101421.

54. Burden, R.E., Gormley, J.A., Jaquin, T.J., Small, D.M., Quinn, D.J., Hegarty, S.M., Ward, C., Walker, B., Johnston, J.A., Olwill, S.A., et al. (2009). Antibody-mediated inhibition of cathepsin S blocks colorectal tumor invasion and angiogenesis. Clin. Cancer Res. *15*, 6042–6051.

55. Basu, S., Cheriyamundath, S., Gavert, N., Brabletz, T., Haase, G., and Ben-Ze’ev, A. (2019). Increased expression of cathepsin D is required for L1-mediated colon cancer progression. Oncotarget *10*, 5217–5228.

56. Spencer, J., and Sollid, L.M. (2016). The human intestinal B-cell response. Mucosal Immunol. *9*, 1113–1124.

57. Sautès-Fridman, C., Petitprez, F., Calderaro, J., and Fridman, W.H. (2019). Tertiary lymphoid structures in the era of cancer immunotherapy. Nat. Rev. Cancer *19*, 307–325.

58. Mendez, M.G., Kojima, S.-I., and Goldman, R.D. (2010). Vimentin induces changes in cell shape, motility, and adhesion during the epithelial to mesenchymal transition. FASEB J. *24*, 1838–1851.

59. Lu, M.-H., Huang, C.-C., Pan, M.-R., Chen, H.-H., and Hung, W.-C. (2012). Prospero homeobox 1 promotes epithelial-mesenchymal transition in colon cancer cells by inhibiting E-cadherin via miR-9. Clin. Cancer Res. *18*, 6416–6425.

60. Oliemuller, E., Newman, R., Tsang, S.M., Foo, S., Muirhead, G., Noor, F., Haider, S., Aurrekoetxea-Rodríguez, I., Vivanco, M. dM, and Howard, B.A. (2020). SOX11 promotes epithelial/mesenchymal hybrid state and alters tropism of invasive breast cancer cells. Elife *9*, e58374.

61. Marjanovic, N.D., Hofree, M., Chan, J.E., Canner, D., Wu, K., Trakala, M., Hartmann, G.G., Smith, O.C., Kim, J.Y., Evans, K.V., et al. (2020). Emergence of a High-Plasticity Cell State during Lung Cancer Evolution. Cancer Cell *38*, 229-246.e13.

62. Puram, S.V., Tirosh, I., Parikh, A.S., Patel, A.P., Yizhak, K., Gillespie, S., Rodman, C., Luo, C.L., Mroz, E.A., Emerick, K.S., et al. (2017). Single-Cell Transcriptomic Analysis of Primary and Metastatic Tumor Ecosystems in Head and Neck Cancer. Cell *171*, 1611-1624.e24.

63. Schwab, R.H.M., Amin, N., Flanagan, D.J., Johanson, T.M., Phesse, T.J., and Vincan, E. (2018). Wnt is necessary for mesenchymal to epithelial transition in colorectal cancer cells. Dev. Dyn. *247*, 521–530.

64. DiMeo, T.A., Anderson, K., Phadke, P., Fan, C., Perou, C.M., Naber, S., and Kuperwasser, C. (2009). A novel lung metastasis signature links Wnt signaling with cancer cell self-renewal and epithelial-mesenchymal transition in basal-like breast cancer. Cancer Res. *69*, 5364–5373.

65. Penninger, J.M., and Crabtree, G.R. (1999). The Actin Cytoskeleton and Lymphocyte Activation. Cell *96*, 9–12.

66. Cang, Z., Zhao, Y., Almet, A.A., Stabell, A., Ramos, R., Plikus, M.V., Atwood, S.X., and Nie, Q. (2023). Screening cell–cell communication in spatial transcriptomics via collective optimal transport. Nat. Methods *20*, 218–228.

67. Che, L.-H., Liu, J.-W., Huo, J.-P., Luo, R., Xu, R.-M., He, C., Li, Y.-Q., Zhou, A.-J., Huang, P., Chen, Y.-Y., et al. (2021). A single-cell atlas of liver metastases of colorectal cancer reveals reprogramming of the tumor microenvironment in response to preoperative chemotherapy. Cell Discovery *7*, 1–21.

68. Zheng, X., Song, J., Yu, C., Zhou, Z., Liu, X., Yu, J., Xu, G., Yang, J., He, X., Bai, X., et al. (2022). Single-cell transcriptomic profiling unravels the adenoma-initiation role of protein tyrosine kinases during colorectal tumorigenesis. Signal Transduction and Targeted Therapy *7*, 1–14.

69. Khaliq, A.M., Erdogan, C., Kurt, Z., Turgut, S.S., Grunvald, M.W., Rand, T., Khare, S., Borgia, J.A., Hayden, D.M., Pappas, S.G., et al. (2022). Correction: Refining colorectal cancer classification and clinical stratification through a single-cell atlas. Genome Biol. *23*, 156.

70. Joanito, I., Wirapati, P., Zhao, N., Nawaz, Z., Yeo, G., Lee, F., Eng, C.L.P., Macalinao, D.C., Kahraman, M., Srinivasan, H., et al. (2022). Single-cell and bulk transcriptome sequencing identifies two epithelial tumor cell states and refines the consensus molecular classification of colorectal cancer. Nat. Genet. *54*, 963–975.

71. Guinney, J., Dienstmann, R., Wang, X., de Reyniès, A., Schlicker, A., Soneson, C., Marisa, L., Roepman, P., Nyamundanda, G., Angelino, P., et al. (2015). The consensus molecular subtypes of colorectal cancer. Nat. Med. *21*, 1350–1356.

72. West, N.R., Hegazy, A.N., Owens, B.M.J., Bullers, S.J., Linggi, B., Buonocore, S., Coccia, M., Görtz, D., This, S., Stockenhuber, K., et al. (2017). Oncostatin M drives intestinal

inflammation and predicts response to tumor necrosis factor-neutralizing therapy in patients with inflammatory bowel disease. Nat. Med. *23*, 579–589.

73. West, N.R., Murray, J.I., and Watson, P.H. (2013). Oncostatin-M promotes phenotypic changes associated with mesenchymal and stem cell-like differentiation in breast cancer. Oncogene *33*, 1485–1494.

74. Smigiel, J.M., Parameswaran, N., and Jackson, M.W. (2017). Potent EMT and CSC phenotypes are induced by oncostatin-M in pancreatic cancer. Mol. Cancer Res. *15*, 478–488.

75. Hara, T., Chanoch-Myers, R., Mathewson, N.D., Myskiw, C., Atta, L., Bussema, L., Eichhorn, S.W., Greenwald, A.C., Kinker, G.S., Rodman, C., et al. (2021). Interactions between cancer cells and immune cells drive transitions to mesenchymal-like states in glioblastoma. Cancer Cell *39*, 779-792.e11.

76. de Sousa e Melo, F., Kurtova, A.V., Harnoss, J.M., Kljavin, N., Hoeck, J.D., Hung, J., Anderson, J.E., Storm, E.E., Modrusan, Z., Koeppen, H., et al. (2017). A distinct role for Lgr5+ stem cells in primary and metastatic colon cancer. Nature *543*, 676–680.

77. Schepers, A.G., Snippert, H.J., Stange, D.E., van den Born, M., van Es, J.H., van de Wetering, M., and Clevers, H. (2012). Lineage tracing reveals Lgr5+ stem cell activity in mouse intestinal adenomas. Science *337*, 730–735.

78. André, T., Shiu, K.-K., Kim, T.W., Jensen, B.V., Jensen, L.H., Punt, C., Smith, D., Garcia-Carbonero, R., Benavides, M., Gibbs, P., et al. (2020). Pembrolizumab in Microsatellite-Instability–High Advanced Colorectal Cancer. N. Engl. J. Med. *383*, 2207–2218.

79. Kuraguchi, M., Wang, X.-P., Bronson, R.T., Rothenberg, R., Ohene-Baah, N.Y., Lund, J.J., Kucherlapati, M., Maas, R.L., and Kucherlapati, R. (2006). Adenomatous polyposis coli (APC) is required for normal development of skin and thymus. PLoS Genet. *2*, e146.

80. Johnson, L., Mercer, K., Greenbaum, D., Bronson, R.T., Crowley, D., Tuveson, D.A., and Jacks, T. (2001). Somatic activation of the K-ras oncogene causes early onset lung cancer in mice. Nature *410*, 1111–1116.

81. Madisen, L., Zwingman, T.A., Sunkin, S.M., Oh, S.W., Zariwala, H.A., Gu, H., Ng, L.L., Palmiter, R.D., Hawrylycz, M.J., Jones, A.R., et al. (2009). A robust and high-throughput Cre reporting and characterization system for the whole mouse brain. Nat. Neurosci. *13*, 133–140.

82. Marino, S., Vooijs, M., van Der Gulden, H., Jonkers, J., and Berns, A. (2000). Induction of medulloblastomas in p53-null mutant mice by somatic inactivation of Rb in the external granular layer cells of the cerebellum. Genes Dev. *14*, 994–1004.

83. el Marjou, F., Janssen, K.-P., Chang, B.H.-J., Li, M., Hindie, V., Chan, L., Louvard, D., Chambon, P., Metzger, D., and Robine, S. (2004). Tissue-specific and inducible Cre-mediated recombination in the gut epithelium. Genesis *39*, 186–193.

84. Stoeckius, M., Zheng, S., Houck-Loomis, B., Hao, S., Yeung, B.Z., Mauck, W.M., 3rd, Smibert, P., and Satija, R. (2018). Cell Hashing with barcoded antibodies enables multiplexing and doublet detection for single cell genomics. Genome Biol. *19*, 224.

85. Qian, X., Harris, K.D., Hauling, T., Nicoloutsopoulos, D., Muñoz-Manchado, A.B., Skene, N., Hjerling-Leffler, J., and Nilsson, M. (2019). Probabilistic cell typing enables fine mapping of closely related cell types in situ. Nat. Methods *17*, 101–106.

86. Li, B., Gould, J., Yang, Y., Sarkizova, S., Tabaka, M., Ashenberg, O., Rosen, Y., Slyper, M., Kowalczyk, M.S., Villani, A.-C., et al. (2020). Cumulus provides cloud-based data analysis for large-scale single-cell and single-nucleus RNA-seq. Nat. Methods *17*, 793–798.

87. Wolf, F.A., Angerer, P., and Theis, F.J. (2018). SCANPY: large-scale single-cell gene expression data analysis. Genome Biol. *19*, 15.

88. Wolock, S.L., Lopez, R., and Klein, A.M. (2019). Scrublet: Computational Identification of Cell Doublets in Single-Cell Transcriptomic Data. Cell Syst *8*, 281-291.e9.

89. Aran, D., Looney, A.P., Liu, L., Wu, E., Fong, V., Hsu, A., Chak, S., Naikawadi, R.P., Wolters, P.J., Abate, A.R., et al. (2019). Reference-based analysis of lung single-cell sequencing reveals a transitional profibrotic macrophage. Nat. Immunol. *20*, 163–172.

90. Tabula Muris Consortium, Overall coordination, Logistical coordination, Organ collection and processing, Library preparation and sequencing, Computational data analysis, Cell type annotation, Writing group, Supplemental text writing group, and Principal investigators (2018). Single-cell transcriptomics of 20 mouse organs creates a Tabula Muris. Nature *562*, 367–372.

91. Pedregosa, F., Varoquaux, G., Gramfort, A., and Michel, V. Scikit-learn: Machine Learning in Python. 12 (85): 2825–2830. : http://jmlr. org/papers/v12 ….

92. Polański, K., Young, M.D., Miao, Z., Meyer, K.B., Teichmann, S.A., and Park, J.-E. (2020). BBKNN: fast batch alignment of single cell transcriptomes. Bioinformatics *36*, 964–965.

93. Rao, J.N., and Wang, J.-Y. (2010). Intestinal Architecture and Development (Morgan & Claypool Life Sciences).

94. Puram, S.V., Parikh, A.S., and Tirosh, I. (2018). Single cell RNA-seq highlights a role for a partial EMT in head and neck cancer. Mol Cell Oncol *5*, e1448244.

95. Liu, J., Lichtenberg, T., Hoadley, K.A., Poisson, L.M., Lazar, A.J., Cherniack, A.D., Kovatich, A.J., Benz, C.C., Levine, D.A., Lee, A.V., et al. (2018). An Integrated TCGA Pan-Cancer Clinical Data Resource to Drive High-Quality Survival Outcome Analytics. Cell *173*, 400-416.e11.

96. Davidson-Pilon, C. (2019). lifelines: survival analysis in Python. The Journal of Open Source Software *4*, 1317.

97. Fazilaty, H., Brügger, M.D., Valenta, T., Szczerba, B.M., Berkova, L., Doumpas, N., Hausmann, G., Scharl, M., and Basler, K. (2021). Tracing colonic embryonic transcriptional profiles and their reactivation upon intestinal damage. Cell Rep. *36*, 109484.

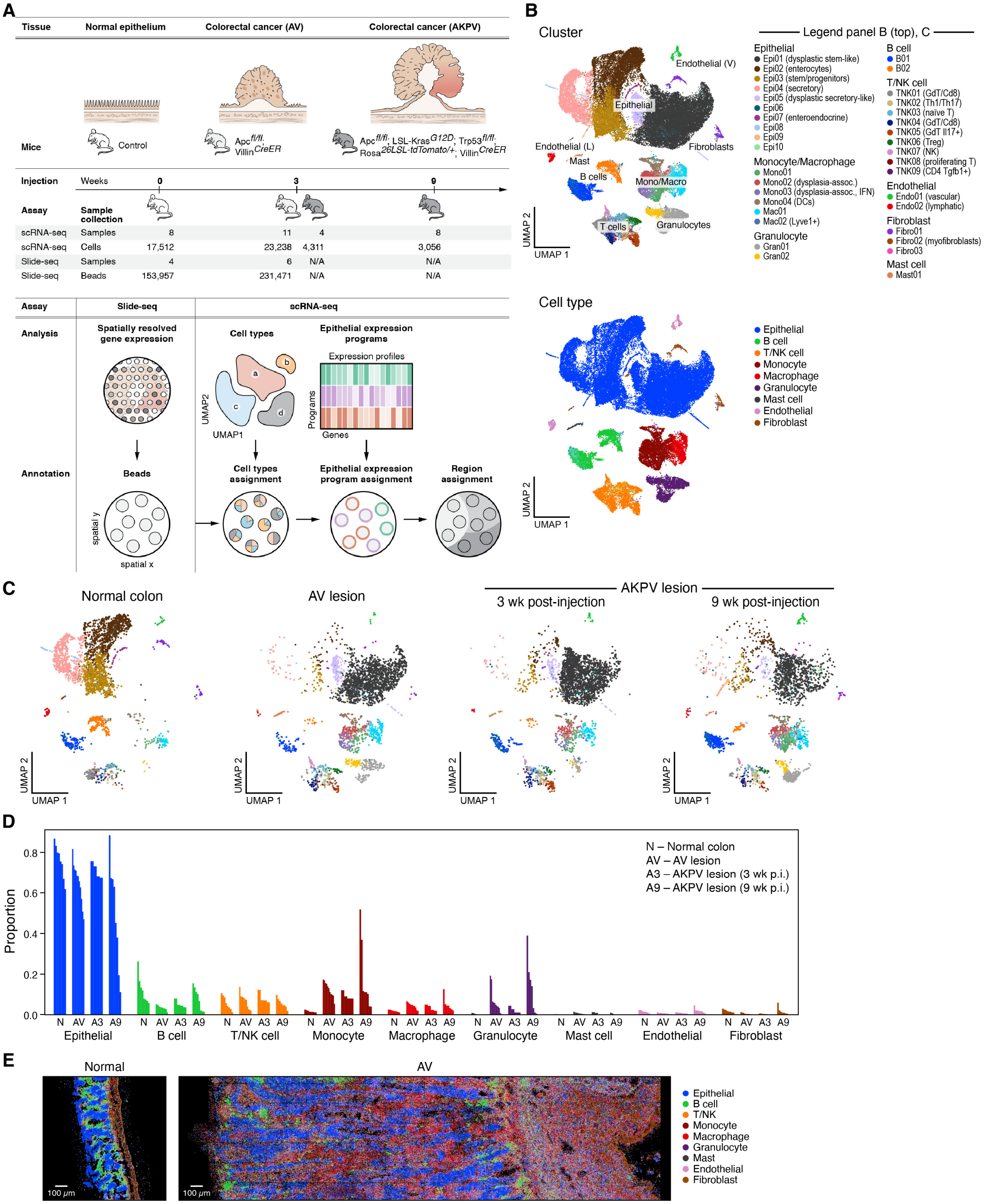
A
Tissue
Normal epithelium
Colorectal cancer (AV)
Colorectal cancer (AKPV)
Mice
Control
Apc fl/fl; Villin CreER
Apc fl/fl; LSL-Kras G12D; Trp53 fl/fl; Rosa26 LSL-tdTomato/+; Villin CreER
Injection
Weeks
0
3
9
Assay
Sample collection
scRNA-seq Samples 8 11 4 8
scRNA-seq Cells 17,512 23,238 4,311 3,056
Slide-seq Samples 4 6 N/A N/A
Slide-seq Beads 153,957 231,471 N/A N/A
Assay
Slide-seq
scRNA-seq
Analysis
Spatially resolved gene expression
Cell types
Epithelial expression programs
Expression profiles
UMAP2
UMAP1
Programs
Genes
a
b
c
d
Annotation
Beads
Cell types assignment
Epithelial expression program assignment
Region assignment
spatial y
spatial x
B
Cluster
Endothelial (V)
Epithelial
Endothelial (L)
Fibroblasts
Mast
B cells
Mono/Macro
T cells
Granulocytes
UMAP 2
UMAP 1
Legend panel B (top), C
Epithelial
Epi01 (dysplastic stem-like)
Epi02 (enterocytes)
Epi03 (stem/progenitors)
Epi04 (secretory)
Epi05 (dysplastic secretory-like)
Epi06
Epi07 (enteroendocrine)
Epi08
Epi09
Epi10
Monocyte/Macrophage
Mono01
Mono02 (dysplasia-assoc.)
Mono03 (dysplasia-assoc., IFN)
Mono04 (DCs)
Mac01
Mac02 (Lyve1+)
Granulocyte
Gran01
Gran02
B cell
B01
B02
T/NK cell
TNK01 (GdT/Cd8)
TNK02 (Th1/Th17)
TNK03 (naive T)
TNK04 (GdT/Cd8)
TNK05 (GdT Il17+)
TNK06 (Treg)
TNK07 (NK)
TNK08 (proliferating T)
TNK09 (CD4 Tgfb1+)
Endothelial
Endo01 (vascular)
Endo02 (lymphatic)
Fibroblast
Fibro01
Fibro02 (myofibroblasts)
Fibro03
Mast cell
Mast01
Cell type
Epithelial
B cell
T/NK cell
Monocyte
Macrophage
Granulocyte
Mast cell
Endothelial
Fibroblast
UMAP 2
UMAP 1
C
Normal colon
AV lesion
AKPV lesion
3 wk post-injection
9 wk post-injection
UMAP 2
UMAP 1
D
Proportion
0.0
0.2
0.4
0.6
0.8
N – Normal colon
AV – AV lesion
A3 – AKPV lesion (3 wk p.i.)
A9 – AKPV lesion (9 wk p.i.)
N AV A3 A9
Epithelial
B cell
T/NK cell
Monocyte
Macrophage
Granulocyte
Mast cell
Endothelial
Fibroblast
E
Normal
AV
100 μm
100 μm
Epithelial
B cell
T/NK
Monocyte
Macrophage
Granulocyte
Mast
Endothelial
Fibroblast

Figure 1. A single cell atlas of healthy colon and dysplastic lesions in mouse.

A. Study overview. **B.** Major cell subsets of healthy colon and dysplastic lesions. 2D embedding of 48,115 single cell profiles colored by cluster (top, legend) or annotated cell type (bottom, legend). **C,D.** Changes in cell composition in dysplastic tissues. C. 2D embedding of single cell profiles, showing only the cells in each condition state, subsampled to equal numbers of cells per condition state, colored by cluster (same legend as in B (top)). D. Proportion of cells (y axis) of each cell type in each sample (x axis). **E.** multiplex RNA *in situ* analysis. Representative images of Cartana analysis of normal colon (left) and AV lesions (right) colored by cell type assignment (same as **Supplementary item 2A**).

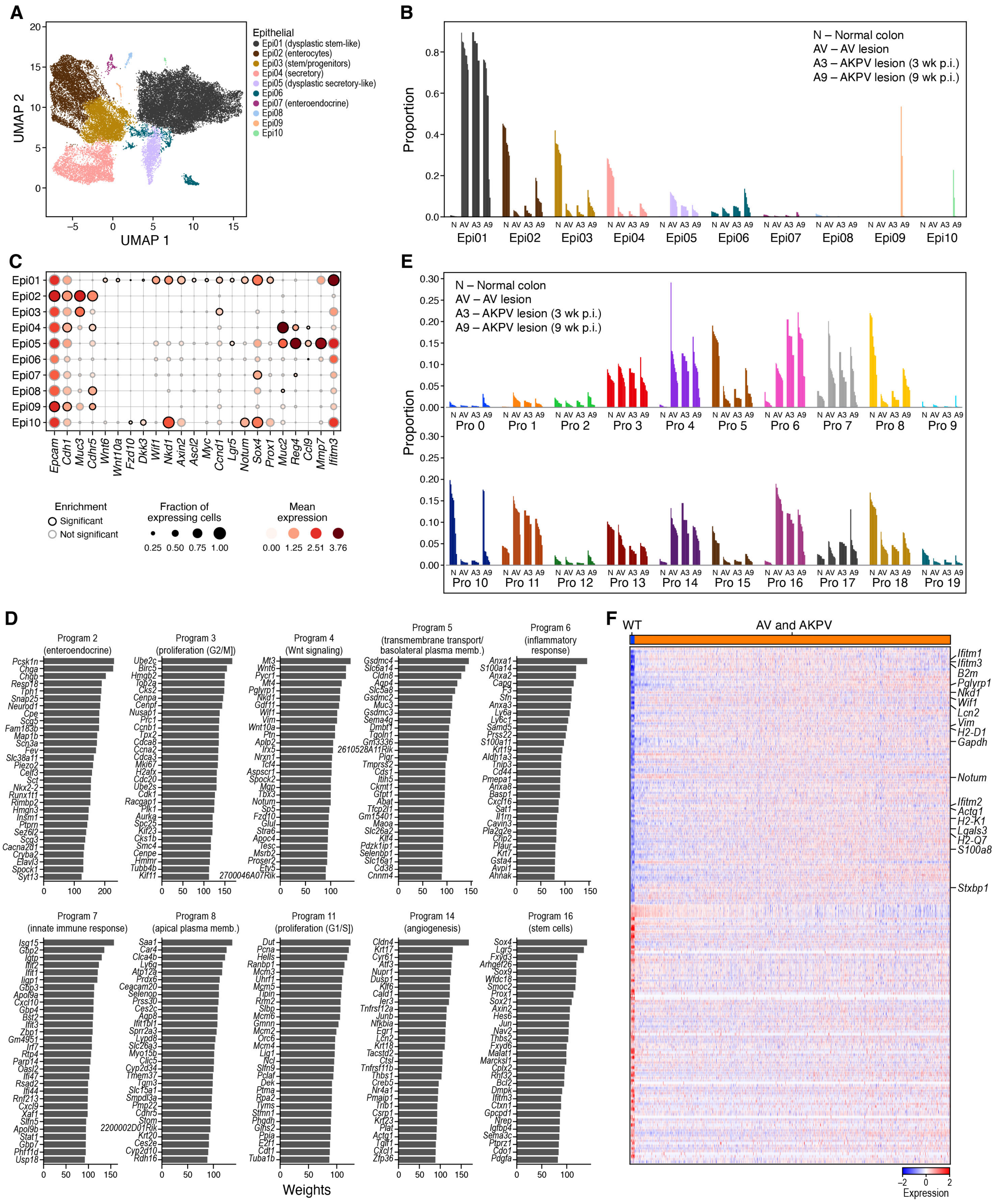
A
UMAP 1
UMAP 2
Epithelial
Epi01 (dysplastic stem-like)
Epi02 (enterocytes)
Epi03 (stem/progenitors)
Epi04 (secretory)
Epi05 (dysplastic secretory-like)
Epi06
Epi07 (enteroendocrine)
Epi08
Epi09
Epi10
B
Proportion
N – Normal colon
AV – AV lesion
A3 – AKPV lesion (3 wk p.i.)
A9 – AKPV lesion (9 wk p.i.)
N AV A3 A9
Epi01 Epi02 Epi03 Epi04 Epi05 Epi06 Epi07 Epi08 Epi09 Epi10
C
Epcam Cdh1 Muc3 Cdhr5 Wnt6 Wnt10a Fzd10 Dkk3 Wif1 Nkd1 Axin2 Ascl2 Myc Ccnd1 Lgr5 Notum Sox4 Prox1 Muc2 Reg4 Ccl9 Mmp7 Ifitm3
Enrichment
Significant
Not significant
Fraction of expressing cells
0.25 0.50 0.75 1.00
Mean expression
0.00 1.25 2.51 3.76
E
Proportion
Pro 0 Pro 1 Pro 2 Pro 3 Pro 4 Pro 5 Pro 6 Pro 7 Pro 8 Pro 9
Pro 10 Pro 11 Pro 12 Pro 13 Pro 14 Pro 15 Pro 16 Pro 17 Pro 18 Pro 19
D
Program 2 (enteroendocrine)
Pcsk1n Chga Chgb Resp18 Tph1 Snap25 Neurod1 Cpe Scg5 Fam183b Map1b Scn3a Fev Slc38a11 Piezo2 Celf3 Sct Nkx2-2 Runx1t1 Rimbp2 Hmgn3 Insm1 Ptprn Sez6l2 Scg3 Cacna2d1 Cryba2 Elavl3 Spock1 Syt13
Program 3 (proliferation (G2/M])
Ube2c Birc5 Hmgb2 Top2a Cks2 Cenpa Cenpf Nusap1 Prc1 Ccnb1 Tpx2 Cdca8 Ccna2 Cdca3 Mki67 H2afx Cdc20 Ube2s Cdk1 Racgap1 Plk1 Aurka Spc25 Kif23 Cks1b Smc4 Cenpe Hmmr Tubb4b Kif11
Program 4 (Wnt signaling)
Mt3 Wnt6 Pycr1 Mt4 Pglyrp1 Nkd1 Gdf11 Wif1 Vim Wnt10a Ptn Aplp2 Irx5 Nrxn1 Tcf4 Aspscr1 Spock2 Mgp Tbx3 Notum Sp5 Fzd10 Glul Stra6 Apoc4 Tesc Msrb2 Proser2 Etv5 2700046A07Rik
Program 5 (transmembrane transport/ basolateral plasma memb.)
Gsdmc4 Slc6a14 Cldn8 Aqp4 Slc5a8 Gsdmc2 Muc3 Gsdmc3 Sema4g Dmbt1 Tgoln1 Gm3336 2610528A11Rik Pigr Tmprss2 Cds1 Itih5 Ckmt1 Gfpt1 Abat Tfcp2l1 Gm15401 Maoa Slc26a2 Klf4 Pdzk1ip1 Selenbp1 Slc16a1 Cd38 Cnnm4
Program 6 (inflammatory response)
Anxa1 S100a14 Anxa2 Capg F3 Sfn Anxa3 Ly6a Ly6c1 Samd5 Prss22 S100a11 Krt19 Aldh1a3 Tnip3 Cd44 Pmepa1 Anxa8 Basp1 Cxcl16 Sat1 Il1rn Cavin3 Pla2g2e Crip2 Plaur Krt7 Gsta4 Avpi1 Ahnak
Program 7 (innate immune response)
Isg15 Gbp2 Igtp Ifit2 Ifit1 Iigp1 Gbp3 Apol9a Cxcl10 Gbp4 Bst2 Ifit3 Zbp1 Gm4951 Irf7 Rtp4 Parp14 Oasl2 Ifi47 Rsad2 Ifi44 Rnf213 Cxcl9 Xaf1 Slfn5 Apol9b Stat1 Gbp7 Phf11d Usp18
Program 8 (apical plasma memb.)
Saa1 Car4 Clca4b Ly6g Atp12a Prdx6 Ceacam20 Selenop Prss30 Ces2c Aqp8 Ifit1bl1 Sprr2a3 Lypd8 Slc26a3 Myo15b Clic5 Cyp2d34 Tmem37 Tgm3 Slc5a1 Smpdl3a Pmp22 Cdhr5 Stom 2200002D01Rik Krt20 Ces2e Cyp2d10 Rdh16
Program 11 (proliferation (G1/S])
Dut Pcna Hells Ranbp1 Mcm3 Uhrf1 Mcm5 Tipin Rrm2 Slbp Mcm6 Gmnn Mcm2 Orc6 Mcm4 Lig1 Ncl Slfn9 Pclaf Dek Ptma Rpa2 Tyms Stmn1 Phgdh Gins2 Ppia E2f1 Cdt1 Tuba1b
Program 14 (angiogenesis)
Cldn4 Krt17 Cyr61 Atf3 Nupr1 Dusp1 Klf6 Cald1 Ier3 Tnfrsf12a Junb Nfkbia Egr1 Lcn2 Krt18 Tacstd2 Ctsl Tnfrsf11b Thbs1 Creb5 Nr4a1 Pmaip1 Trib1 Csrp1 Krt23 Plat Actg1 Tgif1 Cxcl1 Zfp36
Program 16 (stem cells)
Sox4 Lgr5 Fxyd3 Arhgef26 Sox9 Wfdc18 Smoc2 Prox1 Sox21 Axin2 Hes6 Jun Nav2 Thbs2 Fxyd6 Malat1 Marcksl1 Cplx2 Rnf32 Bcl2 Dmpk Ifitm3 Ctxn1 Gpcpd1 Nrep Igfbp4 Sema3c Ptprz1 Cdo1 Pdgfa
Weights
F
WT
AV and AKPV
Ifitm1 Ifitm3 B2m Pglyrp1 Nkd1 Wif1 Lcn2 Vim H2-D1 Gapdh Notum Ifitm2 Actg1 H2-K1 Lgals3 H2-Q7 S100a8 Stxbp1
Expression

Figure 2. Composition and cell intrinsic expression program changes in dysplastic epithelial cells.

A-C. Compositional changes in epithelial cells in dysplastic tissue. A. 2D embedding of epithelial cell profiles colored by clusters (legend). Cluster Epi06: potential doublets (**Methods**). B. Proportion of cells out of all epithelial cells (y axis) of each epithelial cell subset in each sample (x axis). C. Fraction of expressing cells (dot size) and mean expression in expressing cells (dot color) of marker genes (columns) for each cluster (rows). **D-E.** Use of epithelial cell programs changes in dysplastic tissue. D. Weights (x axis) of each of the 20 top ranked genes (y axis) for each program. E. Proportion of program weights summed over all epithelial cells (y axis) in each sample (x axis). **F.** Stem cell program 16 is induced in epithelial cells in dysplastic tissue. Scaled log-normalized expression (color bar) of the top 100 genes differentially expressed between cells from normal colon and from dysplastic (AV and AKPV) across the 10,812 cells that accounted for 90% of program 16's expression across all epithelial cells (columns). Selected program genes are marked.

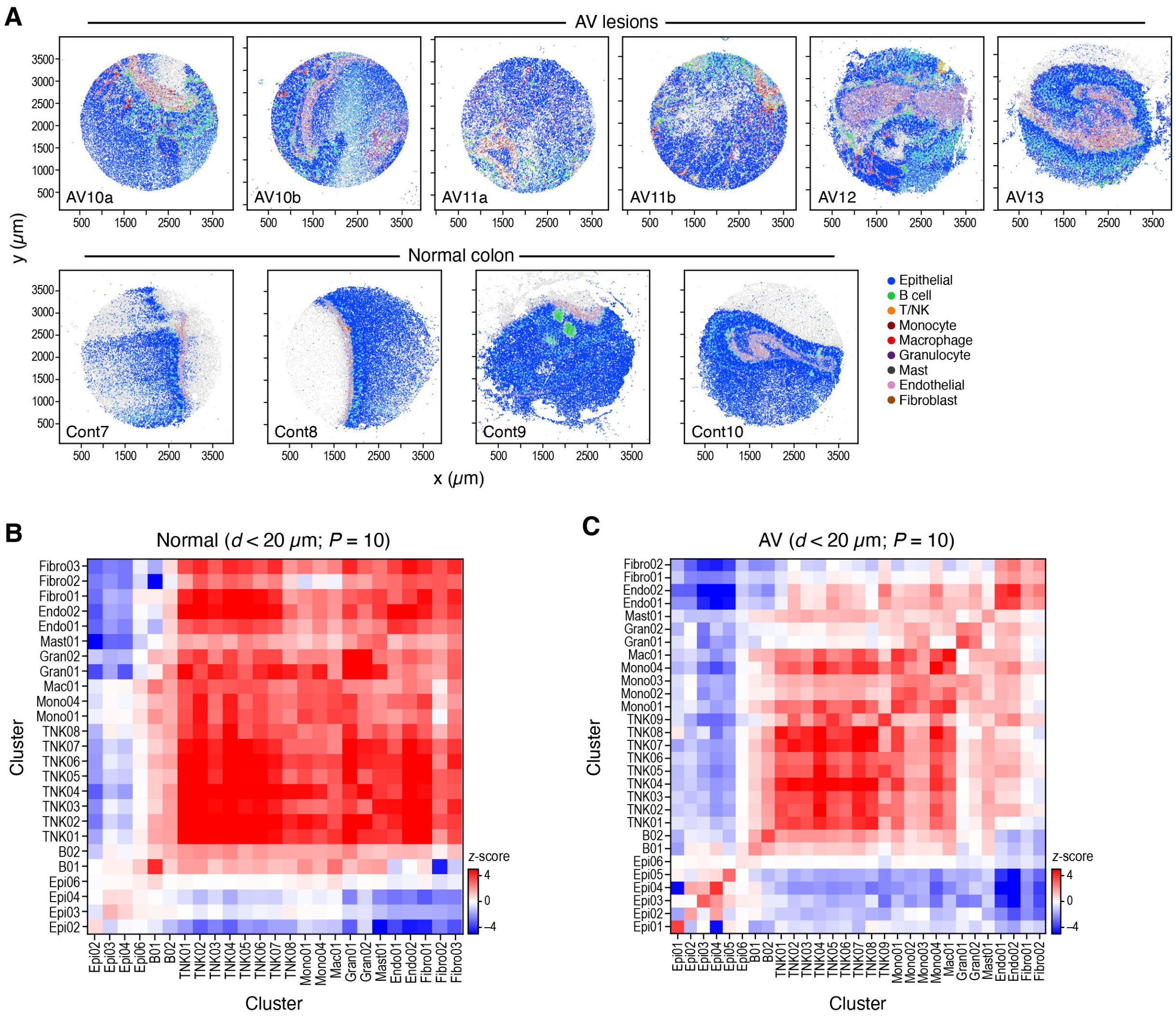

Figure 3. Altered cell type neighborship in CRC.

A. Cell type distributions *in situ*. Slide-seq pucks of dysplastic (top) and normal (bottom) tissue colored by TACCO assignment of cell labels (legend, light grey: low quality beads) (x and y axis: spatial coordinates in μm). **B,C.** Cell type neighborships in normal and dysplastic colon tissue. Short-range (up to 20μm) neighborship enrichment (Z score, color bar) vs. a background of spatially random annotation assignments for each pair of cell annotations (rows, columns) in normal (A) and dysplastic (B) tissue.

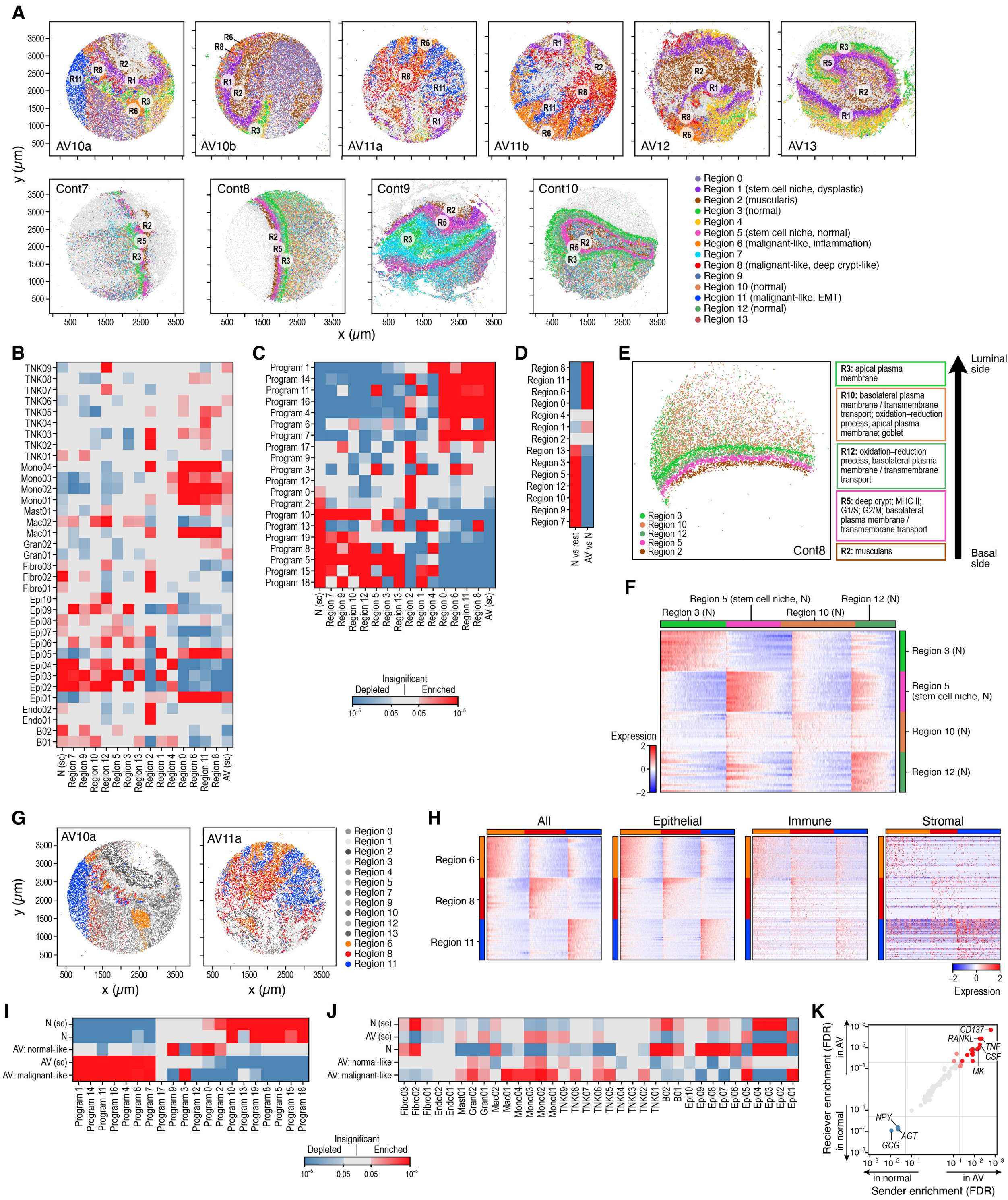
A
AV10a
AV10b
AV11a
AV11b
AV12
AV13
Cont7
Cont8
Cont9
Cont10
y (µm)
x (µm)
Region 0
Region 1 (stem cell niche, dysplastic)
Region 2 (muscularis)
Region 3 (normal)
Region 4
Region 5 (stem cell niche, normal)
Region 6 (malignant-like, inflammation)
Region 7
Region 8 (malignant-like, deep crypt-like)
Region 9
Region 10 (normal)
Region 11 (malignant-like, EMT)
Region 12 (normal)
Region 13
B
C
D
N vs rest
AV vs N
E
Cont8
R3: apical plasma membrane
R10: basolateral plasma membrane / transmembrane transport; oxidation-reduction process; apical plasma membrane; goblet
R12: oxidation-reduction process; basolateral plasma membrane / transmembrane transport
R5: deep crypt; MHC II; G1/S; G2/M; basolateral plasma membrane / transmembrane transport
R2: muscularis
Luminal side
Basal side
Insignificant
Depleted
Enriched
F
Region 3 (N)
Region 5 (stem cell niche, N)
Region 10 (N)
Region 12 (N)
Expression
G
H
All
Epithelial
Immune
Stromal
Region 6
Region 8
Region 11
I
N (sc)
N
AV: normal-like
AV (sc)
AV: malignant-like
J
K
CD137
RANKL
TNF
CSF
MK
NPY
AGT
GCG
Reciever enrichment (FDR)
in AV
in normal
Sender enrichment (FDR)

Figure 4. **Three cellular neighborhoods associated with tumor progression.**

A. Spatial regions. Slide-seq pucks of AV (top) and normal (bottom) mouse colon colored by TACCO regions (legend, light gray: low quality beads) (x and y axis are spatial coordinates in μm). **B,C.** Enrichment and depletion of cell subsets and epithelial programs across different regions. Significance (FDR, color bar, two-sided Welch's t-test on CLR-transformed compositions) of enrichment (red) or depletion (blue) of specific cell subsets (rows, B) or epithelial cell programs (rows, C) in the different regions defined by TACCO (columns) as well as all normal ("N (ref.)", leftmost column) and AV ("AV (ref.)", leftmost column) samples. **D.** TACCO defined regions preferentially relate to normal or AV tissue. Significance (FDR, color bar, two-sided Welch's t-test on CLR-transformed compositions) of enrichment (red) or depletion (blue) of each TACCO defined region (rows) in normal ("N vs. rest") and AV ("AV vs. N") samples (columns). **E.** TACCO reveals normal colon architecture. Left: Slide-seq puck of normal mouse colon colored by TACCO region annotations (legend) (x and y axis: spatial coordinates (μm)). Right: Main epithelial expression programs enriched in each region (FDR<6.3 10^{-4}, two-sided Welch's t test on CLR-transformed compositions) except region 2 (muscularis), which is characterized by non-epithelial (stromal) cell types. **F.** Expression signatures of cells in normal regions 3,5,10 and 12. Scaled log-normalized expression of the top 20 differentially expressed genes (rows) for each bead (columns) in the region. **G,H**. Malignant-like regions. G. Slide-seq pucks of two AV lesions colored by TACCO annotations of malignant-like regions 6, 8 and 11. H. Scaled log-normalized expression of the top 20 differentially expressed genes (rows) of each bead (left, columns) in the region; or epithelial (middle left), immune (middle right) or stromal (right) fractions of beads (columns) in regions 6, 8 and 11 in dysplastic lesions. **I,J.** Epithelial cell subsets and programs associated with "malignant-like", "normal-like" and normal tissues. Significance (FDR, color bar, two-sided Welch's t-test on CLR-transformed compositions) of enrichment (red) or depletion (blue) of epithelial cell programs (I, rows) or epithelial, immune and stromal cell subsets (J, rows) in different tissue types (columns) based on Slide-seq or scRNA-seq ("sc") samples. **K.** Inferred interaction pathways. Enrichment (FDR) in AV *vs*. normal tissue of corresponding "sender" (x axis) and "receiver" (y axis) (aggregated over ligand-receptor pairs) pathways (dots). Red/blue: pathways significantly enriched in AV/normal samples and (light red: only for either sender or receiver). The top 5 enriched pathways (in each direction) are labeled.

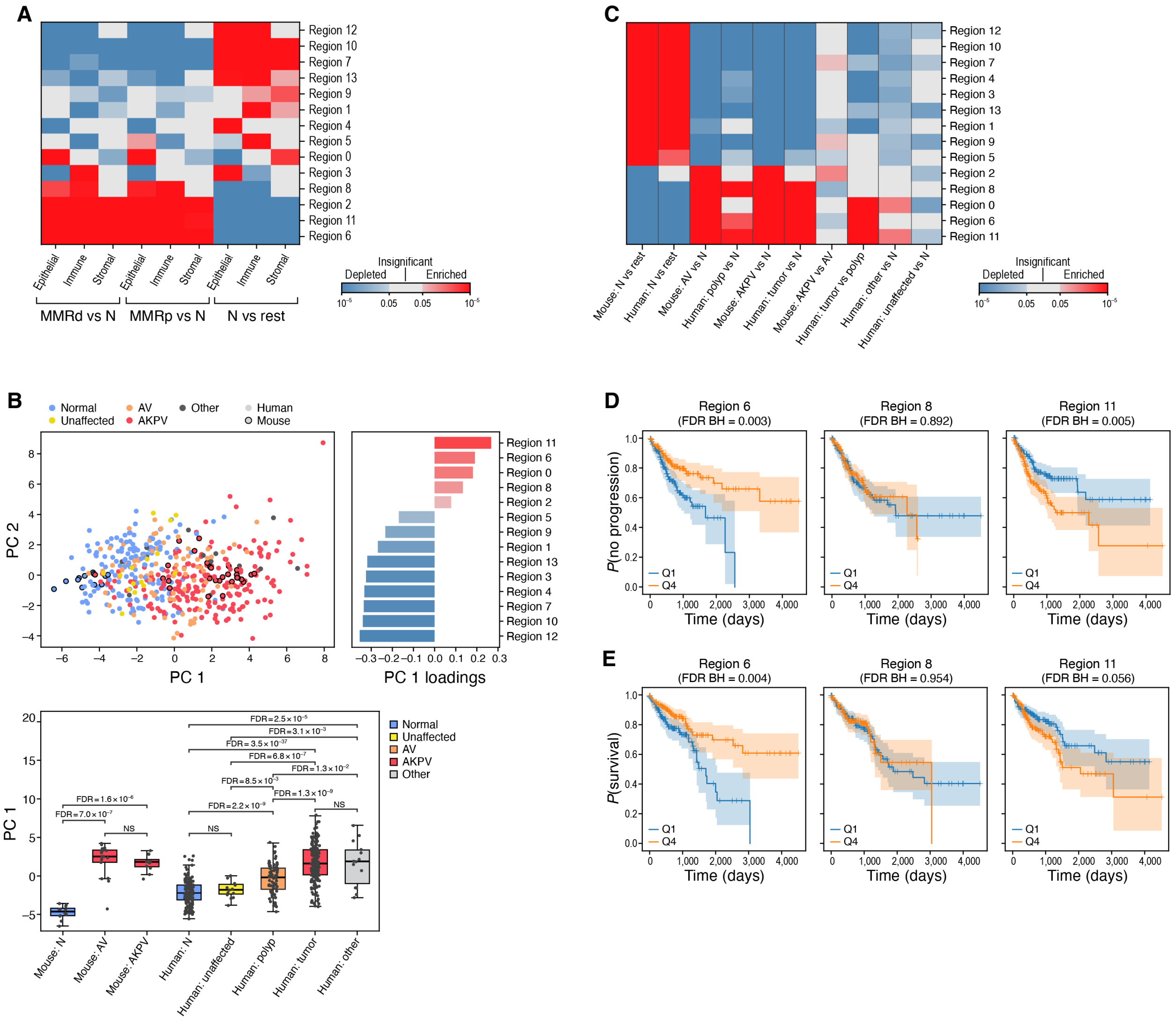

Figure 5. Mouse tumor regions associated with tumor progression in human colorectal tumors.

A. Expression profiles characterizing mouse regions are recapitulated in human tumors. Significance (FDR, color bar, two-sided Welch's t-test on CLR-transformed compositions) of enrichment (red) or depletion (blue) of region-associated epithelial, immune or stromal profiles (rows) compared between normal, MMRp, or MMRd samples (columns). **B,C.** Mouse regions capture malignant features in human tumors. B. Top left: First (PC1, x axis) and second (PC2, y axis) principal components of mouse region scores of mouse and human epithelial pseudo-bulk samples. Top right: PC1 loadings (x axis) of each mouse region score (y axis). Bottom: PC1 values (box plots show mean, quartiles, and whiskers for the full data distribution except for outliers outside 1.5 times the interquartile range (IQR)) for each type of mouse or human sample (x axis). C. Significance (FDR, color bar, two-sided Welch's t-test) of enrichment (red) or depletion (blue) of region-associated profile scores (rows) in normal and dysplastic samples (columns) in human or mouse. **D,E.** Expression of malignant like regions 6 and 11 in tumors are associated with PFI (D) and OS (E) in human patients. Kaplan-Meier PFI (e, n = 662[95]) or OS (f, n = 662[95]) analysis of human bulk RNA-seq cohort stratified by malignant-like region profile scores.

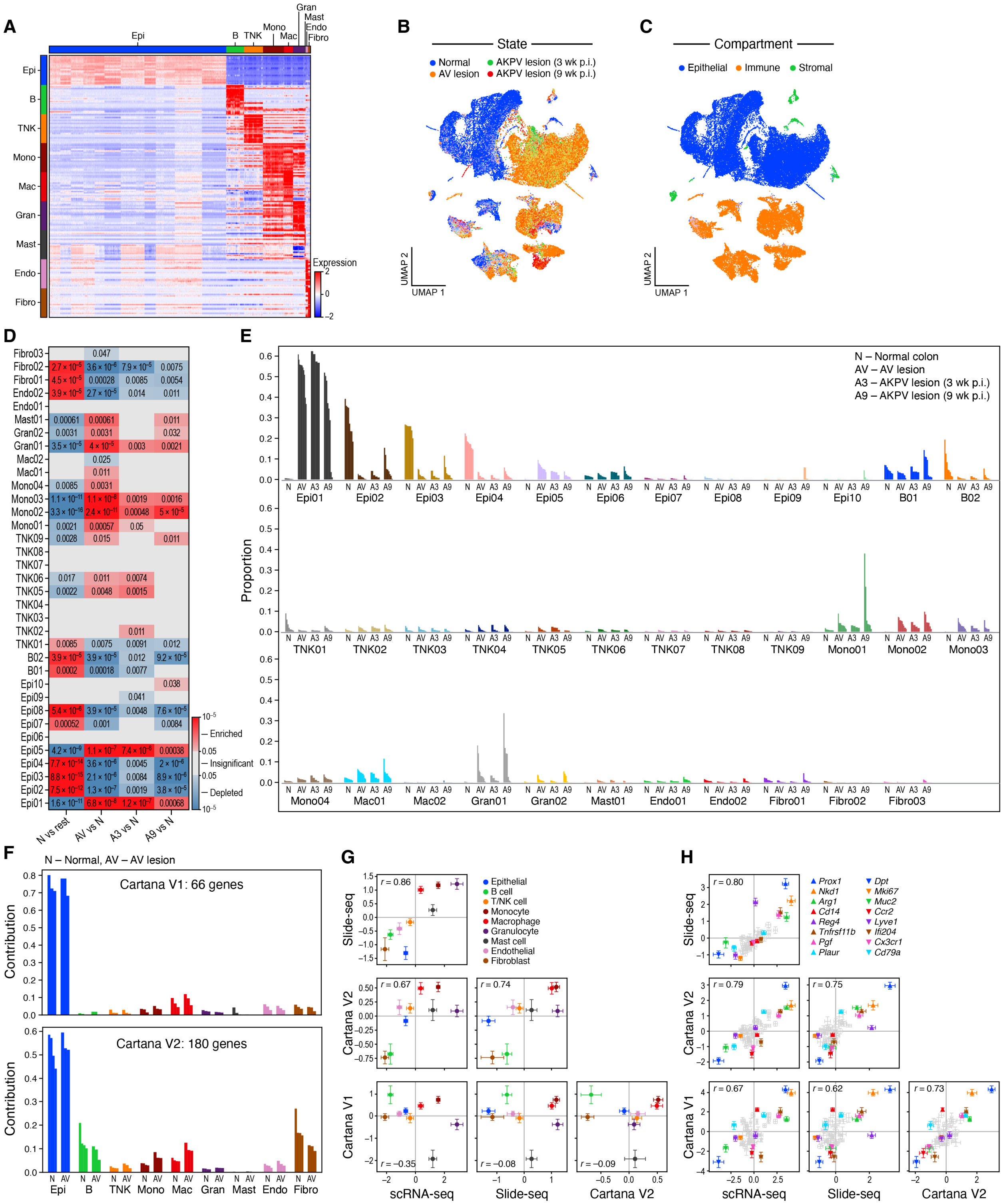
A
Epi
B
TNK
Mono
Mac
Gran
Mast
Endo
Fibro
Expression
2
0
−2
B
State
Normal
AV lesion
AKPV lesion (3 wk p.i.)
AKPV lesion (9 wk p.i.)
UMAP 2
UMAP 1
C
Compartment
Epithelial
Immune
Stromal
UMAP 2
UMAP 1
D
Fibro03: 0.047
Fibro02: 2.7 × 10−5, 3.6 × 10−6, 7.9 × 10−5, 0.0075
Fibro01: 4.5 × 10−5, 0.00028, 0.0085, 0.0054
Endo02: 3.9 × 10−5, 2.7 × 10−5, 0.014, 0.011
Endo01
Mast01: 0.00061, 0.00061, 0.011
Gran02: 0.0031, 0.0031, 0.032
Gran01: 3.5 × 10−5, 4 × 10−5, 0.003, 0.0021
Mac02: 0.025
Mac01: 0.011
Mono04: 0.0085, 0.0031
Mono03: 1.1 × 10−11, 1.1 × 10−8, 0.0019, 0.0016
Mono02: 3.3 × 10−16, 2.4 × 10−11, 0.00048, 5 × 10−5
Mono01: 0.0021, 0.00057, 0.05
TNK09: 0.0028, 0.015, 0.011
TNK08
TNK07
TNK06: 0.017, 0.011, 0.0074
TNK05: 0.0022, 0.0048, 0.0015
TNK04
TNK03
TNK02: 0.011
TNK01: 0.0085, 0.0075, 0.0091, 0.012
B02: 3.9 × 10−5, 3.9 × 10−5, 0.012, 9.2 × 10−5
B01: 0.0002, 0.00018, 0.0077
Epi10: 0.038
Epi09: 0.041
Epi08: 5.4 × 10−6, 3.9 × 10−5, 0.0048, 7.6 × 10−5
Epi07: 0.00052, 0.001, 0.0084
Epi06
Epi05: 4.2 × 10−9, 1.1 × 10−7, 7.4 × 10−6, 0.00038
Epi04: 7.7 × 10−14, 3.6 × 10−6, 0.0045, 2 × 10−6
Epi03: 8.8 × 10−15, 2.1 × 10−6, 0.0084, 8.9 × 10−6
Epi02: 7.5 × 10−12, 1.3 × 10−7, 0.0019, 3.8 × 10−5
Epi01: 1.6 × 10−11, 6.8 × 10−8, 1.2 × 10−7, 0.00068
N vs rest
AV vs N
A3 vs N
A9 vs N
10−5
Enriched
0.05
Insignificant
0.05
Depleted
10−5
E
N – Normal colon
AV – AV lesion
A3 – AKPV lesion (3 wk p.i.)
A9 – AKPV lesion (9 wk p.i.)
Proportion
N AV A3 A9
Epi01 Epi02 Epi03 Epi04 Epi05 Epi06 Epi07 Epi08 Epi09 Epi10 B01 B02
TNK01 TNK02 TNK03 TNK04 TNK05 TNK06 TNK07 TNK08 TNK09 Mono01 Mono02 Mono03
Mono04 Mac01 Mac02 Gran01 Gran02 Mast01 Endo01 Endo02 Fibro01 Fibro02 Fibro03
F
N – Normal, AV – AV lesion
Cartana V1: 66 genes
Cartana V2: 180 genes
Contribution
N AV
Epi B TNK Mono Mac Gran Mast Endo Fibro
G
Epithelial
B cell
T/NK cell
Monocyte
Macrophage
Granulocyte
Mast cell
Endothelial
Fibroblast
Slide-seq
Cartana V2
Cartana V1
scRNA-seq
Slide-seq
Cartana V2
r = 0.86
r = 0.67
r = 0.74
r = −0.35
r = −0.08
r = −0.09
H
Prox1
Nkd1
Arg1
Cd14
Reg4
Tnfrsf11b
Pgf
Plaur
Dpt
Mki67
Muc2
Ccr2
Lyve1
Ifi204
Cx3cr1
Cd79a
Slide-seq
Cartana V2
Cartana V1
scRNA-seq
Slide-seq
Cartana V2
r = 0.80
r = 0.79
r = 0.75
r = 0.67
r = 0.62
r = 0.73

Figure S1. **Marker genes, cell states and cell types in the healthy and dysplastic mouse colon atlas**.

A. Cell-type expression signatures. Scaled log-normalized expression (color bar) of the top 20 differentially expressed genes (rows) in cells (columns) from each cell type. **B,C.** Distinct condition states and compartments. 2D embedding of all single cell profiles (dots) colored by either condition state (B) or compartment (C). **D.** Changes in cell composition in dysplastic lesions. Significance (FDR, color bar, two-sided Welch's t-test on CLR-transformed compositions) of enrichment (red) or depletion (blue) of each cell subset (rows) between samples from different conditions (columns). **E.** Changes in cell composition between healthy and dysplastic tissue. Proportion of cells (y axis) from each cell subset (x axis) out of all cells in each sample (x axis). **F-H.** Multiplex *in situ* RNA profiles (Cartana) reproduce scRNA-seq and Slide-Seq findings. F. Proportion of RNA molecules (y axis) attributed to each cell type in each sample (x axis) in two Cartana experiments, with different gene panels. G. Change in cell proportions in AV vs. normal samples (difference of CLR-transformed cell type fractions, x and y axes) for each cell type (dots, color) based on scRNA-seq, Slide-Seq or Cartana (axis labels). Error bars: bootstrapped standard error of the mean (normal n=8, 16, 12, 16 and AV n=11, 24, 12, 12 for scRNA-seq, Slide-seq, Cartana V1, Cartana V2). H. Change in marker gene expression (dots) in AV vs. normal samples (difference of CLR-transformed gene fractions, x and y axes) based on scRNA-seq, Slide-Seq or Cartana (axis labels), for genes measured by all 3 methods. Genes with the 8 maximal and minimal expression ranks across methods are labeled. Error bars: bootstrapped standard error of the mean (normal n=8, 16, 12, 16 and AV n=11, 24, 12, 12 for scRNA-seq, Slide-seq, Cartana V1, Cartana V2).

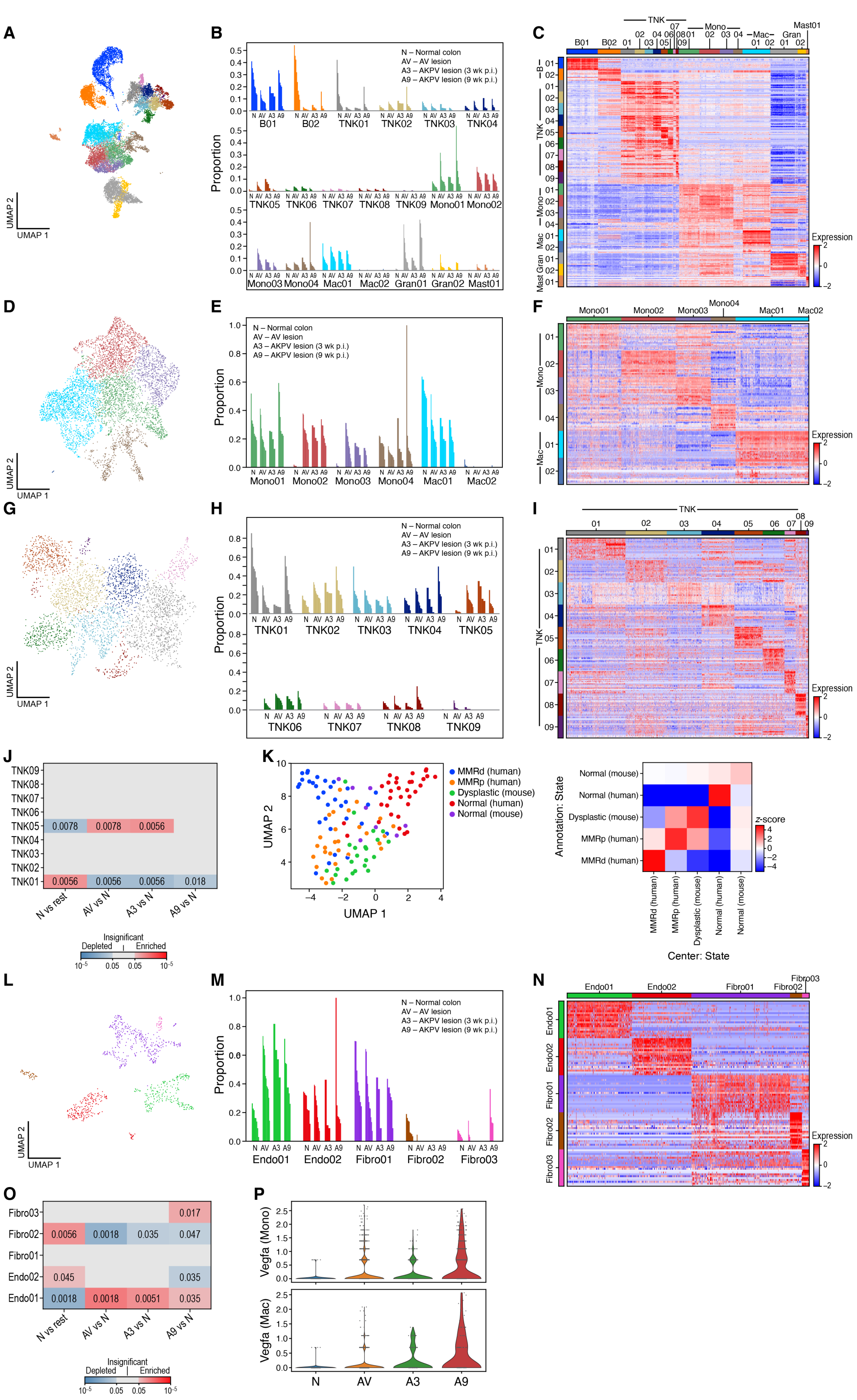
A
UMAP 1
UMAP 2
B
Proportion
N – Normal colon
AV – AV lesion
A3 – AKPV lesion (3 wk p.i.)
A9 – AKPV lesion (9 wk p.i.)
N AV A3 A9
B01 B02 TNK01 TNK02 TNK03 TNK04
TNK05 TNK06 TNK07 TNK08 TNK09 Mono01 Mono02
Mono03 Mono04 Mac01 Mac02 Gran01 Gran02 Mast01
C
B TNK Mono Mac Gran Mast
Expression
D
E
Mono01 Mono02 Mono03 Mono04 Mac01 Mac02
F
G
H
TNK01 TNK02 TNK03 TNK04 TNK05
TNK06 TNK07 TNK08 TNK09
I
J
TNK09 TNK08 TNK07 TNK06 TNK05 TNK04 TNK03 TNK02 TNK01
0.0078 0.0078 0.0056
0.0056 0.0056 0.0056 0.018
N vs rest AV vs N A3 vs N A9 vs N
Insignificant
Depleted Enriched
10^{-5} 0.05 0.05 10^{-5}
K
MMRd (human)
MMRp (human)
Dysplastic (mouse)
Normal (human)
Normal (mouse)
UMAP 1
UMAP 2
Annotation: State
Center: State
z-score
L
M
Endo01 Endo02 Fibro01 Fibro02 Fibro03
N
O
Fibro03 Fibro02 Fibro01 Endo02 Endo01
0.017
0.0056 0.0018 0.035 0.047
0.045 0.035
0.0018 0.0018 0.0051 0.035
P
Vegfa (Mono)
Vegfa (Mac)
N AV A3 A9

Figure S2. Compositional and cell intrinsic changes in stromal and immune cells.

A-C. Immune cell subsets and composition. A. 2D embedding of immune cell profiles colored by clusters (as in B). B. Proportion of cells out of all immune cells (y axis) of each immune cell subset in each sample (x axis). C. Scaled log-normalized expression (color bar) of the top 20 differentially expressed genes (rows) in cells (columns) from each immune cell subset (color bar on top). **D-F**. Monocyte and macrophage cell subsets and composition. D. 2D embedding of monocyte and macrophage cell profiles colored by clusters (as in E). E. Proportion of cells out of all monocytes and macrophages (y axis) of each monocyte and macrophage cell subset in each sample (x axis). F. Scaled log-normalized expression (color bar) of the top 20 differentially expressed genes (rows) in cells (columns) from each monocyte and macrophage cell subset (color bar on top). **G-I.** T/NK cell subsets and composition. G. 2D embedding of T/NK cell profiles colored by clusters (as in H). H. Proportion of cells out of all T/NK cells (y axis) of each T/NK cell subset in each sample (x axis). I. Scaled log-normalized expression (color bar) of the top 20 differentially expressed genes (rows) in cells (columns) from each T/NK cell subset (color bar on top). **J.** Enrichment of IL17+ γδT cells (TNK05) and depletion of CD8+ γδT cells (TNK01) in dysplastic lesions. Significance (FDR, color bar, two-sided Welch's t-test on CLR-transformed compositions) of enrichment (red) or depletion (blue) of each T/NK cell subset (rows) between samples from different conditions (columns). **K**. T/NK cell compositions is similar in human and mouse. Left: 2D embedding of T/NK cell composition profiles of human and mouse samples colored by sample type (legend) (**STAR Methods**). Right: Similarity of T/NK cell composition (enrichment z-scores) in the 2D embedding between each set of samples (rows, columns). **L-N.** Stromal cell subsets and composition. L. 2D embedding of stromal cell profiles colored by clusters (legend). M. Proportion of cells out of all stromal cells (y axis) of each stromal cell subset in each sample (x axis). N.

Scaled log-normalized expression (color bar) of the top 20 differentially expressed genes (rows) in cells (columns) from each stromal cell subset (color bar on top). **O**. Enrichment of vascular endothelial cells (Endo01) and depletion of myofibroblasts (Fibro02) in dysplastic lesions. Significance (FDR, color bar, two-sided Welch's t test on CLR-transformed compositions) of enrichment (red) or depletion (blue) of each stromal cell subset (rows) between samples from different conditions (columns). **P.** Increased VEGFA expression in monocyte-macrophage populations with dysplasia. Distribution of expression (y axis, log1p(counts)) of *VegfA* in monocytes and macrophages from different conditions (x axis).

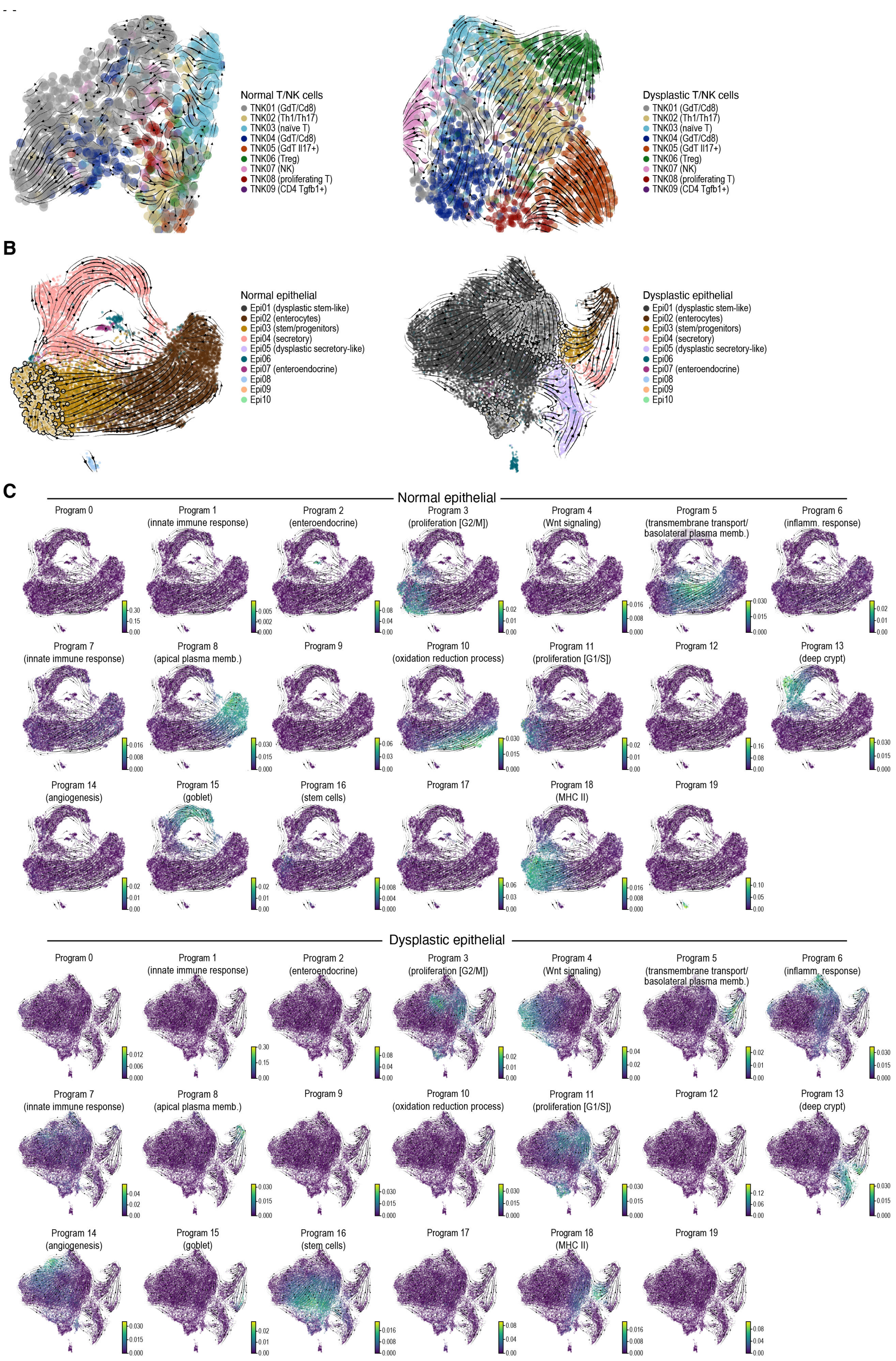
Normal T/NK cells
● TNK01 (GdT/Cd8)
● TNK02 (Th1/Th17)
● TNK03 (naïve T)
● TNK04 (GdT/Cd8)
● TNK05 (GdT Il17+)
● TNK06 (Treg)
● TNK07 (NK)
● TNK08 (proliferating T)
● TNK09 (CD4 Tgfb1+)
Dysplastic T/NK cells
● TNK01 (GdT/Cd8)
● TNK02 (Th1/Th17)
● TNK03 (naïve T)
● TNK04 (GdT/Cd8)
● TNK05 (GdT Il17+)
● TNK06 (Treg)
● TNK07 (NK)
● TNK08 (proliferating T)
● TNK09 (CD4 Tgfb1+)
B
Normal epithelial
● Epi01 (dysplastic stem-like)
● Epi02 (enterocytes)
● Epi03 (stem/progenitors)
● Epi04 (secretory)
● Epi05 (dysplastic secretory-like)
● Epi06
● Epi07 (enteroendocrine)
● Epi08
● Epi09
● Epi10
Dysplastic epithelial
● Epi01 (dysplastic stem-like)
● Epi02 (enterocytes)
● Epi03 (stem/progenitors)
● Epi04 (secretory)
● Epi05 (dysplastic secretory-like)
● Epi06
● Epi07 (enteroendocrine)
● Epi08
● Epi09
● Epi10
C
Normal epithelial
Program 0
0.30 0.15 0.00
Program 1 (innate immune response)
0.005 0.002 0.000
Program 2 (enteroendocrine)
0.08 0.04 0.00
Program 3 (proliferation [G2/M])
0.02 0.01 0.00
Program 4 (Wnt signaling)
0.016 0.008 0.000
Program 5 (transmembrane transport/ basolateral plasma memb.)
0.030 0.015 0.000
Program 6 (inflamm. response)
0.02 0.01 0.00
Program 7 (innate immune response)
0.016 0.008 0.000
Program 8 (apical plasma memb.)
0.030 0.015 0.000
Program 9
0.06 0.03 0.00
Program 10 (oxidation reduction process)
0.030 0.015 0.000
Program 11 (proliferation [G1/S])
0.02 0.01 0.00
Program 12
0.16 0.08 0.00
Program 13 (deep crypt)
0.030 0.015 0.000
Program 14 (angiogenesis)
0.02 0.01 0.00
Program 15 (goblet)
0.02 0.01 0.00
Program 16 (stem cells)
0.008 0.004 0.000
Program 17
0.06 0.03 0.00
Program 18 (MHC II)
0.016 0.008 0.000
Program 19
0.10 0.05 0.00
Dysplastic epithelial
Program 0
0.012 0.006 0.000
Program 1 (innate immune response)
0.30 0.15 0.00
Program 2 (enteroendocrine)
0.08 0.04 0.00
Program 3 (proliferation [G2/M])
0.02 0.01 0.00
Program 4 (Wnt signaling)
0.04 0.02 0.00
Program 5 (transmembrane transport/ basolateral plasma memb.)
0.02 0.01 0.00
Program 6 (inflamm. response)
0.030 0.015 0.000
Program 7 (innate immune response)
0.04 0.02 0.00
Program 8 (apical plasma memb.)
0.030 0.015 0.000
Program 9
0.030 0.015 0.000
Program 10 (oxidation reduction process)
0.030 0.015 0.000
Program 11 (proliferation [G1/S])
0.030 0.015 0.000
Program 12
0.12 0.06 0.00
Program 13 (deep crypt)
0.030 0.015 0.000
Program 14 (angiogenesis)
0.030 0.015 0.000
Program 15 (goblet)
0.02 0.01 0.00
Program 16 (stem cells)
0.016 0.008 0.000
Program 17
0.08 0.04 0.00
Program 18 (MHC II)
0.016 0.008 0.000
Program 19
0.08 0.04 0.00

Figure S3. Changes in T/NK and epithelial cell differentiation in dysplastic lesions.

A. T/NK cell differentiation. 2D embedding of T/NK cell profiles from normal tissues (left) and dysplastic lesions (right), colored by cell subset. Streamlines: averaged and projected RNA velocities. **B,C.** Proliferating stem-like cells give rise to an expanded stem-like compartment and differentiated-like tumor cells in dysplastic lesions. 2D embedding of epithelial cell profiles from normal tissues (B, left and C, top) and dysplastic lesions (B, right, and C, bottom), colored by cell subset (B), or by expression of epithelial programs (C). Streamlines: averaged and projected RNA velocities. Outlined dots (B): Proliferative cells (cells with more than 50% program weight in the proliferation programs #3 and #11).

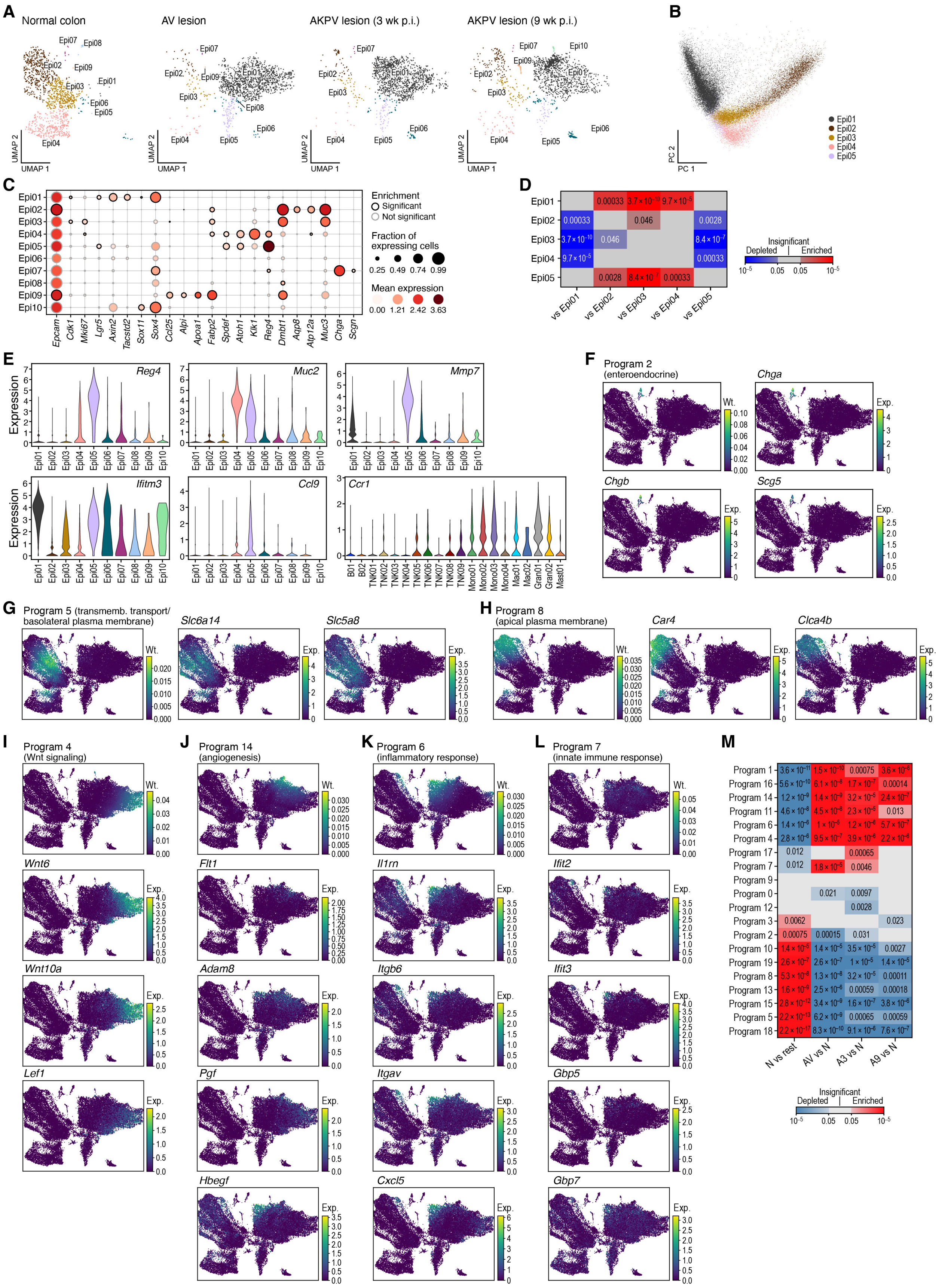
A
Normal colon
AV lesion
AKPV lesion (3 wk p.i.)
AKPV lesion (9 wk p.i.)
Epi01
Epi02
Epi03
Epi04
Epi05
Epi06
Epi07
Epi08
Epi09
Epi10
UMAP 1
UMAP 2
B
PC 1
PC 2
Epi01
Epi02
Epi03
Epi04
Epi05
C
Epcam
Cdk1
Mki67
Lgr5
Axin2
Tacstd2
Sox11
Sox4
Ccl25
Alpi
Apoa1
Fabp2
Spdef
Atoh1
Klk1
Reg4
Dmbt1
Aqp8
Atp12a
Muc3
Chga
Scgn
Enrichment
Significant
Not significant
Fraction of expressing cells
0.25
0.49
0.74
0.99
Mean expression
0.00
1.21
2.42
3.63
D
Epi01: 0.00033, 3.7 × 10⁻¹⁰, 9.7 × 10⁻⁵
Epi02: 0.00033, 0.046, 0.0028
Epi03: 3.7 × 10⁻¹⁰, 0.046, 8.4 × 10⁻⁷
Epi04: 9.7 × 10⁻⁵, 0.00033
Epi05: 0.0028, 8.4 × 10⁻⁷, 0.00033
vs Epi01
vs Epi02
vs Epi03
vs Epi04
vs Epi05
Insignificant
Depleted
Enriched
10⁻⁵
0.05
0.05
10⁻⁵
E
Expression
Reg4
Muc2
Mmp7
Ifitm3
Ccl9
Ccr1
B01
B02
TNK01
TNK02
TNK03
TNK04
TNK05
TNK06
TNK07
TNK08
TNK09
Mono01
Mono02
Mono03
Mono04
Mac01
Mac02
Gran01
Gran02
Mast01
F
Program 2 (enteroendocrine)
Chga
Chgb
Scg5
Wt.
Exp.
G
Program 5 (transmemb. transport/ basolateral plasma membrane)
Slc6a14
Slc5a8
H
Program 8 (apical plasma membrane)
Car4
Clca4b
I
Program 4 (Wnt signaling)
Wnt6
Wnt10a
Lef1
J
Program 14 (angiogenesis)
Flt1
Adam8
Pgf
Hbegf
K
Program 6 (inflammatory response)
Il1rn
Itgb6
Itgav
Cxcl5
L
Program 7 (innate immune response)
Ifit2
Ifit3
Gbp5
Gbp7
M
Program 1: 3.6 × 10⁻¹¹, 1.5 × 10⁻¹⁰, 0.00075, 3.6 × 10⁻⁶
Program 16: 5.6 × 10⁻¹⁰, 6.1 × 10⁻⁸, 1.7 × 10⁻⁷, 0.00014
Program 14: 1.2 × 10⁻⁹, 1.4 × 10⁻⁹, 3.2 × 10⁻⁵, 2.4 × 10⁻⁷
Program 11: 4.6 × 10⁻⁸, 4.5 × 10⁻⁸, 2.3 × 10⁻⁵, 0.013
Program 6: 1.4 × 10⁻⁶, 1 × 10⁻⁵, 1.2 × 10⁻⁶, 5.7 × 10⁻⁷
Program 4: 2.8 × 10⁻⁶, 9.5 × 10⁻⁷, 3.9 × 10⁻⁶, 2.2 × 10⁻⁶
Program 17: 0.012, 0.00065
Program 7: 0.012, 1.8 × 10⁻⁵, 0.0046
Program 9
Program 0: 0.021, 0.0097
Program 12: 0.0028
Program 3: 0.0062, 0.023
Program 2: 0.00075, 0.00015, 0.031
Program 10: 1.4 × 10⁻⁵, 1.4 × 10⁻⁵, 3.5 × 10⁻⁵, 0.0027
Program 19: 2.6 × 10⁻⁷, 2.6 × 10⁻⁷, 1 × 10⁻⁵, 1.4 × 10⁻⁵
Program 8: 5.3 × 10⁻⁸, 1.3 × 10⁻⁸, 3.2 × 10⁻⁵, 0.00011
Program 13: 1.6 × 10⁻⁹, 2.5 × 10⁻⁶, 0.00059, 0.00018
Program 15: 2.8 × 10⁻¹², 3.4 × 10⁻⁹, 1.6 × 10⁻⁷, 3.8 × 10⁻⁶
Program 5: 2.2 × 10⁻¹³, 6.2 × 10⁻⁹, 0.00065, 0.00059
Program 18: 2.2 × 10⁻¹⁷, 8.3 × 10⁻¹⁰, 9.1 × 10⁻⁶, 7.6 × 10⁻⁷
N vs rest
AV vs N
A3 vs N
A9 vs N
Insignificant
Depleted
Enriched
10⁻⁵
0.05
0.05
10⁻⁵

Figure S4. Changes in cell composition and expression programs usage in dysplastic epithelium.

A-D. Changes in epithelial cell composition in dysplastic tissues. A. 2D embedding of all single cell epithelial profiles showing only the profiles (dots) of cells from each condition state, subsampled to equal numbers of cells per condition state, colored by cluster. B. PCA captures differentiation status and lineage of epithelial clusters. First (PC1, x axis) and second (PC2, y axis) principal components of the expression of epithelial clusters. C. Mean expression (dot color) and fraction of expressing cells (dot size) of epithelial cell marker genes[97] (columns) in each cluster (rows). D. Significance (FDR, color bar, two-sided Welch's t test on ALR-transformed compositions with all non-tdTomato counts used as reference compartment) of enrichment (red) or depletion (blue) of tdTomato expression in cells from AKPVT samples between every pair of epithelial clusters. **E.** Dysplastic secretory like (Epi05) and immune cells express tumor-related genes. Distribution of expression (y axis, log1p(counts)) of different marker genes in cells from each epithelial/immune cell cluster (x axis). **F-L**. Epithelial gene programs. 2D embedding of all epithelial cells colored by the weight of each program (color bar) and the expression of selected program genes (color bar). **M.** Epithelial program characteristics of normal and dysplastic colon. Heatmap significance (FDR, color bar, two-sided Welch's t test on CLR-transformed compositions) of enrichment (red) or depletion (blue) of each epithelial program (rows) between normal vs. dysplastic tissues (columns).

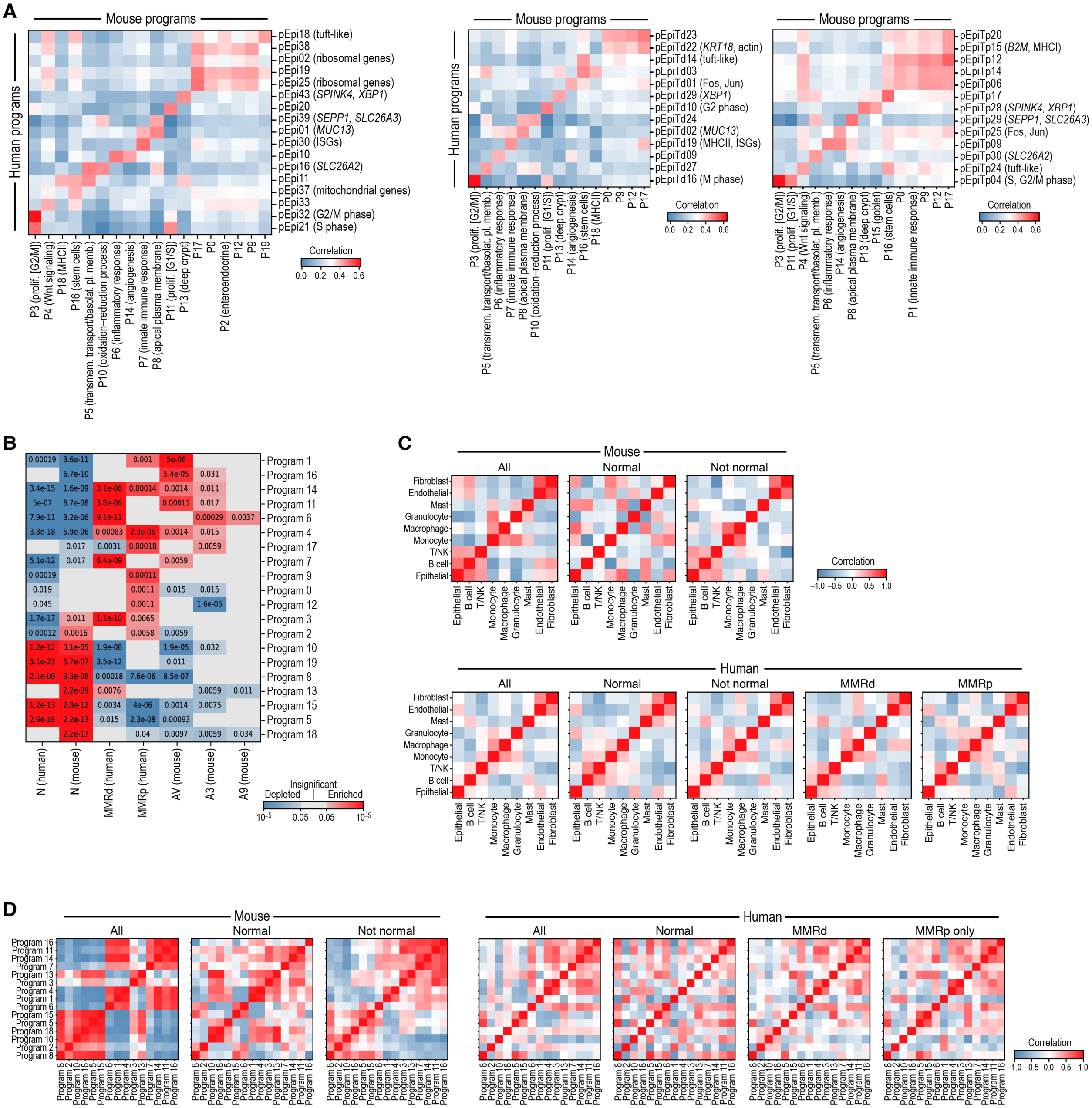

	N (human)	N (mouse)	MMRd (human)	MMRp (human)	AV (mouse)	A3 (mouse)	A9 (mouse)
Program 1	0.00019	3.6e-11		0.001	5e-06		
Program 16		6.7e-10			5.4e-05	0.031	
Program 14	3.4e-15	1.6e-09	3.1e-06	0.00014	0.0014	0.011	
Program 11	5e-07	8.7e-08	3.8e-06		0.00011	0.017	
Program 6	7.9e-11	3.2e-06	9.1e-11			0.00029	0.0037
Program 4	3.8e-18	5.9e-06	0.00083	2.3e-06	0.0014	0.015	
Program 17		0.017	0.0031	0.00018		0.0059	
Program 7	5.1e-12	0.017	6.4e-09		0.0059		
Program 9	0.00019			0.00011			
Program 0	0.019			0.0011	0.015	0.015	
Program 12	0.045			0.0011		1.6e-05	
Program 3	1.7e-17	0.011	1.1e-10	0.0065			
Program 2	0.00012	0.0016		0.0058	0.0059		
Program 10	1.2e-12	3.1e-05	1.9e-08		1.9e-05	0.032	
Program 19	5.1e-23	5.7e-07	3.5e-12		0.011		
Program 8	2.1e-09	9.3e-08	0.00018	7.6e-06	8.5e-07		
Program 13		2.2e-09	0.0076			0.0059	0.011
Program 15	1.2e-13	2.8e-12	0.0034	4e-06	0.0014	0.0075	
Program 5	2.9e-16	2.2e-13	0.015	2.3e-08	0.00093		
Program 18		2.2e-17		0.04	0.0097	0.0059	0.034

Figure S5. Conservation of cellular composition and expression programs between mouse and human scRNA-seq data.

A,B. Conservation of general and subtype-specific human and mouse epithelial expression programs. A. Pearson correlation coefficients (color) between program-specific expression profiles (**Methods**) of human (all samples, left, MMRd, middle and MMRp, right)) (rows) and mouse programs (columns). B. Mouse epithelial program enrichments in mouse and human tumor and normal samples. Significance (FDR, color bar, two-sided Welch t-test on CLR-transformed compositions) of enrichment (red) or depletion (blue) of mouse epithelial program expression (rows) in sample classes from human or mouse (columns). **C,D.** Human-mouse conservation of cell type and program associations. Pearson correlation coefficients (color) of the CLR-transformed cell type (C) or epithelial program (D) compositions across samples in mouse (left) or human (right) single cell data. In (D), data are hierarchically clustered for the “not normal” mouse case (AV and AKPV) and this ordering is applied to all other panels.

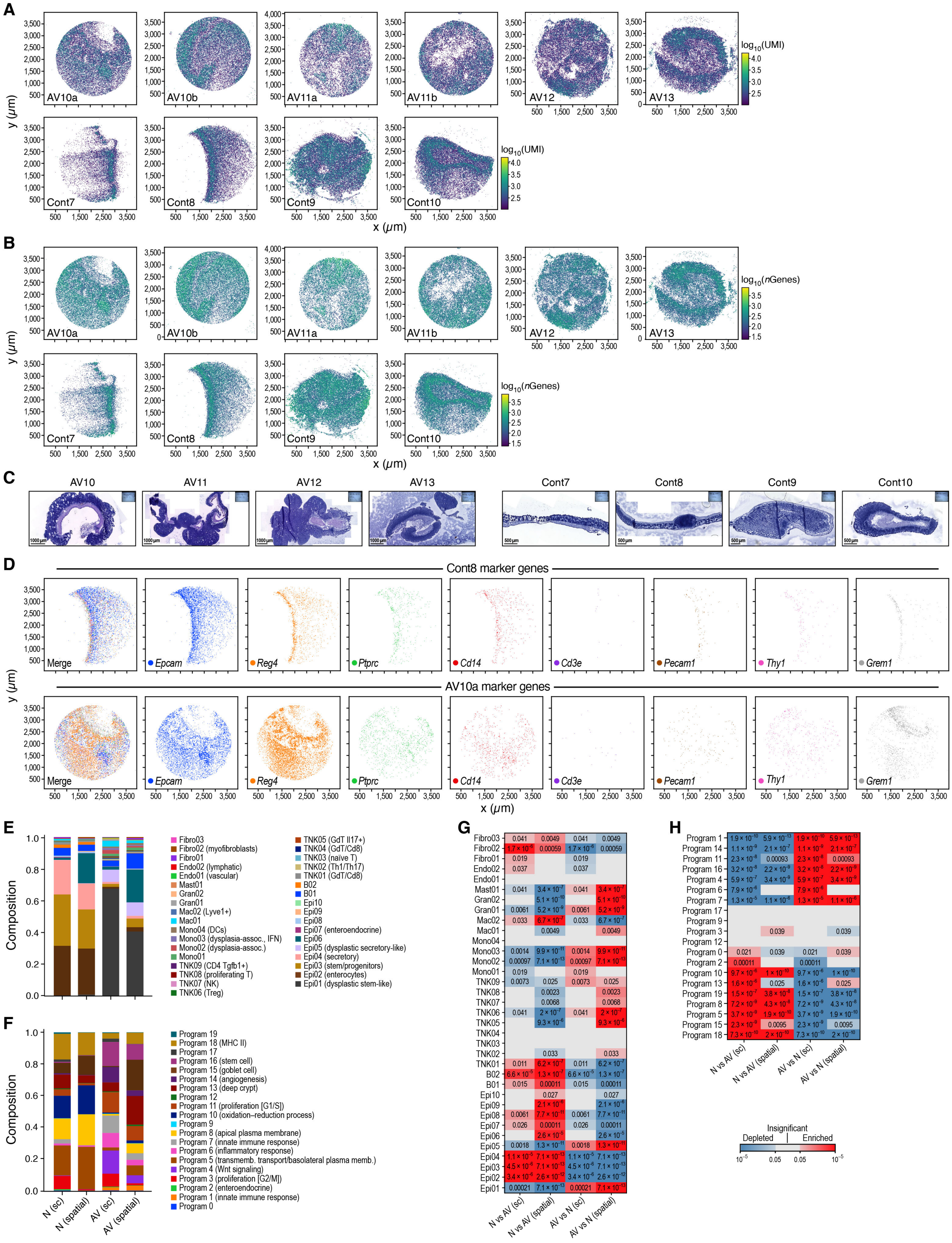
A
AV10a
AV10b
AV11a
AV11b
AV12
AV13
Cont7
Cont8
Cont9
Cont10
log10(UMI)
y (μm)
x (μm)
B
log10(nGenes)
C
AV10
AV11
AV12
AV13
Cont7
Cont8
Cont9
Cont10
D
Cont8 marker genes
AV10a marker genes
Merge
Epcam
Reg4
Ptprc
Cd14
Cd3e
Pecam1
Thy1
Grem1
E
Composition
Fibro03
Fibro02 (myofibroblasts)
Fibro01
Endo02 (lymphatic)
Endo01 (vascular)
Mast01
Gran02
Gran01
Mac02 (Lyve1+)
Mac01
Mono04 (DCs)
Mono03 (dysplasia-assoc., IFN)
Mono02 (dysplasia-assoc.)
Mono01
TNK09 (CD4 Tgfb1+)
TNK08 (proliferating T)
TNK07 (NK)
TNK06 (Treg)
TNK05 (GdT Il17+)
TNK04 (GdT/Cd8)
TNK03 (naive T)
TNK02 (Th1/Th17)
TNK01 (GdT/Cd8)
B02
B01
Epi10
Epi09
Epi08
Epi07 (enteroendocrine)
Epi06
Epi05 (dysplastic secretory-like)
Epi04 (secretory)
Epi03 (stem/progenitors)
Epi02 (enterocytes)
Epi01 (dysplastic stem-like)
F
Program 19
Program 18 (MHC II)
Program 17
Program 16 (stem cell)
Program 15 (goblet cell)
Program 14 (angiogenesis)
Program 13 (deep crypt)
Program 12
Program 11 (proliferation [G1/S])
Program 10 (oxidation–reduction process)
Program 9
Program 8 (apical plasma membrane)
Program 7 (innate immune response)
Program 6 (inflammatory response)
Program 5 (transmemb. transport/basolateral plasma memb.)
Program 4 (Wnt signaling)
Program 3 (proliferation [G2/M])
Program 2 (enteroendocrine)
Program 1 (innate immune response)
Program 0
N (sc)
N (spatial)
AV (sc)
AV (spatial)
G
H
N vs AV (sc)
N vs AV (spatial)
AV vs N (sc)
AV vs N (spatial)
Insignificant
Depleted
Enriched
10⁻⁵
0.05
0.05
10⁻⁵

Figure S6. **Spatial distributions of cells and programs across regions.**

A-C. Slide-seq quality controls. Slide-seq pucks of AV (top) and normal (bottom) mouse colon colored by number of UMIs (A) or of genes (B) per bead. (x and y axis: spatial coordinates (μm)). C. H&E staining of sections adjacent to those used for Slide-seq. **D.** Selected marker gene expression. Slide-seq pucks from a normal (top) and AV (bottom) sample, colored by marker gene detected per bead. **E,F.** Spatial mapping of cell types and programs yields comparable composition to scRNA-seq. Distribution of the proportion (y axis) of contributions to each cell type (D) or program (E; based on fractional annotations) in cells (for scRNA-seq; “sc”) or beads (for Slide-seq; “spatial”; based on fractional annotations) in samples from normal (N) or AV (AV) tissue. **G,H.** Distinct cell types and programs associated with AV and normal colon. Significance (FDR, color bar, two-sided Welch’s t test on CLR-transformed compositions) of enrichment (red) or depletion (blue) of cell types (F, rows) or epithelial programs (G, rows) in normal (N) or AV (AV) tissues based on Slide-seq (“spatial”) data or scRNA-seq ("sc”).

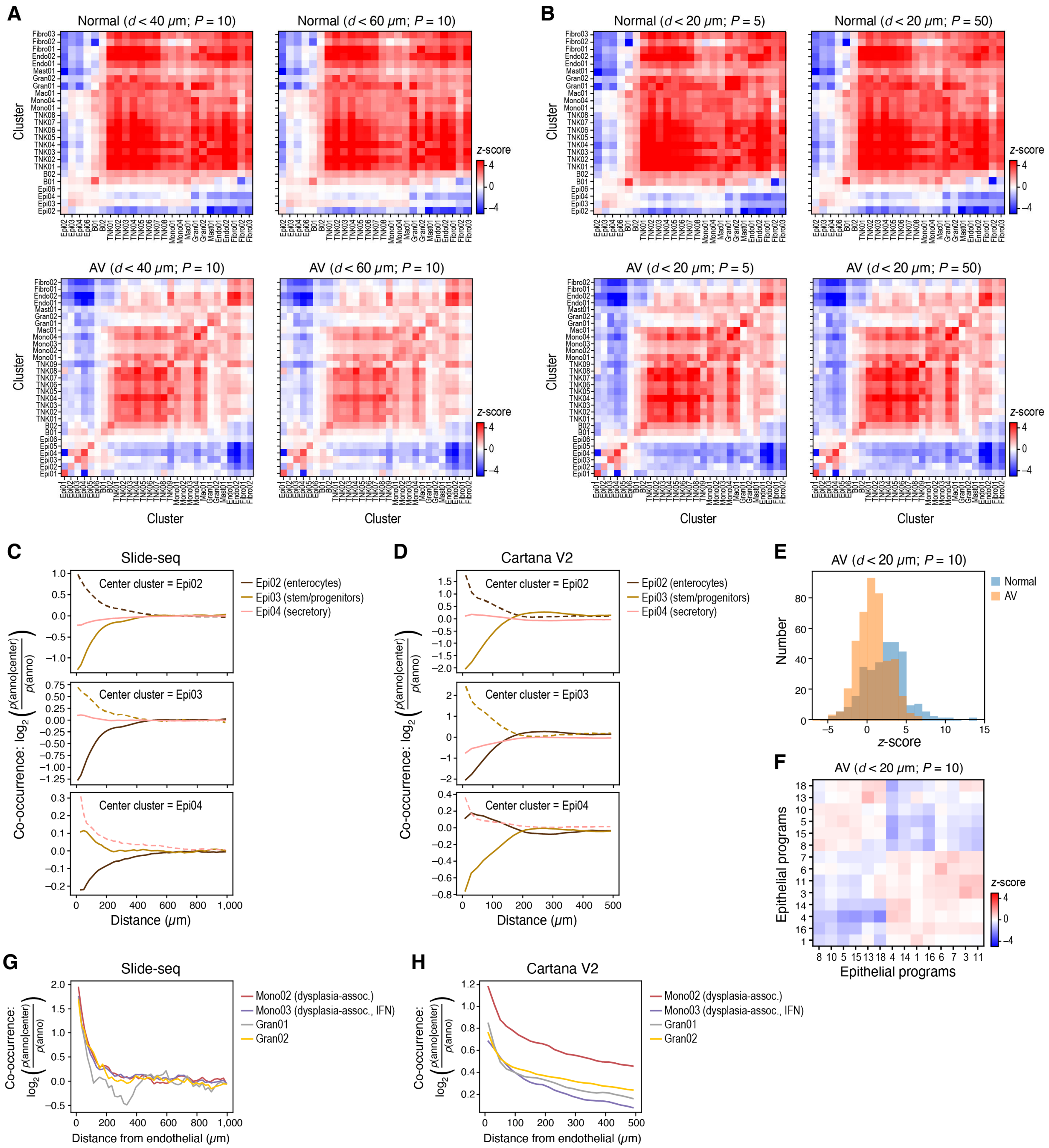
A
Normal ($d < 40$ μm; $P = 10$)
Normal ($d < 60$ μm; $P = 10$)
B
Normal ($d < 20$ μm; $P = 5$)
Normal ($d < 20$ μm; $P = 50$)
AV ($d < 40$ μm; $P = 10$)
AV ($d < 60$ μm; $P = 10$)
AV ($d < 20$ μm; $P = 5$)
AV ($d < 20$ μm; $P = 50$)
Cluster
z-score
4
0
−4
Fibro03
Fibro02
Fibro01
Endo02
Endo01
Mast01
Gran02
Gran01
Mac01
Mono04
Mono03
Mono02
Mono01
TNK09
TNK08
TNK07
TNK06
TNK05
TNK04
TNK03
TNK02
TNK01
B02
B01
Epi06
Epi05
Epi04
Epi03
Epi02
Epi01
C
Slide-seq
D
Cartana V2
Center cluster = Epi02
Center cluster = Epi03
Center cluster = Epi04
Epi02 (enterocytes)
Epi03 (stem/progenitors)
Epi04 (secretory)
Co-occurrence: $\log_2\left(\frac{p(\text{anno}|\text{center})}{p(\text{anno})}\right)$
Distance (μm)
0
200
400
600
800
1,000
100
300
500
E
AV ($d < 20$ μm; $P = 10$)
Normal
AV
Number
z-score
−5
0
5
10
15
F
AV ($d < 20$ μm; $P = 10$)
Epithelial programs
18
13
10
5
15
8
7
6
11
3
14
4
16
1
z-score
G
Slide-seq
H
Cartana V2
Mono02 (dysplasia-assoc.)
Mono03 (dysplasia-assoc., IFN)
Gran01
Gran02
Co-occurrence: $\log_2\left(\frac{p(\text{anno}|\text{center})}{p(\text{anno})}\right)$
Distance from endothelial (μm)

Figure S7. Distinct cellular layout in normal and AV tissues.

A,B. Neighborship analysis is robust to the distance and number of randomizations. Neighborship enrichment (z-scores, color) *vs*. a background of spatially random annotation assignments for each pair of cell annotations (rows, columns) in normal (top) and AV (bottom) samples at varying distance (a, left: ≤40µm; right: ≤60 µm) or number of permutations (B, left: 5, right: 50). **C,D.** Reproducible spatial arrangement of epithelial cells in normal colon in Slide-seq and Cartana V2. Co-occurrence (y axis) of normal epithelial cell types (color) at different distances (x axis) from different central normal epithelial cell type (annotated on top) in Slide-Seq (C) and Cartana (D) data. **E.** Decreased spatial order of cell types in AV vs. normal tissue. Distribution of enrichment z-values (x axis) of cluster-cluster interactions (as shown in **Figure 3B,C**) in AV lesions (orange) and normal colon (blue). **F.** Epithelial program neighborships in AV tissue. Short-range (≤20µm) neighborship enrichment z-scores (color) *vs*. a background of spatially random annotation assignments for each pair of epithelial program annotations (rows, columns) in AV lesions. **G,H.** Reproducible spatial arrangement of dysplasia-associated immune cells relative to endothelial cells in Slide-seq and Cartana V2. Co-occurrence (y axis) of dysplasia-associated monocyte or granulocyte cells (color) with endothelial cells at different distances (x axis) in Slide-Seq (G) and Cartana (H) data.

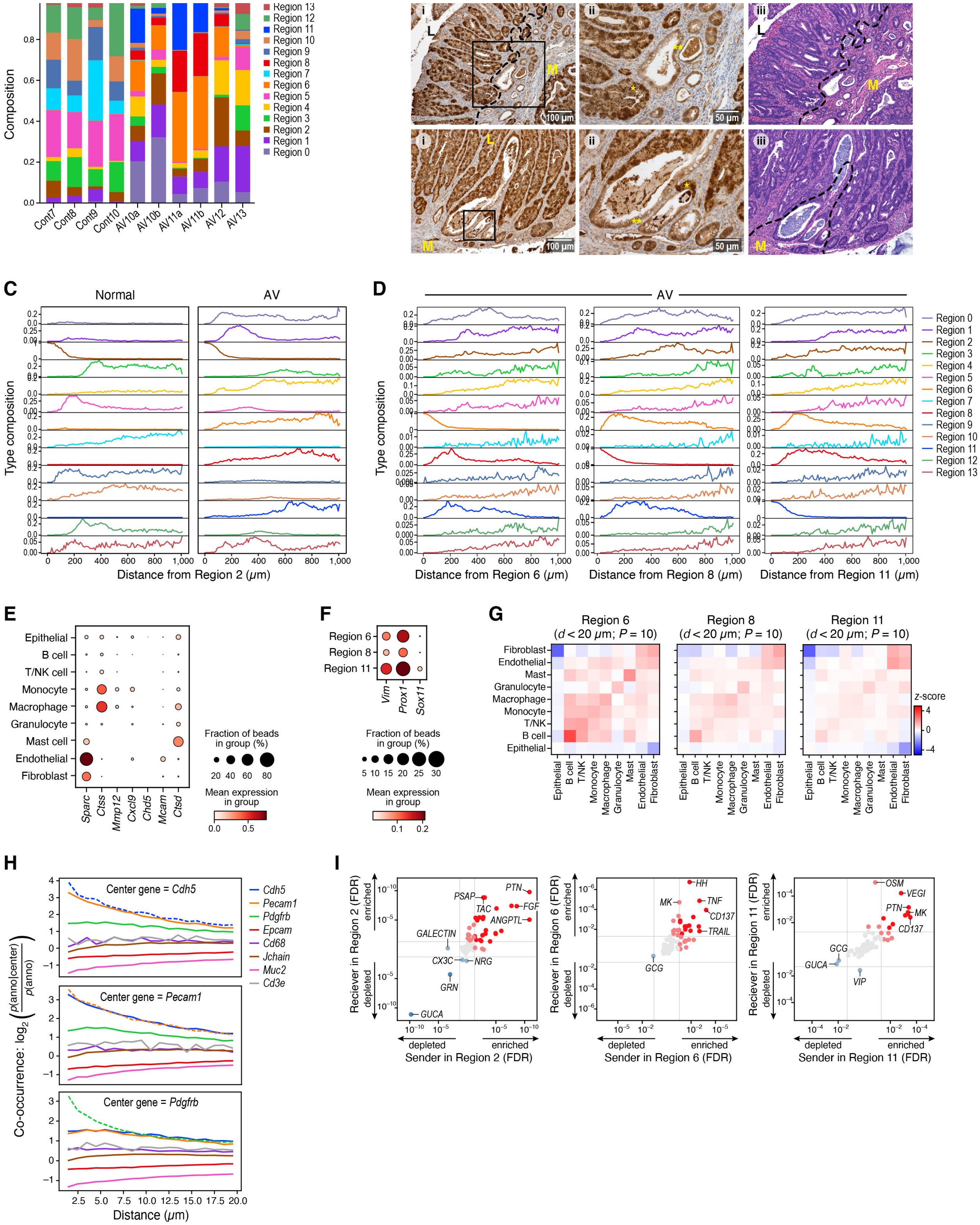
Composition
Cont7
Cont8
Cont9
Cont10
AV10a
AV10b
AV11a
AV11b
AV12
AV13
Region 13
Region 12
Region 11
Region 10
Region 9
Region 8
Region 7
Region 6
Region 5
Region 4
Region 3
Region 2
Region 1
Region 0
i
ii
iii
L
M
100 μm
50 μm
C
Normal
AV
Type composition
Distance from Region 2 (μm)
D
AV
Distance from Region 6 (μm)
Distance from Region 8 (μm)
Distance from Region 11 (μm)
E
Epithelial
B cell
T/NK cell
Monocyte
Macrophage
Granulocyte
Mast cell
Endothelial
Fibroblast
Sparc
Ctss
Mmp12
Cxcl9
Chd5
Mcam
Ctsd
Fraction of beads in group (%)
Mean expression in group
F
Region 6
Region 8
Region 11
Vim
Prox1
Sox11
G
Region 6 (d < 20 μm; P = 10)
Region 8 (d < 20 μm; P = 10)
Region 11 (d < 20 μm; P = 10)
Fibroblast
Endothelial
Mast
Granulocyte
Macrophage
Monocyte
T/NK
B cell
Epithelial
z-score
H
Center gene = Cdh5
Center gene = Pecam1
Center gene = Pdgfrb
Cdh5
Pecam1
Pdgfrb
Epcam
Cd68
Jchain
Muc2
Cd3e
Co-occurrence: log2(p(anno|center)/p(anno))
Distance (μm)
I
Reciever in Region 2 (FDR)
Reciever in Region 6 (FDR)
Reciever in Region 11 (FDR)
enriched
depleted
Sender in Region 2 (FDR)
Sender in Region 6 (FDR)
Sender in Region 11 (FDR)
PTN
FGF
PSAP
TAC
ANGPTL
GALECTIN
CX3C
NRG
GRN
GUCA
HH
MK
TNF
CD137
TRAIL
GCG
OSM
VEGI
VIP

Figure S8. Cellular neighborhoods.

A. Distinct characteristic region distributions in healthy and AV tissue. Proportion of UMIs assigned to each region (y axis) in each Slide-seq puck (x axis). **B.** β-catenin expression in AV lesions. Representative images (i) of β-catenin IHC on sections of AV lesions showing either nuclear (*) or cytoplasmic (**) staining pattern (x10 magnification), along with high magnification (x20, ii) of the region highlighted in (i), and H&E staining (iii) of a serial section showing a region proximal to the region in (i). (M-muscularis, L-lumen, dashed line: border between areas of nuclear and cytoplasmic staining of β-catenin). **C,D.** Spatial relations between the regions. Proportion of beads (y axis) of each region category (color code) at different distances (x axis) from region 2 (C, muscularis), 6 (D, left), 8 (D, middle) or 11 (D, right). **E,F.** Fraction of expressing cells (dot size) and mean expression per celltype (E, dot color) or per region (F, dot color) of marker genes (columns) across cell types in region 6 (E, rows) or regions 6, 8 and 11 (F, rows). **G.** Cell type neighborships in different malignant regions. Short-range (≤20μm) neighborship enrichment z-scores (color) *vs*. a background of spatially random annotation assignment for each pair of cell type annotations (rows, columns) in malignant-like regions 6, 8 and 11 within AV lesions. **H.** Spatial organization of endothelial cells and pericytes based on Cartana multiplex *in situ* RNA analysis. Co-occurrence (y axis) of Cdh5 (top) or Pecam1 (middle) -expressing (endothelial) cells or Pdgfrb (bottom) -expressing cells (pericytes) at different distances (x axis) from each central cell type (color code), based on expression of a specific gene (color bar). **I.** Cell-cell interaction pathways enriched in different regions. Enrichment (FDR) in regions 2 (muscularis, left), 6 (malignant-like, inflammation, middle) or 11 (malignant-like, EMT, right) of corresponding “sender” (x axis) and “receiver” (y axis) (aggregated over ligand-receptor pairs) pathways (dots). Red/blue: pathways significantly enriched/depleted in region (light red/blue: only enriched/depleted for either sender or receiver). The top 5 enriched pathways (in each direction) are labeled.

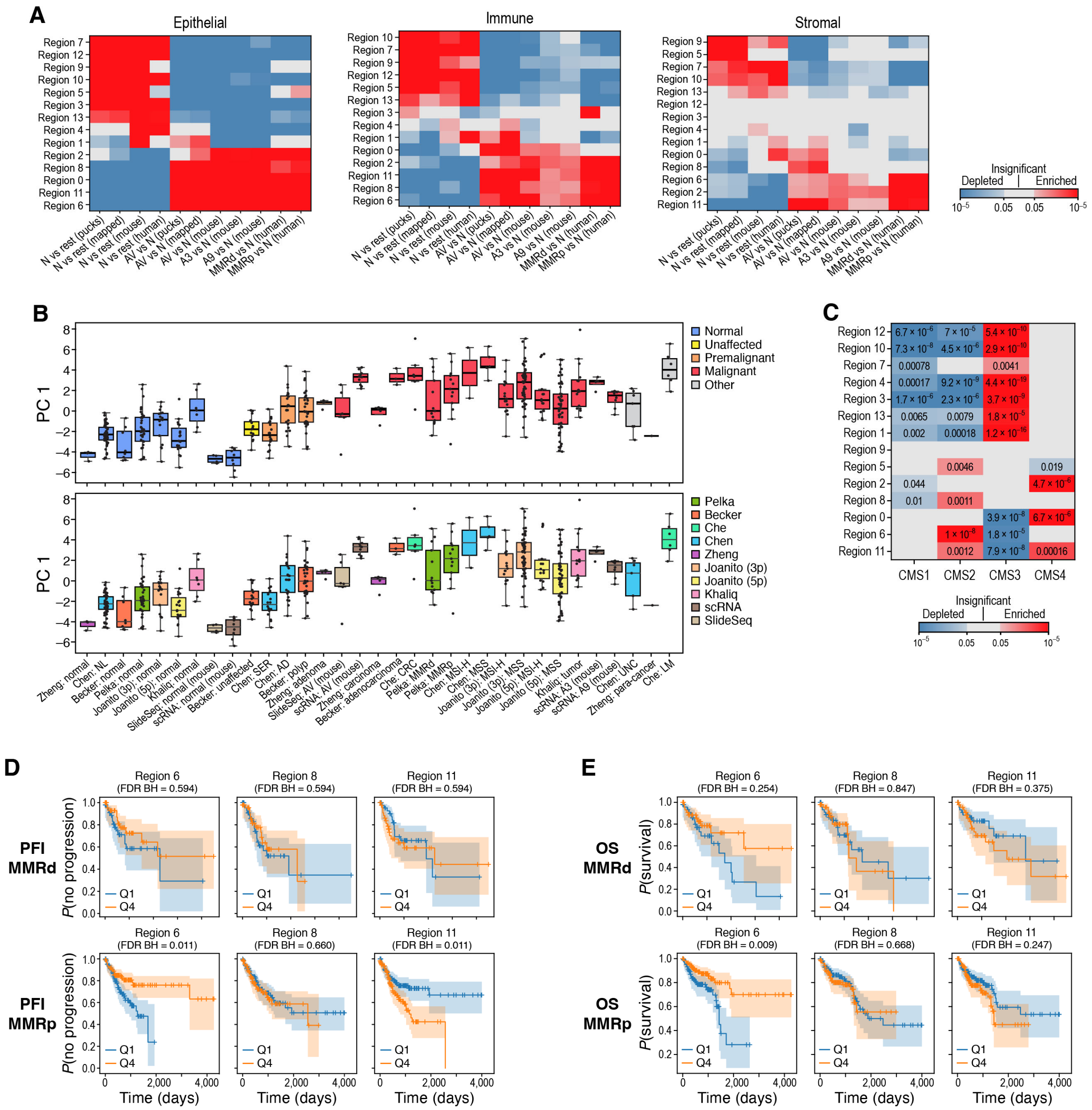

	CMS1	CMS2	CMS3	CMS4
Region 12	6.7×10^{-6}	7×10^{-5}	5.4×10^{-10}	
Region 10	7.3×10^{-8}	4.5×10^{-6}	2.9×10^{-10}	
Region 7	0.00078		0.0041	
Region 4	0.00017	9.2×10^{-9}	4.4×10^{-19}	
Region 3	1.7×10^{-6}	2.3×10^{-6}	3.7×10^{-9}	
Region 13	0.0065	0.0079	1.8×10^{-5}	
Region 1	0.002	0.00018	1.2×10^{-16}	
Region 9				
Region 5		0.0046		0.019
Region 2	0.044			4.7×10^{-6}
Region 8	0.01	0.0011		
Region 0			3.9×10^{-8}	6.7×10^{-6}
Region 6		1×10^{-8}	1.8×10^{-5}	
Region 11		0.0012	7.9×10^{-8}	0.00016

Figure S9. Transfer of mouse spatial region expression profiles to human patient data.

A. Expression profiles characterizing mouse regions in human and mouse samples. Significance (FDR, color bar, two-sided Welch's t test on CLR-transformed compositions) of enrichment (red) or depletion (blue) of mouse region-associated epithelial (left), immune (middle) or stromal profiles (right) in pucks from normal colon and dysplastic lesions, in the same pucks but after mapping the region annotation to itself (consistency check), in mouse single cell data after mapping region annotation from mouse pucks, and in human single cell data after mapping region annotation from mouse pucks. **B**. PC1 values (y axis; box plots show mean, quartiles, and whiskers for the full data distribution except for outliers outside 1.5 times the interquartile range (IQR)) in a PCA of region scores of mouse and human samples (x axis) sorted by malignant status and colored by status (top, legend) or study (bottom, legend). **C**. Spatial regions profiles associated with different CMS classes. Significance (Benjamini-Hochberg FDR, color bar, two-sided Welch's t test) of enrichment (red) or depletion (blue) of each region profile (rows) in pseudo bulk profiles of human tumor samples classified in each CMS class (columns). **D,E**. Expression of malignant-like regions 6 and 11 in tumors is associated with PFI and OS in MMRd and MMRp patients. Kaplan-Meier PFI (f, MMRd n = 189[95], MMRp n = 447[95]) or OS (g, MMRd n = 189[95], MMRp n = 447[95]) analysis of human bulk RNA-seq cohort stratified by malignant-like region profile scores.

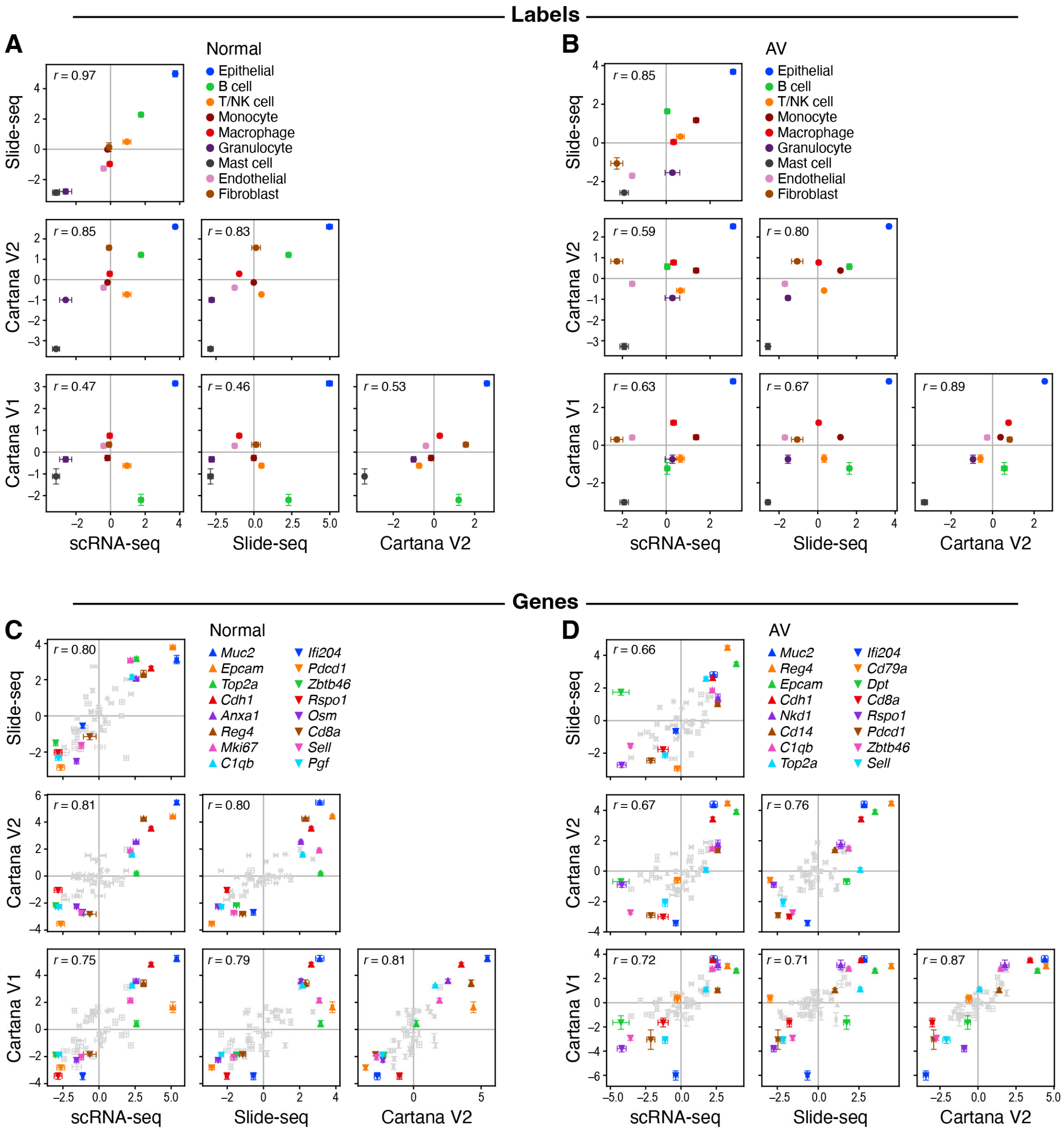
Labels
A
Normal
Epithelial
B cell
T/NK cell
Monocyte
Macrophage
Granulocyte
Mast cell
Endothelial
Fibroblast
r = 0.97
r = 0.85
r = 0.83
r = 0.47
r = 0.46
r = 0.53
B
AV
Epithelial
B cell
T/NK cell
Monocyte
Macrophage
Granulocyte
Mast cell
Endothelial
Fibroblast
r = 0.85
r = 0.59
r = 0.80
r = 0.63
r = 0.67
r = 0.89
Slide-seq
Cartana V2
Cartana V1
scRNA-seq
Slide-seq
Cartana V2
Genes
C
Normal
Muc2
Epcam
Top2a
Cdh1
Anxa1
Reg4
Mki67
C1qb
Ifi204
Pdcd1
Zbtb46
Rspo1
Osm
Cd8a
Sell
Pgf
r = 0.80
r = 0.81
r = 0.80
r = 0.75
r = 0.79
r = 0.81
D
AV
Muc2
Reg4
Epcam
Cdh1
Nkd1
Cd14
C1qb
Top2a
Ifi204
Cd79a
Dpt
Cd8a
Rspo1
Pdcd1
Zbtb46
Sell
r = 0.66
r = 0.67
r = 0.76
r = 0.72
r = 0.71
r = 0.87
Slide-seq
Cartana V2
Cartana V1
scRNA-seq
Slide-seq
Cartana V2

Supplementary item 1. Correspondence between scRNA-seq, Slide-seq, and Cartana data

A,B. Agreement in cell type proportions. Inferred cell type proportions (y and x axis; CLR-transformed cell type fractions) for each cell type (dot color) in normal (A) and AV (B) samples in scRNA-seq, Slide-Seq and Cartana data (axis labels). Pearson's r: top left corners. Error bars: bootstrapped standard error of the mean ((A) n=8, 16, 12, 16 and (B) n=11, 24, 12, 12 for scRNA-seq, Slide-seq, Cartana V1, Cartana V2). **C,D**. Agreement in gene expression levels. Measured expression (y and x axis; CLR-transformed gene fractions) for each gene (dot) measured by all three methods in normal (A) and AV (B) samples in scRNA-seq, Slide-Seq and Cartana data (axis labels). Pearson's r: top left corners. Error bars: bootstrapped standard error of the mean ((C) n=8, 16, 12, 16 and (D) n=11, 24, 12, 12 for scRNA-seq, Slide-seq, Cartana V1, Cartana V2). Genes with the 8 maximal and minimal expression ranks across methods are labeled.

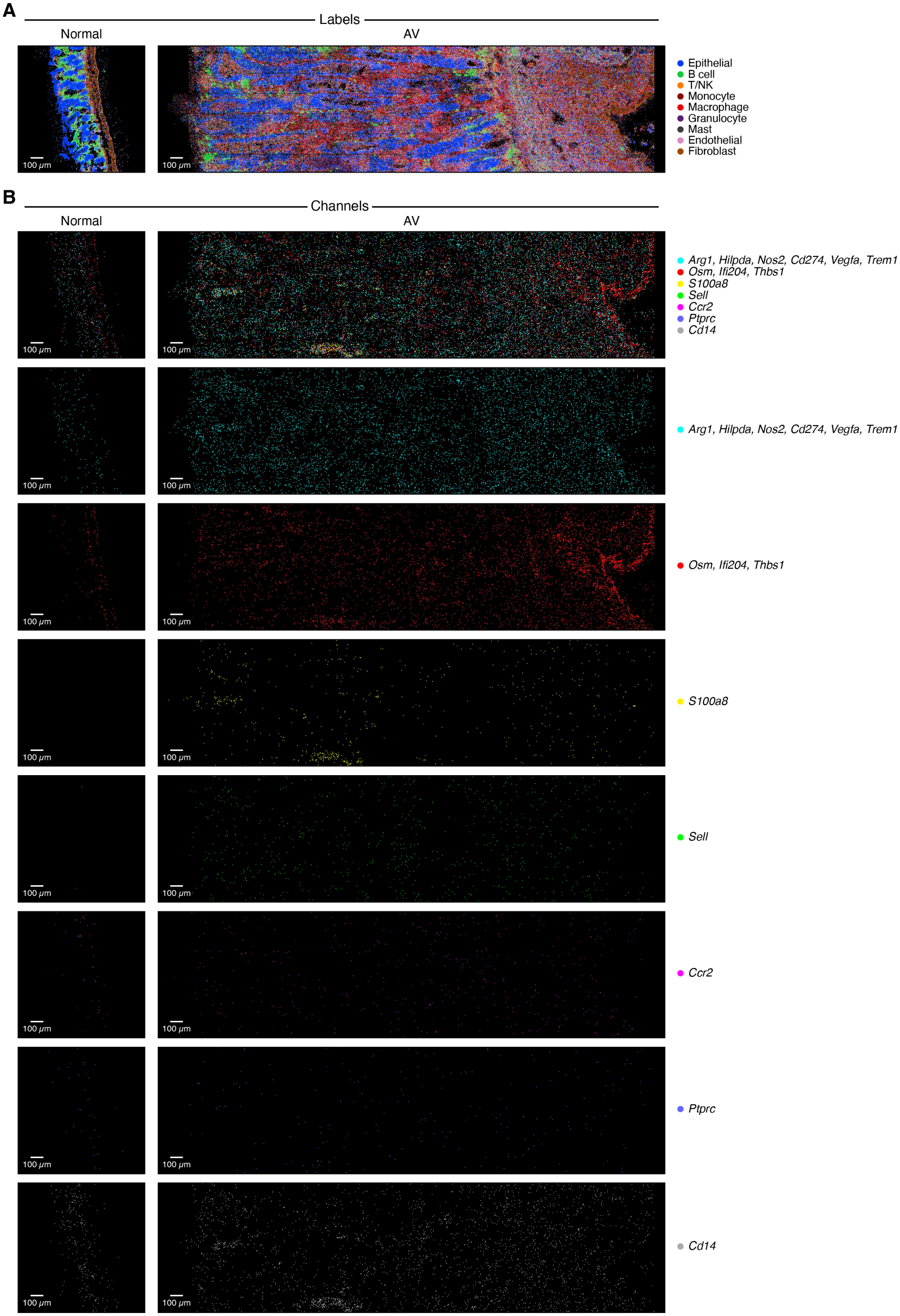
A
Labels
Normal
AV
100 μm
100 μm
● Epithelial
● B cell
● T/NK
● Monocyte
● Macrophage
● Granulocyte
● Mast
● Endothelial
● Fibroblast
B
Channels
Normal
AV
100 μm
● *Arg1, Hilpda, Nos2, Cd274, Vegfa, Trem1*
● *Osm, Ifi204, Thbs1*
● *S100a8*
● *Sell*
● *Ccr2*
● *Ptprc*
● *Cd14*

1831

Supplementary item 2. Dysplasia-associated cells in the tumor microenvironment.

A,B. Representative images of multiplex RNA analysis in normal colon (left) and AV lesions (right) colored by cell type assignment (A, the same is **Figure 1E**) and expression of marker genes (B) for Mono02 (Arg1, Hilpda, Nos2, Cd274, Vegfa, Trem1; cyan), Mono03 (Osm, Ifi204 and Thbs1; red), granulocytes (S100a8; yellow), as well as Sell (green), Ccr2 (magenta), Ptprc (blue) and Cd14 (gray).

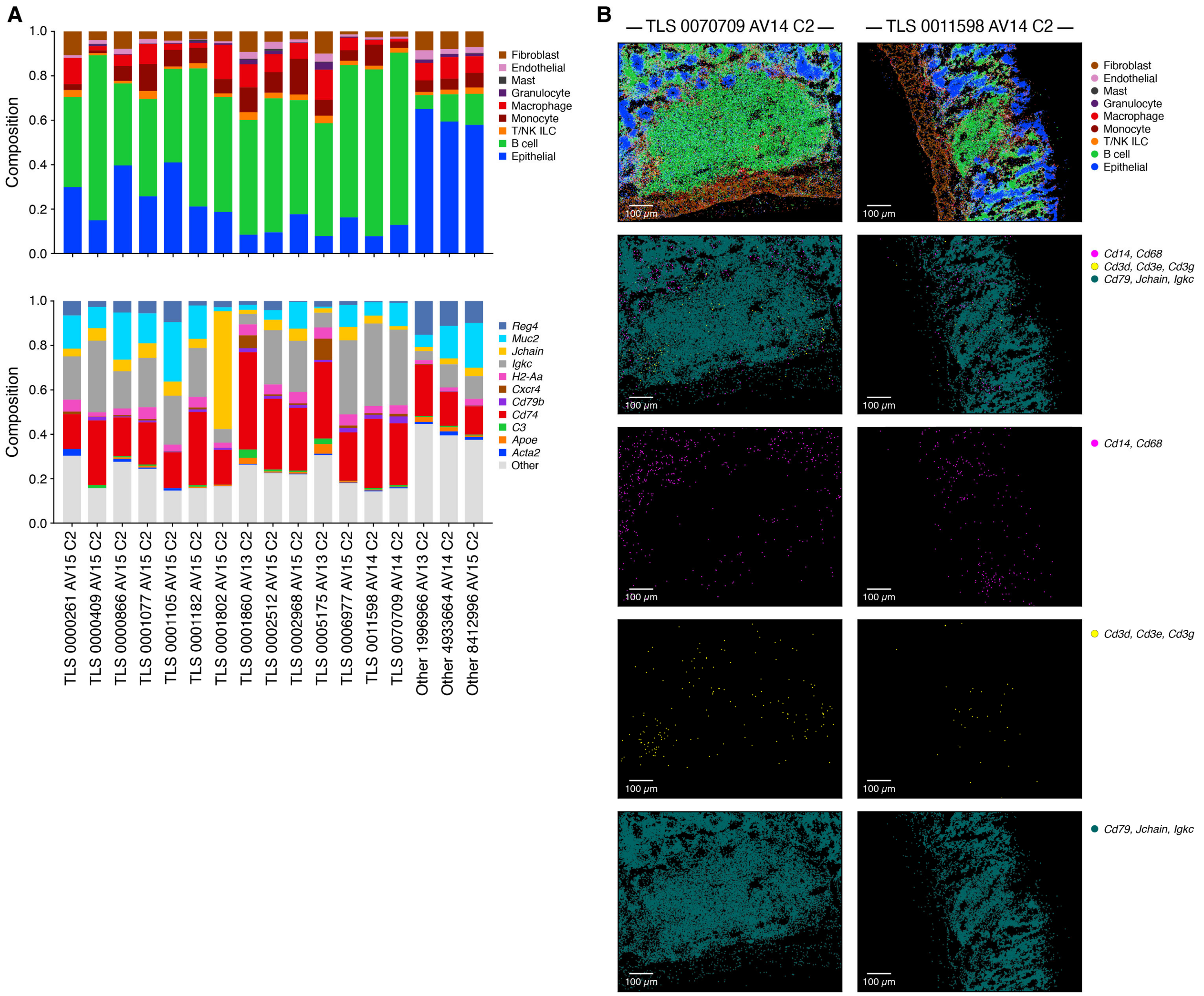
A
Composition
1.0
0.8
0.6
0.4
0.2
0.0
Fibroblast
Endothelial
Mast
Granulocyte
Macrophage
Monocyte
T/NK ILC
B cell
Epithelial
Reg4
Muc2
Jchain
Igkc
H2-Aa
Cxcr4
Cd79b
Cd74
C3
Apoe
Acta2
Other
TLS 0000261 AV15 C2
TLS 0000409 AV15 C2
TLS 0000866 AV15 C2
TLS 0001077 AV15 C2
TLS 0001105 AV15 C2
TLS 0001182 AV15 C2
TLS 0001802 AV15 C2
TLS 0001860 AV13 C2
TLS 0002512 AV15 C2
TLS 0002968 AV15 C2
TLS 0005175 AV13 C2
TLS 0006977 AV15 C2
TLS 0011598 AV14 C2
TLS 0070709 AV14 C2
Other 1996966 AV13 C2
Other 4933664 AV14 C2
Other 8412996 AV15 C2
B
— TLS 0070709 AV14 C2 —
— TLS 0011598 AV14 C2 —
100 μm
Cd14, Cd68
Cd3d, Cd3e, Cd3g
Cd79, Jchain, Igkc

Supplementary item 3. TLS-like structures in AV **lesions by Cartana multiplex *in situ* RNA profiles.**

A. Proportion of RNA molecules (y axis) attributed to each cell type (top) or gene (bottom) in TLS-like regions (x axis) in Cartana V2 multiplex *in situ* RNA experiment. Genes which constitute at least 3% of all measured transcripts in any of the identified follicular structures are noted (bottom). **B.** Representative images from TLS-like regions showing the distribution of cell type (top row) and of cell type markers (bottom four rows; Cd14, Cd68 (monocytes, magenta), Cd3d, Cd3e, Cd3g (T cells, yellow), and Cd79, Jchain, Igkc (B cells, dark cyan)).

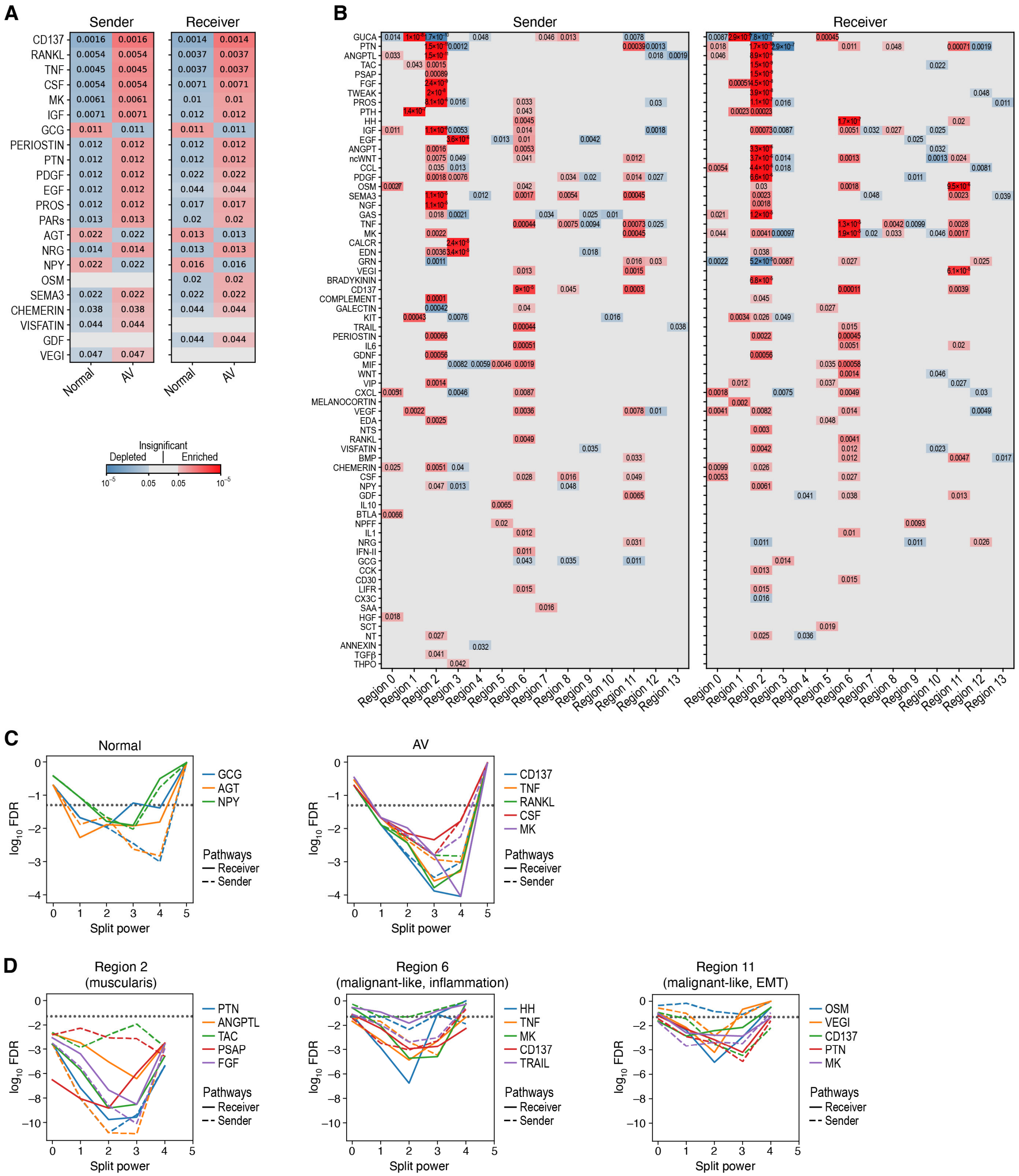
A
Sender
Receiver
CD137
RANKL
TNF
CSF
MK
IGF
GCG
PERIOSTIN
PTN
PDGF
EGF
PROS
PARs
AGT
NRG
NPY
OSM
SEMA3
CHEMERIN
VISFATIN
GDF
VEGI
Normal
AV
Insignificant
Depleted
Enriched
10^{-5}
0.05
0.05
10^{-5}
B
Sender
Receiver
Region 0
Region 1
Region 2
Region 3
Region 4
Region 5
Region 6
Region 7
Region 8
Region 9
Region 10
Region 11
Region 12
Region 13
C
Normal
AV
$\log_{10}$ FDR
Split power
GCG
AGT
NPY
CD137
TNF
RANKL
CSF
MK
Pathways
Receiver
Sender
D
Region 2 (muscularis)
Region 6 (malignant-like, inflammation)
Region 11 (malignant-like, EMT)
PTN
ANGPTL
TAC
PSAP
FGF
HH
TNF
MK
CD137
TRAIL
OSM
VEGI
CD137
PTN
MK
Pathways
Receiver
Sender
$\log_{10}$ FDR
Split power

Supplementary item 4. Ligand-receptor analysis.

A,B. Cell-cell interaction pathways enriched in normal and AV tissue and regions. Significance (FDR, color bar, two-sided Mann-Whitney U test) of enrichment (red) or depletion (blue) of expression of “sender” (left) and “receiver” (right) cell-cell communication pathways (rows) (aggregted from ligand-receptor pairs) in normal *vs*. AV samples (A, columns), or regions (B, columns). **C,D.** Split power analysis for cell-cell communication pathway analysis. Significance of enrichment ($\log_{10}$(FDR), y-axis) for receiver (solid lines) and sender (dashed line) for each of the top 5 enriched communication pathways (color) in each iteration for the spatial split of the Slide-Seq pucks into spatially disconnected and separated patches (x axis), for either normal vs. AV tissue enrichment (C) or for specific regions (D).